Alshook NA et al. JOTCSA. 2025; 12(1): 1-14

RESEARCH ARTICLE

Development of a Silica-Organic Framework Ionic Solid Bronsted Acid Catalyst for the Synthesis of 2,4,5-trisubstituted Imidazole Derivatives

Noor Abbas Alshook[1] ID, Haitham Dalol Hanoon[1*] ID, Hayder Hamied Mihsen[1] ID

[1]University of Karbala, Collage of Science, Department of Chemistry, Karbala, Iraq.

Abstract: Heterogeneous Bronsted acid is one of the most promising compounds that can be used as a catalyst in chemical production, and that can certainly have a positive impact on the environment. This research includes the preparation of heterogeneous Bronsted acid by using rice hulls as a starting material. The prepared acid was characterized by FTIR, XRD, TGA, SEM-EDX, TEM, and elemental analysis. The FTIR results showed the presence of N-H and S=O absorption bands within the expected range in prepared Bronsted acid. The specific surface area of the catalyst determined by Brunauer-Emmett-Teller (BET) using the nitrogen adsorption method is 205.42 m^2/g, and the average pore diameters are 3.69 nm, 2,4,5-Trisubstituted imidazole derivatives were prepared by reacting substituted aldehydes with benzil and ammonium acetate in the presence of a solid acid catalyst. The main advantages of this method are safe, cheap, and short reaction conditions. In addition, the prepared catalyst can be reused.

1. INTRODUCTION

Agricultural and industrial waste negatively impacts the environment by causing air pollution and contaminating water and soil. However, these issues can be mitigated by utilizing this waste, providing a potential source of income and a means to reduce waste production and its environmental effects (1). One of the essential agricultural wastes is rice husks, which are used in the composition of many medical and agricultural industries. They are the hard covering surrounding the grain of rice to protect it from insects and pathogens during growth. It is separated when the rice is harvested (2,3). Rice represents a significant food source for more than half of the Earth's population, with its annual volume reaching more than 100 million tons. Rice husks are rich in silica, or silicon dioxide, and represent about 20% of their weight. It is one of the common forms of silica found in nature, as it is rarely seen in its pure form (4,5). Notably, rice hulls have been talked about as a source of silica before. Last year, researchers at "Chaudhary Sharan" University in India published a similar study that concluded that rice husks represent a good source for obtaining silica with the appropriate structure at a low cost (6).

Silica is obtained from the rice hulls as sodium silicate. So, acid treatment converts the silica into a gel. This method of extraction is possible at ambient temperatures and is an alternative to temperature treatment (7-9).

Sulfated silicate catalysts are comprised of two components: one is composed of sulfuric acid adsorbed to silica, and the other is composed of sulfated silica. The utilization of Sulfuric acid adsorbed on silica is simple and cost-effective for large-scale synthesis because the acid can be repeated without altering the catalytic system's activity. Studies have demonstrated that it is a safe, environmentally friendly, and reusable catalyst (10, 11). The adsorbed form of sulfuric acid on silica is considered an exceptional candidate for use as a chemical solvent or component of a chemical solution; the approach circumvents these limitations. Other chemicals, including silica acid, have been employed to catalyze chemical reactions to increase yields and other properties. Other common chemicals used to accomplish this include sulfuric acid and tribufos. Many research groups have employed this catalyst, which is composed of sulfonic

acid, as a powerful chemical reagent, such as silica sulfuric acid and solid sulfanilic acid (11, 12).

Solid acid catalysts synthesize many organic compounds, including heterocyclic compounds. Heterocycles are the largest and most diverse family of organic compounds. Among numerous nitrogen-containing heterocyclic compounds, imidazole is a key heterocyclic molecule in many biologically active compounds and synthetic drugs (13, 14).

We focus on developing an environmentally friendly method to synthesize substituted imidazole derivatives under mild conditions without producing hazardous by-products. The purpose of this study is to synthesize 2,4,5-trisubstituted imidazole derivatives in the presence of recyclable solid acid catalyst $SiO_2PrOPDA-SO_4H$.

2. EXPERIMENTAL SECTION

2.1. General Information
The rice husks were taken from Abbasiya town in Najaf City. All chemicals and solvents are purchased from BDH Sigma/Aldrich and Scharlau. The FTIR characterization was obtained by spectrophotometer 8400s Shimadzu, ranging from 4000 to 400 cm^{-1}. powder X-ray diffractometer was recorded by Philips PW 1730/10, which is equipped with a Cu-K$_\alpha$ source of radiation. Elemental analysis (CHNS) was performed by an Eager 300 computer on the EA1112. Scanning electron microscopy (SEM) was obtained by FESEM MIRA III (TESCAN)/(Czech Republic). Atomic force microscopy (AFM) was obtained by NT-MDT/INTEGRA (Nederland), and Thermogravimetric analysis was carried out on TA Instruments SDT- Q600, Belgium, from 30 to 900 °C at a heating rate of 20 °C per minute under nitrogen flow. ^1H NMR spectra were recorded on a Bruker 400 MHz German NMR spectrometer using DMSO-d$_6$ as the solvent, and TMS was employed as the internal standard. Mass spectra were obtained using an Agilent 5375 mass spectrometer.

2.2. Synthesis of the Catalyst
2.2.1. The preparation process of rice husks
The rice husk (RH) was washed two times in distilled water and left at room temperature for two days. 30 g of cleaned rice husk was added to the 500 mL of 1 M nitric acid and stirred at room temperature for 24 h. After that, the RH was washed with distilled water until it reached pH 6-7 and dried in an oven at 110 °C overnight. Rice husks, after this process, are labeled as RH-NO$_3$.

2.2.2. Preparation of sodium silicate solution from rice husks
The preparation process of the sodium silicate from RH-NO$_3$ was performed using a recently reported

method (14, 15). 30 g of RH-NO$_3$ was mixed with 200 mL of 1 M sodium hydroxide in a plastic container and stirred for 24 h. The mixture was filtered to remove the residual cellulose. The filtration represented sodium silicate and was used as a precursor to the synthesis catalyst, as shown in Scheme 1.

*2.2.3. Preparation of rice husk silica-3-(Chloropropyl)triethoxysilane (RH-SiO$_2$PrCl)*
About 6 mL of 3-(chloropropyl)triethoxysilane (CPTES) was added to 50 mL of prepared sodium silicate solution. The mixture was titrated with 3 M HNO$_3$ until the pH reached 3. The formed gel was separated by centrifuge at 4000 r/min for 5 min. The mixture was washed with distilled water five times and finally washed with acetone, then dried at 110 °C for 24 h. The weight of the product was 6.4 g, and the prepared sample was labeled as RH-SiO$_2$PrCl, as shown in Scheme 1.

2.2.4. Preparation of acid catalyst (RH-SiO$_2$PrOPDA-SO$_4$H)
A 1 g of RH-SiO$_2$PrCl was added to the mixture of 2 g, 18.5 mmol o-phenylenediamine, and 2.6 mL, 18.8 mmol triethylamine in 30 mL of toluene. The mixture was refluxed at 110 °C for 24 h. The resulting solution contained a yellow solid precipitate, and it was filtered and washed with DMSO, ethanol, and acetone. Then dry at 110 °C for 24 h. Finally, 0.7 g of powder, which was RH-SiO$_2$PrOPDA, was collected. 40 mL of 0.5 M sulfuric acid was then stirred with (0.7 g) of the product at room temperature for 24 h., and the precipitate was washed with a large amount of distilled water and dried in an oven at 110 °C for 24 h. Finally, brown powder (1.20 g) was obtained, and the product was labeled as RH-SiO$_2$PrOPDA-SO$_4$H. As shown in Scheme 1.

2.3. Synthesis of 2,4,5-trisubstituted Imidazole Derivatives (4a-e)
A mixture of (1 mmol) benzil, (1 mmol) aldehyde, (5 mmol) ammonium acetate, and (0.04 g) RH-SiO$_2$PrOPDA-SO$_4$H was dissolved in (5 mL) ethanol. The mixture was heated to reflux and stirred for 4 h. After the reaction was completed, the crude product was poured into dichloromethane (10 mL), stirred for 15 min, then the solid Bronsted acid catalyst was removed by filtration. The catalyst was recovered in three consecutive cycles under the same conditions (Figure 13). Pour the filtrate into 10 mL of cold water and stir for 10 min. The precipitate was filtered, washed with water, and then dried under a vacuum. The product was purified by recrystallization in an ethanol-water mixture to give the 2,4,5-trisubstituted imidazole derivative, as shown in Scheme 2. All products were confirmed through melting point, FT-IR, ^1H NMR, and mass spectrometry analyses.
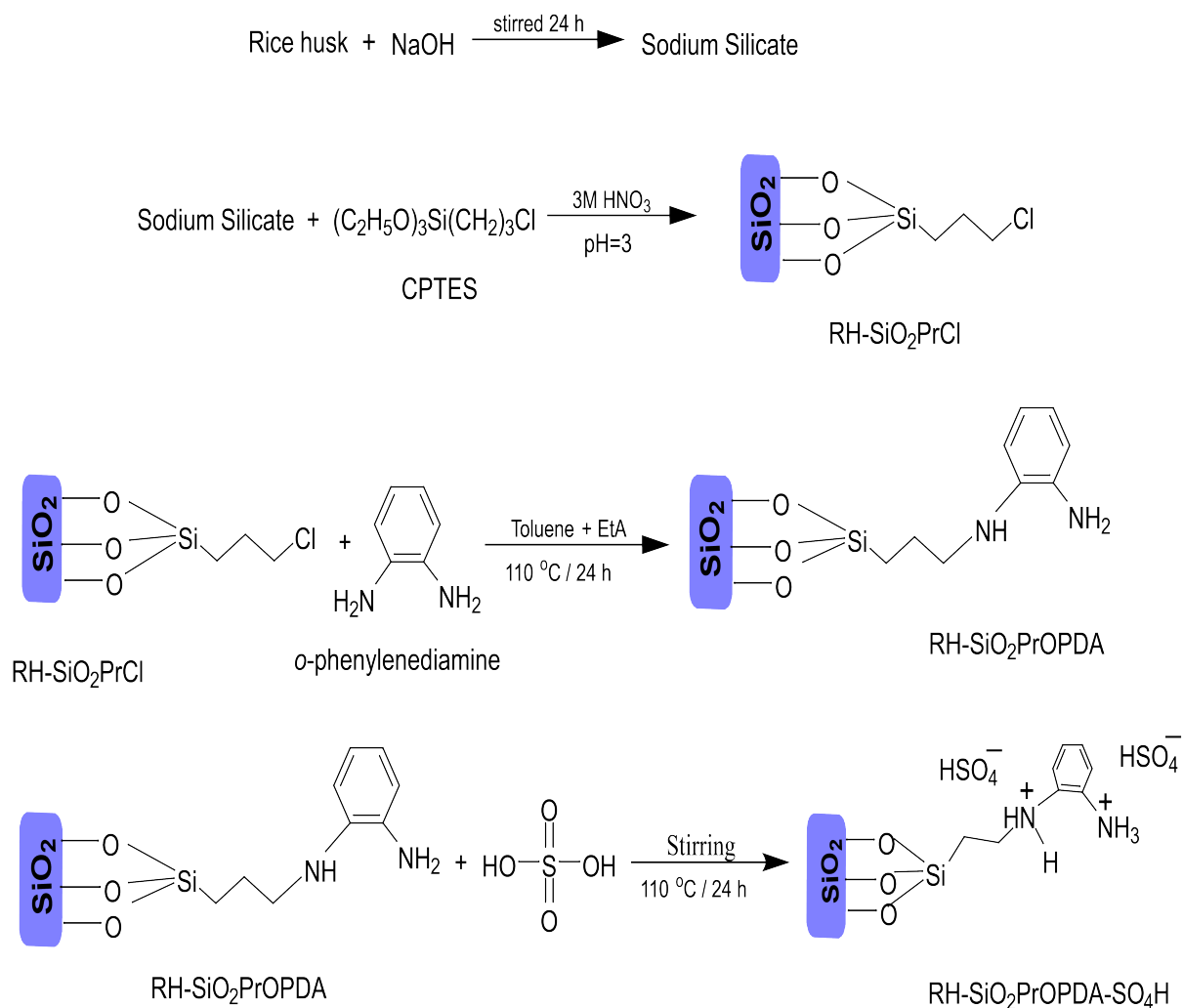
Scheme 1: Preparation process of RH-SiO$_2$PrOPDA-SO$_4$H.
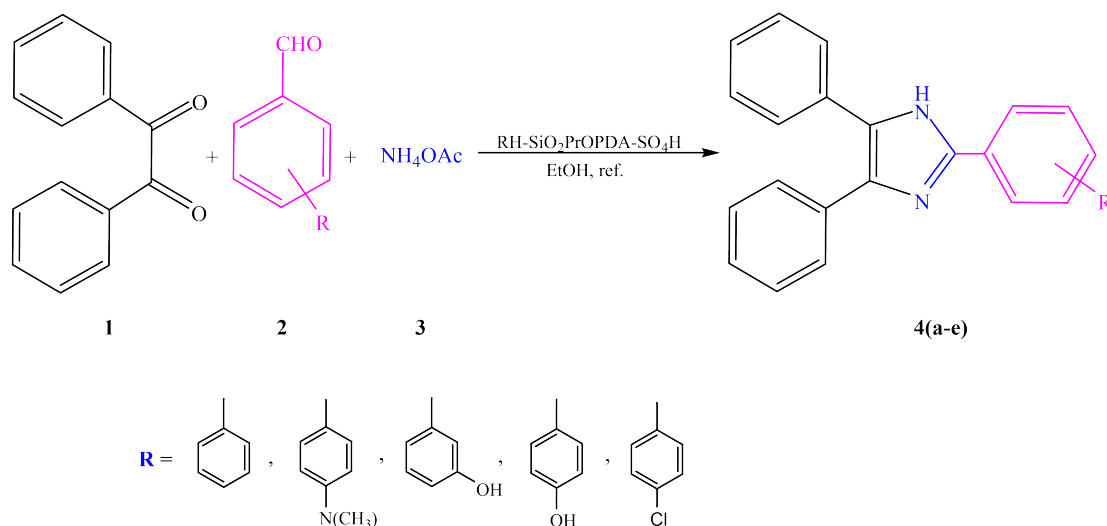
Scheme 2: Synthesis of 2,4,5-trisubstituted imidazole derivatives using RH-SiO$_2$PrOPDA-SO$_4$H as a catalyst.

2.4. Spectral Data for the Products

2,4,5-triphenylimidazole (**4a**): Yield: 99%; White solid; M.p. 267-269 °C (Lit. 267-269 °C) (16); IR (KBr) ū (cm^{-1}): 3315 (N–H), 3063 (Ar–H), 1662($C=N$); ^{1}H NMR (400 MHz, DMSO-d$_6$) δ (ppm): 12.79 (s, N–H), 8.10 (d, J = 8.0 Hz, 2H, Ar–H), 7.57 – 7.54 (m, 3H, Ar–H), 7.52 – 7.33 (m, 8H, Ar–H), 7.29 – 7.21 (m, 2H, Ar–H); MS (ESI): m/z = 296.2 [M$^+$].

4-(4,5-diphenylimidazol-2-yl)-N,N-dimethylaniline (**4b**): Yield: 74%; light yellow solid; M.p. 234-236 °C (Lit. 234-236 °C) (17); 3480 (N–H), 3059 (Ar–H), 2939, 2866 and 2800 (C–H), 1612($C=N$); ^{1}H NMR (400 MHz, DMSO-d$_6$) δ (ppm): 12.31 (s, N–H), 7.90

(d, J = 8.0 Hz, 2H, Ar−H), 7.50−7.20 (m, 10H, Ar−H), 6.79 (d, J = 8.0 Hz, 2H, Ar−H), 2.96 (s, 6H, N(CH_3)$_2$); MS (ESI): m/z = 339.4 [M$^+$].

3-(4,5-Diphenylimidazol-2-yl)phenol (**4c**): Yield: 71%; gray solid; M.p. 256–258 °C (Lit. 254–257 °C) (18); IR (KBr) ū (cm^{-1}): 3317 (O−H), 3190 (N−H), 3063 (Ar−H), 1666 (*C=N*); ^{1}H NMR (400 MHz, DMSO-d$_6$) δ (ppm): 12.61 (s, N−H), 9.56 (s, O−H), 7.55 − 7.49 (m, 5H, Ar−H), 7.44 (t, J = 8.0 Hz, 2H, Ar−H), 7.39 − 7.20 (m, 5H, Ar−H), 6.78 (d, J = 8.0 Hz, 2H, Ar−H); MS (ESI): m/z = 312.2 [M$^+$].

4-(4,5-diphenyl-1H-imidazol-2-yl)phenol (**4d**): Yield: 84%; beige solid; M.p. 232-235 °C (Lit. 233–236 °C) (19); IR (KBr) ū (cm^{-1}): 3313 (O−H), 3174 (N−H), 3032 (Ar−H), 1604 (*C=N*); ^{1}H NMR (400 MHz, DMSO-d$_6$) δ (ppm): 12.40 (s, N−H), 9.69 (s, O−H), 7.89 (d, J = 8.0 Hz, 2H, Ar−H), 7.53 (d, J = 8.0 Hz, 2H, Ar−H), 7.49 − 7.41 (m, 4H, Ar−H), 7.37 − 7.18 (m, 4H, Ar−H), 6.84 (d, J = 8.0 Hz, 2H, Ar−H); MS (ESI): m/z = 312.3 [M$^+$].

2-(4-chlorophenyl)-4,5-diphenylimidazole (**4e**): Yield: 44%; white solid; M.p. 258-261 °C (Lit. 257–260 °C) (20); IR (KBr) ū (cm^{-1}): 3182 (N−H), 3063 (Ar−H), 1666 (*C=N*); ^{1}H NMR (400 MHz, DMSO-d$_6$) δ (ppm): 12.69 (s, N−H), 8.08 (d, J = 8.0 Hz, 2H, Ar−H), 7.53−7.46 (m, 8H, Ar−H), 7.39−7.36 (m, 4H, Ar−H); MS (ESI): m/z = 330.3 [M$^+$].

3. RESULTS AND DISCUSSION

3.1. Fourier-Transform Infrared Spectroscopic Analysis (FT-IR)

Figure 1 shows the infrared spectrum of RH-SiO$_2$PrCl. The band near 3425 cm^{-1} is caused by the OH stretching vibration of silanol and water molecules adsorbed on the silica surface. Additionally, the band at 2958 cm^{-1} indicates the presence of CH stretching in the CH$_2$ propyl moiety (21, 22). The bending vibration of water molecules trapped in the silica matrix was detected as a strong peak at 1647 cm^{-1}. Moreover, bands at 1085, 698, and 462 cm^{-1} were assigned to the vibration modes of siloxane (Si-O-Si) (23, 24). A band at 698 cm^{-1} could be assigned to the chloro-carbon bond of the RH-SiO$_2$PrCl (25). These results indicate that CPTES was successfully incorporated into the silica matrix.

The FT-IR spectrum of the new catalyst RH-SiO$_2$PrOPDA-SO$_4$H in Figure 1 showed the presence of a band at 3433 cm^{-1}, indicating the presence of vibrations belonging to the N-H stretching group. Also, the band at 2947 cm^{-1} indicates the presence of a C-H stretching group vibration. The stretching vibration of the siloxane (Si-O-Si) appeared at 1111 cm^{-1}, which appeared at a higher frequency than compound RH-SiO$_2$PrCl. This indicated that the *o*-phenylenediamine was successfully immobilized onto RH-SiO$_2$PrCl. At the same point, the sulfuric acid functional group appears in the silica matrix with different absorption extents of the S=O stretching modes, which are located in the 1010-1080 cm^{-1} range, and the vibration band of S-O appears at 580 cm^{-1}. This indicates the success of stabilizing sulfonic acids (26) into the surfaces of RH-SiO$_2$PrOPDA-SO$_4$H.
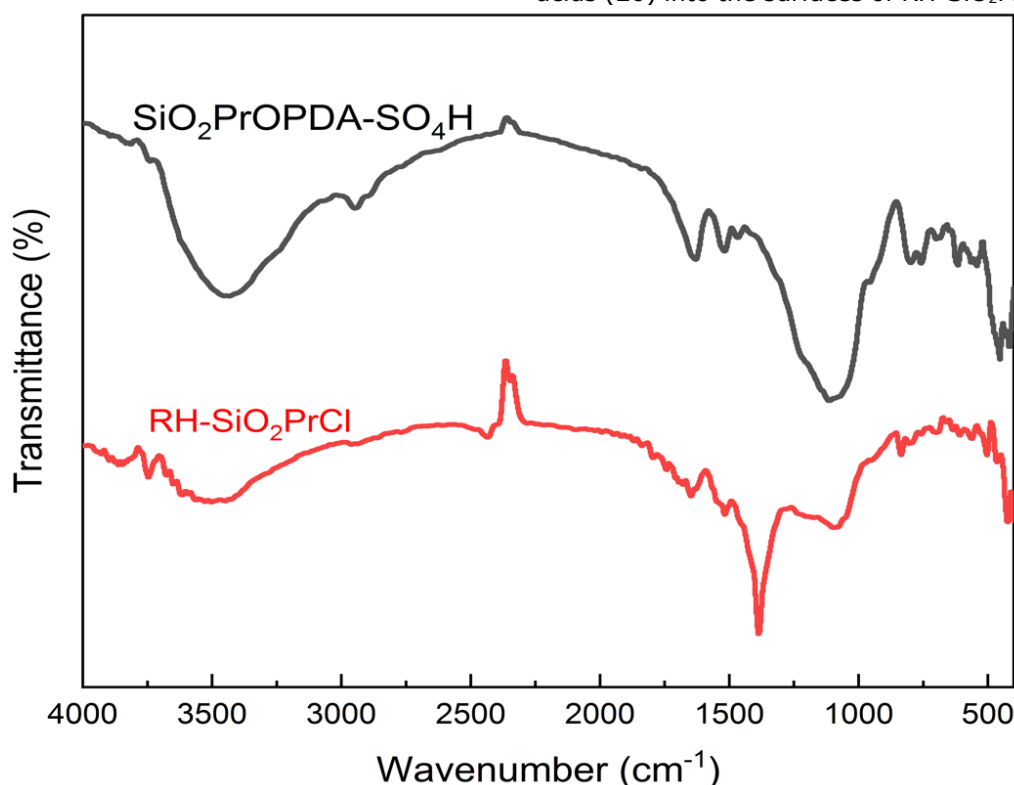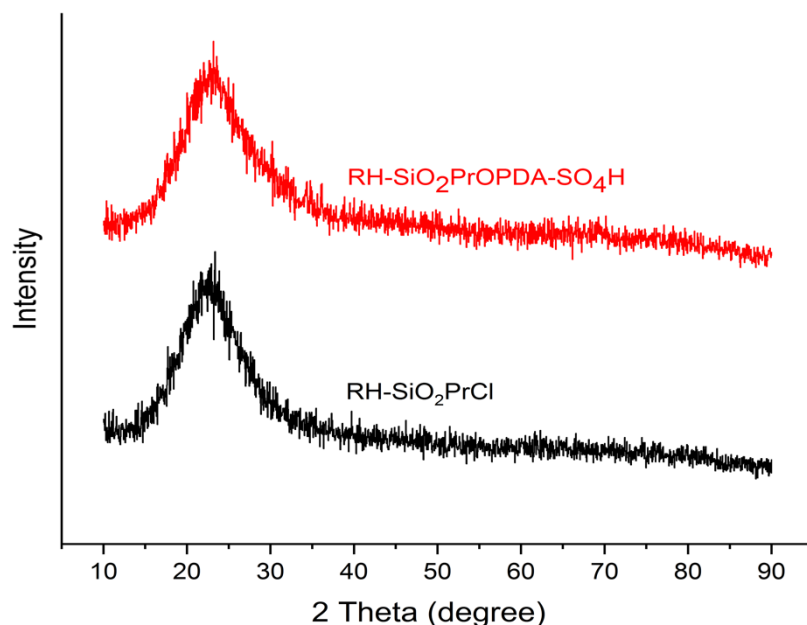

Figure 1: FT-IR analysis of RH-SiO$_2$PrCl and RH-SiO$_2$PrOPDA-SO$_4$H.

3.2. X-Ray Diffraction Analysis (XRD)

The XRD patterns of functionalized silica RH-SiO$_2$-PrCl and SiO$_2$PrOPDA-SO$_4$H show broad peaks at $2\theta=2$ in Figure 2, which indicates the amorphous structure of RH-SiO$_2$-PrCl and RH-SiO$_2$PrOPDA-SO$_4$H (27,28). However, no change occurred after fixation of o-phenylenediamine and sulfuric acid (29) on RH-SiO$_2$-PrCl in the new catalyst structure.


Figure 2: XRD analysis of RH-SiO$_2$PrCl and RH-SiO$_2$PrOPDA-SO$_4$H.

3.3. Nitrogen Adsorption Analysis

The specific surface area of the functionalized silica was 205.42 m^2/g, while for the new catalyst was 165 m^2/g. As a result, RH-SiO$_2$PrCl has a higher specific surface area caused by CPTES functioning as a directing agent for templates. This increase in porosity was attributed to the formation of a new structure of pores in the CPTES-silica composite (25). Adam and Andas (30) also reported similar findings. The reduction in surface area of the new catalyst is due to the acid treatment of the silica (31). In addition, the average pore diameters of RH-SiO$_2$PrCl and RH-SiO$_2$PrOPDA-SO$_4$H are 3.69 and 3.51 nm, respectively. The RH-SiO$_2$PrCl and RH-SiO$_2$PrOPDA-SO$_4$H samples exhibit type IV isotherms with an H3 hysteresis loop, which is typical of mesoporous solids. The pore size distribution is shown in the inset of Figure 3(a) and 3(b), where the pore size distribution is in the range of (5-20 nm) and belongs to mesoporous materials.
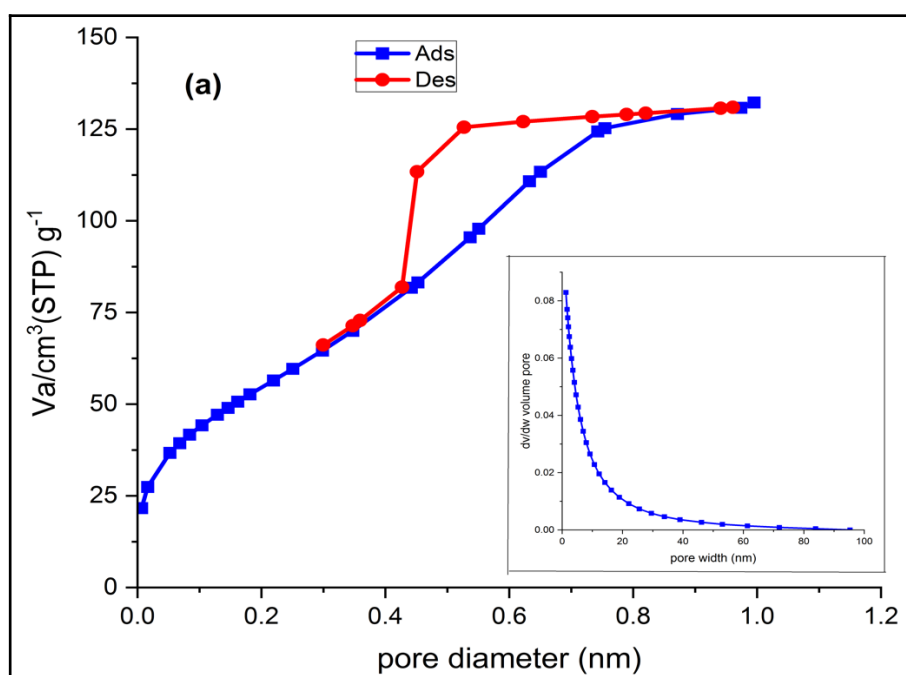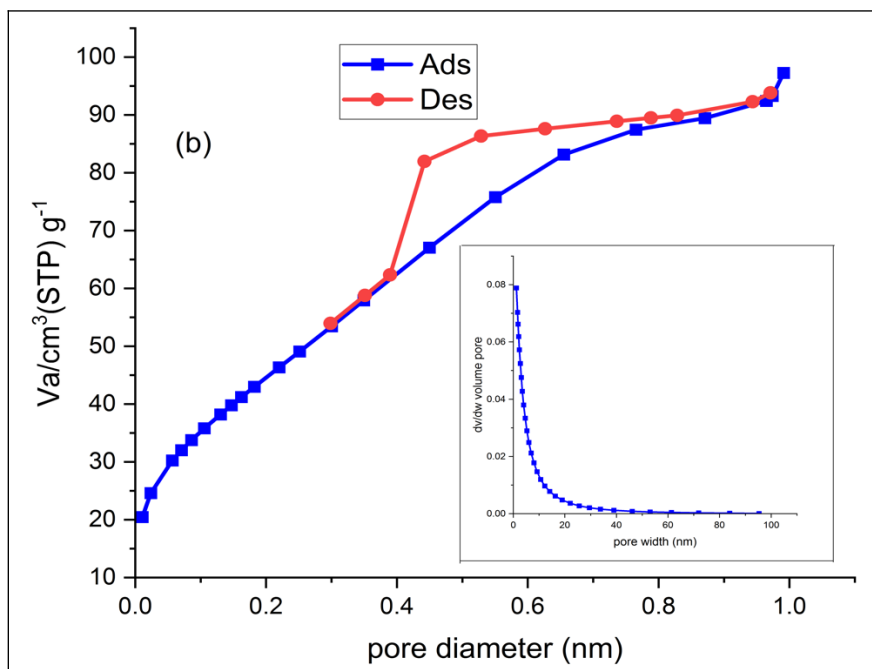
Figure 3: (a) N_2 adsorption–desorption isotherm and pore size distribution of RH-SiO$_2$PrCl. **(b)** N_2 adsorption–desorption isotherm and pore size distribution of RH-SiO$_2$PrOPDA-SO$_4$H.

3.4. Thermogravimetric Analysis (TGA)

The thermal stability of the samples of RH-SiO$_2$PrCl was evaluated by thermogravimetric analysis (TGA), and the weight loss observed was attributed to the degradation of the long-lasting components on the surface of the silica in Figure 4a. The results show that RH-SiO$_2$PrCl exhibits a weight change below 200 °C due to the loss of physically adsorbed water, and then experiences a stable weight loss below 600 °C, with decomposition weight loss increasing to 46% of the CPTES group in the matrix. At higher than 600°C, the silanol groups are converted into stable Si-O-Si siloxane bonds (32).

TGA analysis of RH-SiO$_2$PrOPDA-SO$_4$H (Figure 4(b)) shows a different type of decomposition than that of RH-SiO$_2$PrCl. The first decomposition occurs at temperatures below 300 °C due to water loss. In comparison, the second decomposition, start at temperatures between 300 and 600 °C, resulted in a weight loss of 65% due to the decomposition of the organic components immobilized on the catalyst surface. These results indicate that the acid catalyst is stable at the above temperatures.
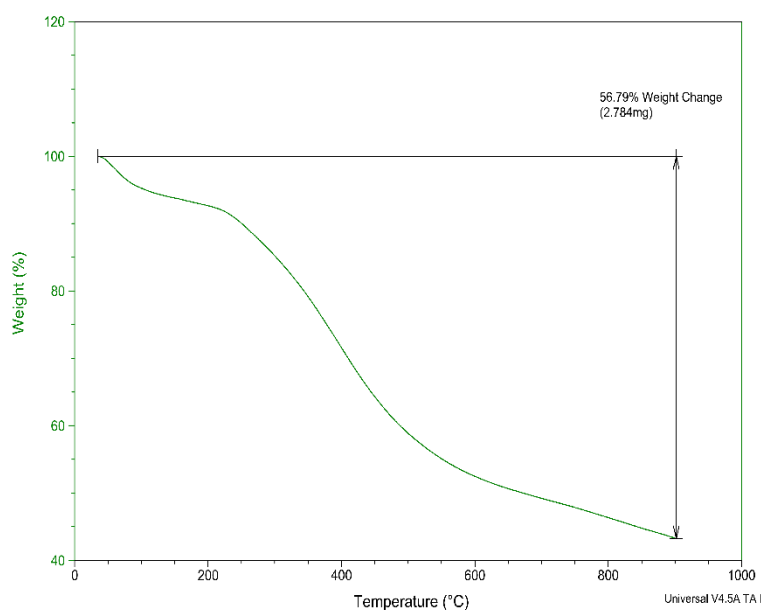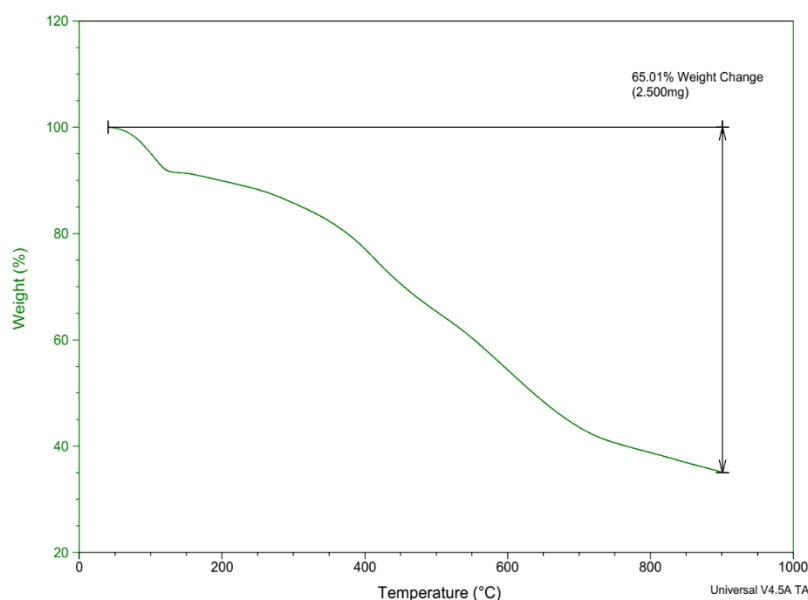
Figure 4: (a) TGA analysis of RH-SiO$_2$PrCl. **(b)** TGA analysis of RH-SiO$_2$PrOPDA-SO$_4$H.

3.5. Elemental Analysis (CHN)

The elemental analysis (CHNS) of the RH-SiO$_2$PrCl compound showed that the percentage of carbon and hydrogen reached 16.24% and 5.3%, respectively, as shown in Table 1. The elemental analysis of the RH-SiO$_2$PrOPDA-SO$_4$H compound indicated that the percentage of carbon, hydrogen, nitrogen, and Sulfur were 20.60%, 4.12%, 4%, and 3%, where the higher percentage of carbon, nitrogen, hydrogen, and Sulfur Results of treatment of functionalized silica with sulfuric acid and *o*-phenylenediamine.

Table 1: (CHNS) of the RH-SiO$_2$PrCl and RH-SiO$_2$PrOPDA-SO$_4$H.

Sample	C (%)	H (%)	N (%)	S (%)
RH-SiO$_2$PrCl	16.24	5.30	-	-
RH-SiO$_2$PrOPDA-SO$_4$H	20.60	5.12	4.00	3.00

3.6. Scanning Electron Microscopy–Energy Dispersive X-Ray (SEM/EDX)

FESEM analysis shows that RH-SiO$_2$PrCl in Figure 5 has a porous surface. In the FESEM image, the particles have irregular shapes. EDS analysis shows the presence of silicon, carbon, and oxygen in RH-SiO$_2$PrCl. The high carbon and oxygen content of silica in EDX analysis indicates the successful incorporation of CPTES into the silica matrix.

FESEM microscopic images of the new catalyst SiO$_2$PrOPDA-SO$_4$H are also shown in Figure 7. The surfaces were less porous than those of the functionalized silica (33), and EDS analysis is shown in Figure 8. The EDS spectrum showed peak oxygen density at 35.78%, carbon at 29.68%, silicon at 16.93%, nitrogen at 11.36%, and sulfur at 6.25. The increase in the percentage of these elements for the new catalyst indicates the succeeding incorporation of *o*-phenylenediamine with RH-SiO$_2$PrCl and sulfuric acid (34).
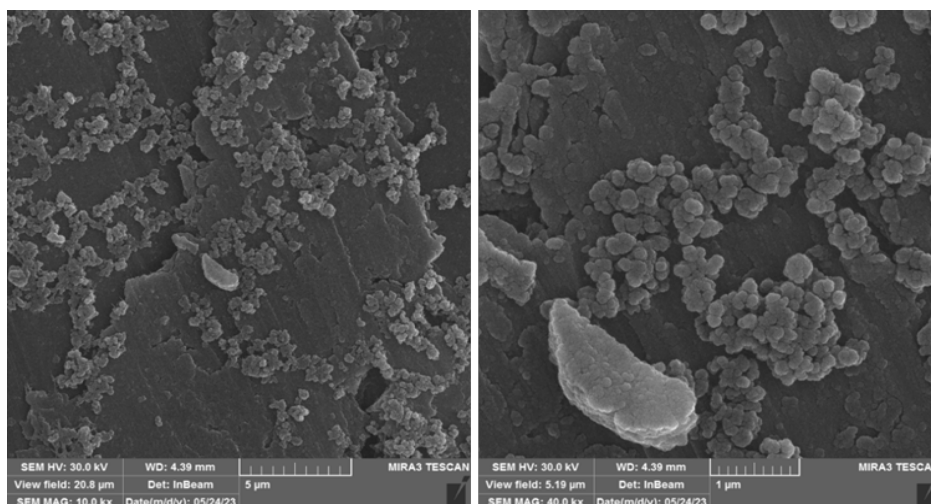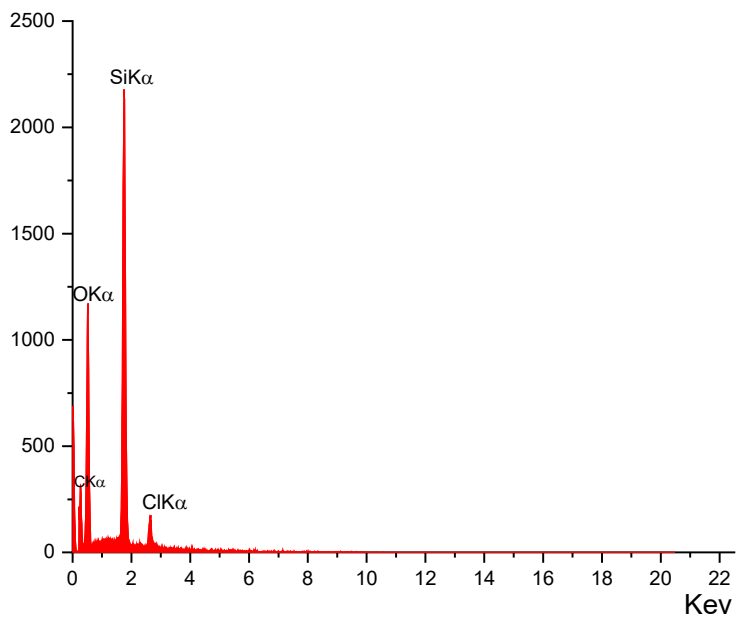

Figure 5: FESEM analysis of RH-SiO$_2$-PrCl.
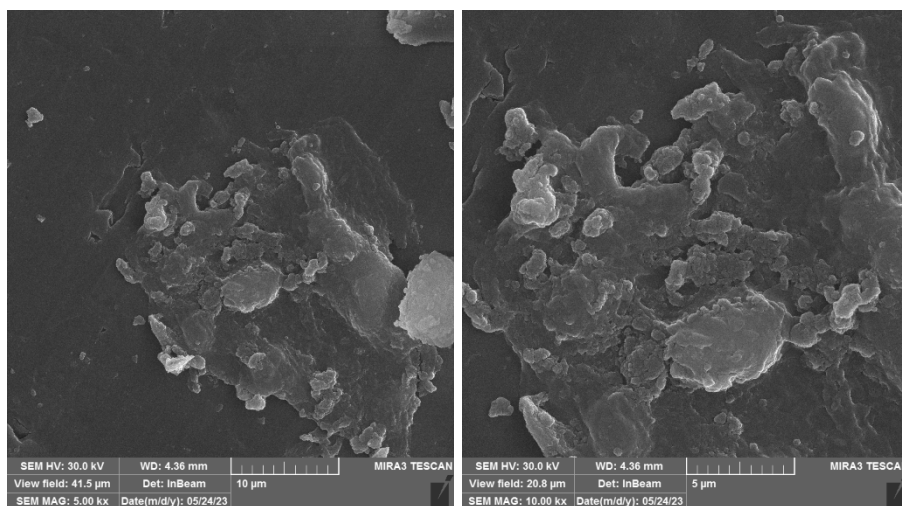
Figure 6: EDS analysis of RH-SiO$_2$PrCl.

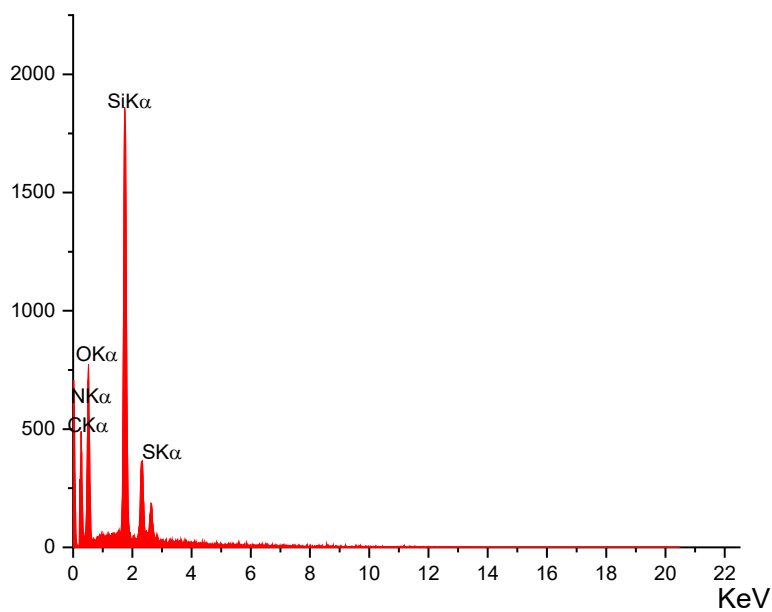**Figure 7:** FESEM analysis of SiO$_2$PrOPDA-SO$_4$H.

Figure 8: EDS analysis of SiO$_2$PrOPDA-SO$_4$H.

3.7. Atomic Force Microscopy (AFM)

The atomic force microscopy (AFM) images of RH-SiO$_2$PrCl and RH-SiO$_2$PrOPDA-SO$_4$H are shown in Figures 9 and 10, respectively. The structures appear pyramidal and irregular surfaces form. From comparing Figures 9 and 10, that note the surface of RH-SiO$_2$PrOPDA-SO$_4$H was less porous than functionalized silica RH-SiO$_2$-PrCl (35) due to add CPTES to silica. The estimated average roughness modulus (Ra) is 1.915 nm, and the root mean square roughness (Rrms) is 1.363 nm for the RH-SiO$_2$PrOPDA-SO$_4$H catalyst, which is larger than the roughness modulus and root square roughness of RH-SiO$_2$PrCl, 1.295 nm, and 845 pm, respectively. This change could be attributed to the successful modification the surface in RH-SiO$_2$PrCl by o-phenylenediamine and sulfuric acid.
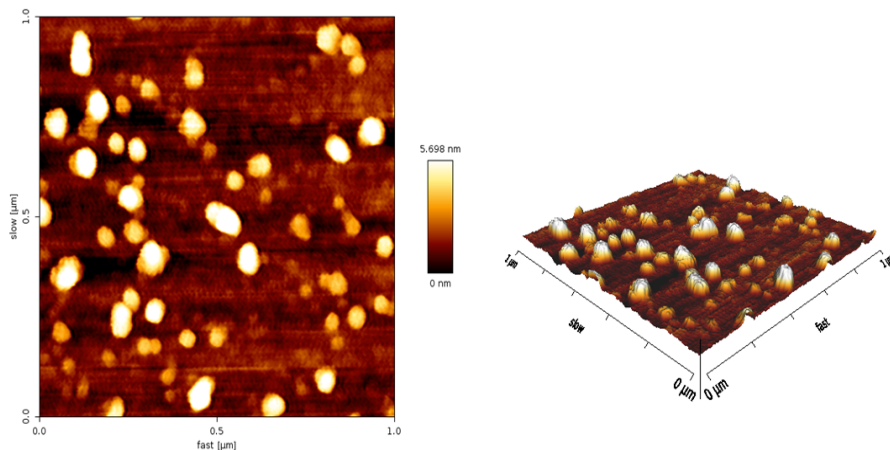
Figure 9: AFM 2D (in left) and 3D (in right) micrographs of RH-SiO$_2$PrCl.
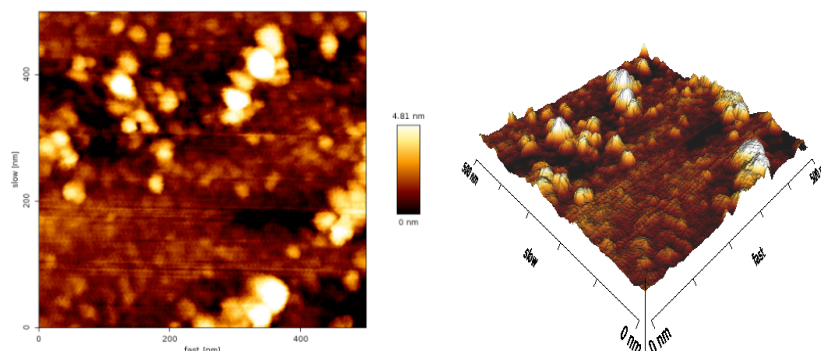
Figure 10: AFM 2D (in left) and 3D (in right) micrographs of RH-SiO$_2$PrOPDA-SO$_4$H.

3.8. Analysis with Transmission Electron Microscopy (TEM)

TEM microscopic images of RH-SiO$_2$PrCl functionalized silica shows spherical particles measuring between 10-15 nm. However, the particles are irregularly shaped, and visible porosity lines appear aligned, indicating the presence of a porous structure. This leads to a high surface area of RH-SiO$_2$PrCl functional silica (25, 36). As for the catalyst RH-SiO$_2$PrOPDA-SO$_4$H, the particle size is between 5-10 nm, and the distribution of particles could be seen with less dispersion than functional silica RH-SiO$_2$PrCl, and this indicates a decrease in the surface area due to the treatment of the functional silica with sulfuric acid.
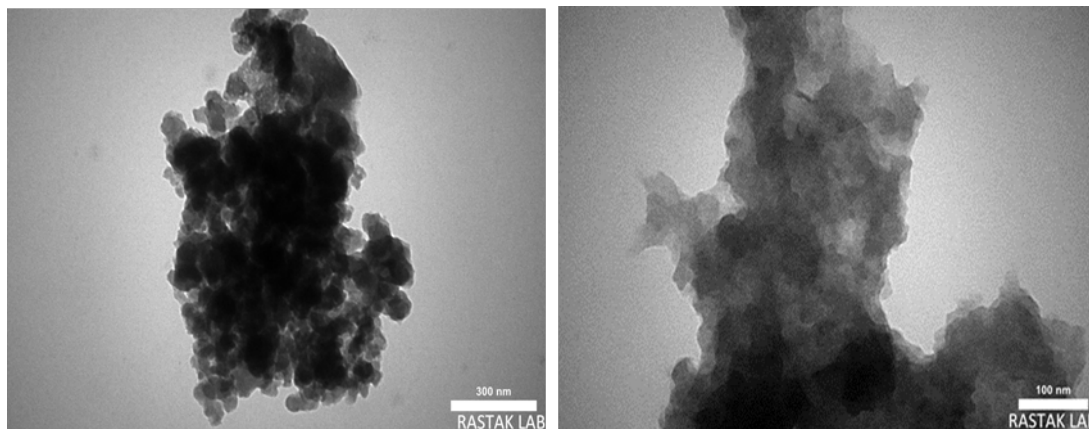
Figure 11: TEM images of RH-SiO$_2$PrCl.
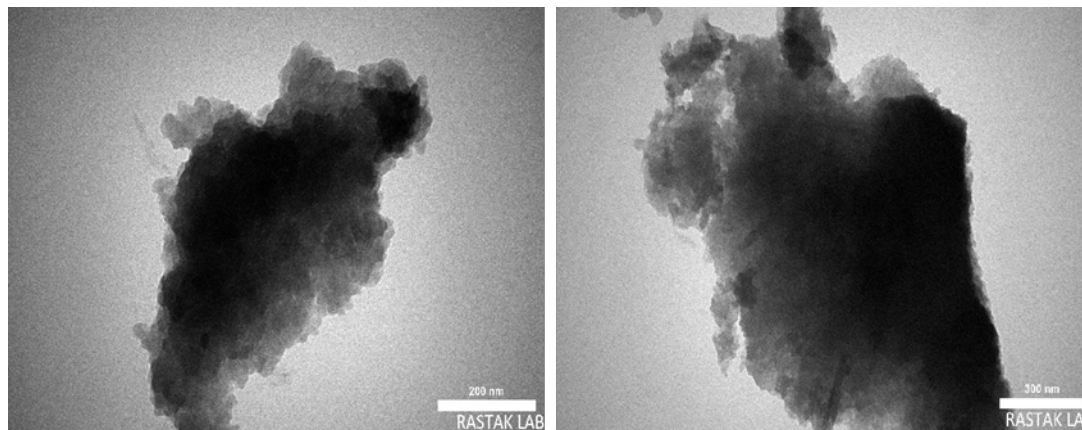
Figure 12: TEM images of RH-SiO$_2$PrOPDA-SO$_4$H.

3.9. Optimization of Reaction Conditions for Synthesis of 2,4,5-trisubstituted Imidazole Derivatives

The response between benzaldehyde, ammonium acetate, and benzil were selected as an example of a reaction that is intended to be studied (**4a**). The most effective conditions (Scheme 3) were determined as a result. Several different solvents and various molar ratios were examined for this process. The findings are listed in Tables 2 and 3. The highest yield percentage was achieved using ethanol as the solvent (Table 2, entry 3). The molar ratio demonstrated that the most effective and practical choice for the reaction was 1:1:5 (Table 3, entry 5). Additionally, the model reaction (**4a**) was conducted with different amounts of catalyst (Table 4). The highest percentage product was achieved when 0.04 g of catalyst was employed. (Table 4, entry 3). After successfully optimizing the reaction conditions, a series of 2,4,5-trisubstituted imidazole derivatives (**4a-e**) were prepared.

The spectral analyses of synthesized products were confirmed by comparison with those reported in the literature, and melting points were also recorded and compared with known compounds (16-20). ^{1}H NMR spectra exhibited the N–H proton of the imidazole ring in the downfield region, while FTIR spectra of the compounds (**4a-e**) showed packs at 3182–3480 and 1604–1666 cm^{-1} for the (N–H) and (C=N) groups, respectively.

Table 2: Effect of solvent on the synthesis of 2,4,5-triphenyl-1H-imidazole (**4a**).

Entry	Solvent	Yield %
1	H$_2$O	35
2	Methanol	46
3	Ethanol	99
4	CH$_3$CN	28
5	THF	71

Table 3: Effect of mole ratio on the synthesis of 2,4,5-triphenyl-1H-imidazole (**4a**).
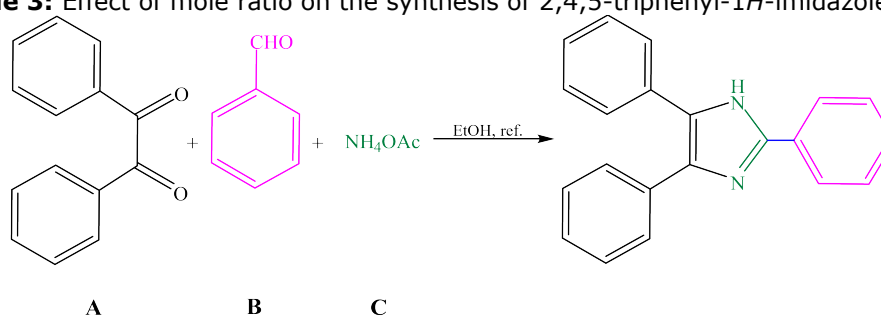
Entry	Mole ratio (A:B:C)	Yield %
1	1:1:1	92
2	1:1:2	39
3	1:1:3	42
4	1:1:4	96
5	1:1:5	99

Table 4: Effect of the catalyst amount on the synthesis of 2,4,5-triphenyl-1*H*-imidazole (**4a**).

Entry	Catalyst	Yield %
1	0.01	56
2	0.02	78
3	0.04	99
4	0.08	35
5	0.16	53

3.10. Reusability of the Catalyst

The benefit of using a new catalyst (RH-SiO$_2$PrOPDA-SO$_4$H) lies in its reusability, making it both environmentally friendly and cost-effective. To investigate the catalyst's recyclability, selected typical reactions were examined under identical optimized conditions. After each reaction, the catalyst was easily separated from the mixture by filtration and washed with dichloromethane. The dried catalyst was then retested for three consecutive cycles (Figure 13).

Figure 13: Reusability of the catalyst.

4. CONCLUSION

Based on some physical measurements, such as infrared spectra, nitrogen absorption analysis, and elemental analysis, it was found that *o*-phenylenediamine was f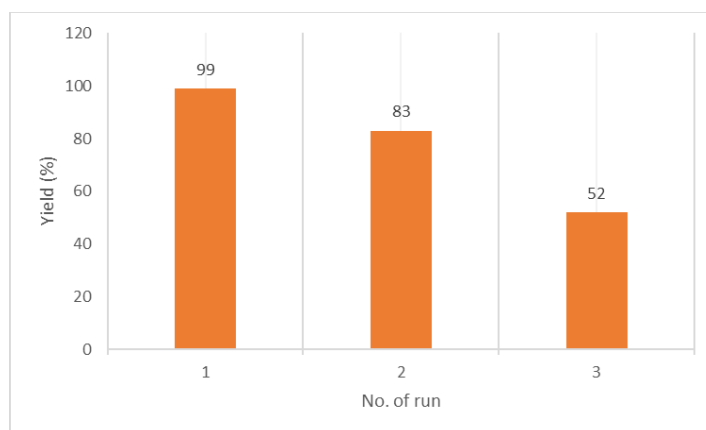unctionalized on the RH-SiO$_2$PrCl to prepare RH-SiO$_2$PrOPDA. Then, amine groups in RH-SiO$_2$PrOPDA were sulfonated by a simple reaction with diluted sulfuric acid to prepare RH-SiO$_2$PrOPDA-SO$_4$H. After the sulfonation process, the SO$_2$ functional groups were clearly shown in the catalyst's FT-IR. BET measurements showed the fixation of a 3-(chloropropyl)triethoxysilane molecule on the silica surface, which increased the specific surface area of RH-SiO$_2$PrCl. An efficient approach with a simple work-up and mild reaction condition procedure for preparation of 2,4,5-trisubstituted imidazole derivatives *via* condensation of ammonium acetate as an ammonia source, various aldehydes and benzil in ethanol as better solvent was presented, by using RH-SiO$_2$PrOPDA-SO$_4$H as the recyclable and inexpensive catalyst. The easy synthesis, safer reaction conditions, and reusable catalyst several times are the highlights of this procedure.

5. CONFLICT OF INTEREST

The authors have no relevant financial or non-financial interests to disclose.

6. ACKNOWLEDGMENTS

7. REFERENCES

1. Oluseun Adejumo I, Adebukola Adebiyi O. Agricultural solid wastes: Causes, effects, and effective management. In: Strategies of Sustainable Solid Waste Management [Internet]. IntechOpen; 2021. Available from: <URL>.

2. Siddique R, Cachim P. Waste and supplementary cementitious materials in concrete [Internet]. Waste and Supplementary Cementitious Materials in Concrete: Characterisation, Properties and Applications. Elsevier; 2018. 621 p. Available from: <URL>.

3. López-Alonso M, Martín-Morales M, Martínez-Echevarría MJ, Agrela F, Zamorano M. Residual biomasses as aggregates applied in cement-based materials. In: Waste and Byproducts in Cement-Based Materials [Internet]. Elsevier; 2021. p. 89–137. Available from: <URL>.

4. Phonphuak N, Chindaprasirt P. Types of waste, properties, and durability of pore-forming waste-based fired masonry bricks. In: Eco-Efficient Masonry Bricks and Blocks [Internet]. Elsevier; 2015. p. 103–27. Available from: <URL>.

5. Gnanamanickam SS. Rice and its importance to human life. In: Biological Control of Rice Diseases [Internet]. Dordrecht: Springer Netherlands; 2009. p. 1–11. Available from: <URL>.

6. Sangwan S, Singh R, Gulati S, Rana S, Punia J, Malik K. Solvent-free rice husk mediated efficient approach for synthesis of novel imidazoles and their

In vitro bio evaluation. Curr Res Green Sustain Chem [Internet]. 2022 Jan 1;5:100250. Available from: <URL>.

7. Lima SPB de, Vasconcelos RP de, Paiva OA, Cordeiro GC, Chaves MR de M, Toledo Filho RD, et al. Production of silica gel from residual rice husk ash. Quim Nova [Internet]. 2011;34(1):71–5. Available from: <URL>.

8. Ali HH, Hussein KA, Mihsen HH. Antimicrobial applications of nanosilica derived from rice grain husks. Silicon [Internet]. 2023 Aug 25;15(13):5735–45. Available from: <URL>.

9. Eshghi H, Hassankhani A. One-pot efficient beckmann rearrangement of ketones catalyzed by silica sulfuric acid. J Korean Chem Soc [Internet]. 2007 Aug 20;51(4):361–4. Available from: <URL>.

10. Riego JM, Sedin Z, Zaldívar J, Marziano NC, Tortato C. Sulfuric acid on silica-gel: An inexpensive catalyst for aromatic nitration. Tetrahedron Lett [Internet]. 1996 Jan 22;37(4):513–6. Available from: <URL>.

11. Manna J, Roy B, Sharma P. Efficient hydrogen generation from sodium borohydride hydrolysis using silica sulfuric acid catalyst. J Power Sources [Internet]. 2015 Feb 1;275:727–33. Available from: <URL>.

12. Adam F, Hello KM, Ali TH. Solvent free liquid-phase alkylation of phenol over solid sulfanilic acid catalyst. Appl Catal A Gen [Internet]. 2011 May 31;399(1–2):42–9. Available from: <URL>.

13. Tolomeu HV, Fraga CAM. Imidazole: Synthesis, functionalization and physicochemical properties of a privileged structure in medicinal chemistry. Molecules [Internet]. 2023 Jan 13;28(2):838. Available from: <URL>.

14. Ali HH, Mihsen HH, Hussain KA. Synthesis, characterization and antimicrobial studies of modified silica materials derived from rice husks. Bionanoscience [Internet]. 2023 Sep 28;13(3):1163–76. Available from: <URL>.

15. Tariq A, Mihsen HH, Saeed SI. Organic–inorganic hybrid modified silica synthesized from rice husks straw for effective uptake of Co(II), Ni(II), and Cu(II) ions from aqueous solutions. Biomass Convers Biorefinery [Internet]. 2023 Dec 28;1:1–13. Available from: <URL>.

16. Samai S, Nandi GC, Singh P, Singh MS. L-Proline: An efficient catalyst for the one-pot synthesis of 2,4,5-trisubstituted and 1,2,4,5-tetrasubstituted imidazoles. Tetrahedron [Internet]. 2009 Dec 5;65(49):10155–61. Available from: <URL>.

17. Noriega-Iribe E, Díaz-Rubio L, Estolano-Cobián A, Barajas-Carrillo VW, Padrón JM, Salazar-Aranda R, et al. In vitro and In silico screening of 2,4,5-Trisubstituted imidazole derivatives as potential xanthine oxidase and acetylcholinesterase inhibitors, antioxidant, and antiproliferative agents. Appl Sci [Internet]. 2020 Apr 22;10(8):2889. Available from: <URL>.

18. Ahmed NS, Hanoon HD. A green and simple method for the synthesis of 2,4,5-trisubstituted-1H-imidazole derivatives using acidic ionic liquid as an effective and recyclable catalyst under ultrasound. Res Chem Intermed [Internet]. 2021 Oct 19;47(10):4083–100. Available from: <URL>.

19. Hilal DA, Hanoon HD. Bronsted acidic ionic liquid catalyzed an eco-friendly and efficient procedure for synthesis of 2,4,5-trisubstituted imidazole derivatives under ultrasound irradiation and optimal conditions. Res Chem Intermed [Internet]. 2020 Feb 27;46(2):1521–38. Available from: <URL>.

20. Hanoon HD, Radhi SM, Abbas SK. Simple and efficient synthesis of 2,4,5-triarylsubstituted imidazole derivatives via a multicomponent reaction using microwave irradiation. In: AIP Conference Proceedings [Internet]. American Institute of Physics Inc.; 2019. p. 020005. Available from: <URL>.

21. Hello KM, Ibrahim AA, Shneine JK, Appaturi JN. Simple method for functionalization of silica with alkyl silane and organic ligands. South African J Chem Eng [Internet]. 2018 Jun 1;25:159–68. Available from: <URL>.

22. Mihsen HH, Rfaish SY, Abass SK, Sobh HS. Synthesis and characterization of silica-thioamide hybrid compounds derived from rice husk ash with expected biological and catalytic activity. J Glob Pharma Technol [Internet]. 2018;10(11):590–8. Available from: <URL>.

23. Saravanan S, Dubey RS. Synthesis of SiO_2 nanoparticles by sol-gel method and their optical and structural properties. Rom J Inf Sci Technol [Internet]. 2020;23(1):105–12. Available from: <URL>.

24. Abbas SK, Hassan ZM, Mihsen HH, Eesa MT, Attol DH. Uptake of nickel(II) ion by Silica-o-Phenylenediamine derived from rice husk ash. Silicon [Internet]. 2020 May 18;12(5):1103–10. Available from: <URL>.

25. Adam F, Osman H, Hello KM. The immobilization of 3-(chloropropyl)triethoxysilane onto silica by a simple one-pot synthesis. J Colloid Interface Sci [Internet]. 2009 Mar 1;331(1):143–7. Available from: <URL>.

26. Elzanati E, Abdallah H, Farg E, Ettouney RS. Enhancing the esterification conversion using pervaporation. J Eng Sci Technol [Internet]. 2018;13(4):990–1004. Available from: <URL>.

27. Adam F, Hello KM, Osman H. Esterification via saccharine mediated silica solid catalyst. Appl Catal A Gen [Internet]. 2009 Aug 31;365(2):165–72. Available from: <URL>.

28. Sobh HS, Mihsen HH. Synthesis of functionalized silica from rice husks containing C-I end group. Baghdad Sci J [Internet]. 2019 Dec 1;16(4):886–91. Available from: <URL>.

29. Vijayalakshmi U, Vaibhav V, Chellappa M, Anjaneyulu U. Green synthesis of silica nanoparticles and its corrosion resistance behavior on mild steel. J Indian Chem Soc. 2015;92(5):675–8.

30. Adam F, Andas J. Amino benzoic acid modified silica—An improved catalyst for the mono-substituted product in the benzylation of toluene with benzyl chloride. J Colloid Interface Sci [Internet]. 2007 Jul 1;311(1):135–43. Available from: <URL>.

31. Esmaili S, Khazaei A, Ghorbani-Choghamarani A, Mohammadi M. Silica sulfuric acid coated on $SnFe_2O_4$ MNPs: Synthesis, characterization and catalytic applications in the synthesis of polyhydroquinolines. RSC Adv [Internet]. 2022 May 12;12(23):14397–410. Available from: <URL>.

32. Permatasari N, Sucahya TN, Dani Nandiyanto AB. Review: Agricultural wastes as a source of silica material. Indones J Sci Technol [Internet]. 2016 Apr 1;1(1):82. Available from: <URL>.

33. Nah HY, Parale VG, Jung HNR, Lee KY, Lim CH, Ku YS, et al. Role of oxalic acid in structural formation of sodium silicate-based silica aerogel by ambient pressure drying. J Sol-Gel Sci Technol [Internet]. 2018 Feb;85(2):302–10. Available from: <URL>.

34. Guedes R, Prosdocimi F, Fernandes G, Moura L, Ribeiro H, Ortega J. Amino acids biosynthesis and nitrogen assimilation pathways: A great genomic deletion during eukaryotes evolution. BMC Genomics [Internet]. 2011 Dec 22;12(S4):S2. Available from: <URL>.

mer-[InCl₃(C₅D₅N)₃]₂·C₅D₅N: A New D₅-pyridine Derivative of Indium(III) Chloride Complex

Ali Tuna[1,2]* (iD), **Anastassios C. Papageorgiou[3]** (iD), **Anssi Peuronen[2]** (iD), **Pekka Peljo[1]** (iD), **Günther Knör[4]** (iD)

[1]   Research Group of Battery Materials and Technologies, Department of Mechanical and Materials Engineering,   University of Turku, FI-20014 Turku, Finland
[2]   Department of Chemistry, University of Turku, FI-20014 Turku, Finland
[3]   Turku Bioscience Center, University of Turku and Åbo Akademi University, FI-20520 Turku, Finland
[4]   Department of Environmental Technology, Magistrate Linz, A-4041 Linz, Austria

Abstract: In this study, we report the crystal structure of a meridional octahedral pyridine-indium(III) chloride adduct, *mer*-trichlorotris(d₅-pyridine)indium(III)·0.5(d₅-pyridine),   InCl₃(C₅D₅N)₃·0.5(C₅D₅N), which exhibits an unreported molecule-to-solvent ratio compared to other substituted and unsubstituted pyridine-indium(III) chloride adducts described in earlier literature. The bonding characteristics of this d₅-pyridine complex are compared to analogous complexes that have already been reported. Furthermore, the role of this metal complex in indium insertion into corrole ligands is discussed.

1. INTRODUCTION

Geometric isomerism is a fundamental aspect in coordination complexes where the complex molecules have the same empirical formula, but where the arrangement of the ligand molecules around the metal center are distinctively different. Isomers may exhibit different physical, chemical and even biological properties due to different geometries, such as cis, trans, facial (*fac*), and meridional (*mer*) isomerism (1). In *fac*-isomerism, three identical ligands are positioned on one face of the octahedron, creating a triangular arrangement around the central metal atom. The *mer*-isomer features three identical ligands and a metal atom in a single plane, forming a T-shaped arrangement around the central metal atom (2). This configuration reduces intra-ligand repulsions, making it more suitable for smaller metal complexes, such as high-valent metal centers (1,3). The distinct spatial arrangements of ligands in *fac*- and *mer*-isomers result in differences in chemical reactivity,

physical properties, and biological activity, highlighting their importance in the study and application of coordination and inorganic chemistry (4–6).

Metal activation through the coordination of pyridine or other solvents occurs when metal complexes interact with the coordinated solvent molecules, thereby affecting the reactivity and properties of the metals involved whereas coordinated solvent pushes the electrons through the metal center to make it more active as the metal center becomes more electro-positive (7–9). Such activation is very useful in metalation, where it can aid the metal centers in forming new complexes with higher yields while preventing the formation of mixtures of products (9,10).

Corroles are conjugated 18π-electron aromatic ring system carrying one direct pyrrole–pyrrole linkage. They can be considered as ring-contracted porphyrin

derivatives. Many metallocorroles have been successfully synthesized and investigated in the last decades. The first attempts at the synthesis of an indium corrole compound were made in the late 80s, but complete characterization of this compound was unsuccessful for many years (11,12). Recently, the first successful indium insertion into the 5,10,15-tris(pentafluorophenyl)corrole was achieved and the obtained indium corrole complex was successfully characterized by relevant analytical techniques (13). Remarkably, the observed Soret- and Q-band patterns of the formed indium corrole complex in the absorption spectrum shows a hypsochromic shift which indicates a significant change of HOMO-LUMO gap as well as an extent of conjugated π-system in order to structural modifications influenced the electronic transitions in the direction of successful metal insertion. We believe that when the metalation process of indium corrole is conducted in d5-pyridine, an *in situ* formed intermediate, trichlorotris(d5-pyridine)indium(III) plays a key role in the metalation process. Here, we explore this claim, by isolating and characterizing *mer*-trichlorotris(d5-pyridine)indium(III) (**1**) and by using it as a metal precursor in the metalation of two different corrole ligands (Scheme 1).

R = 4-carboxymethylphenyl or 4-methylphenyl
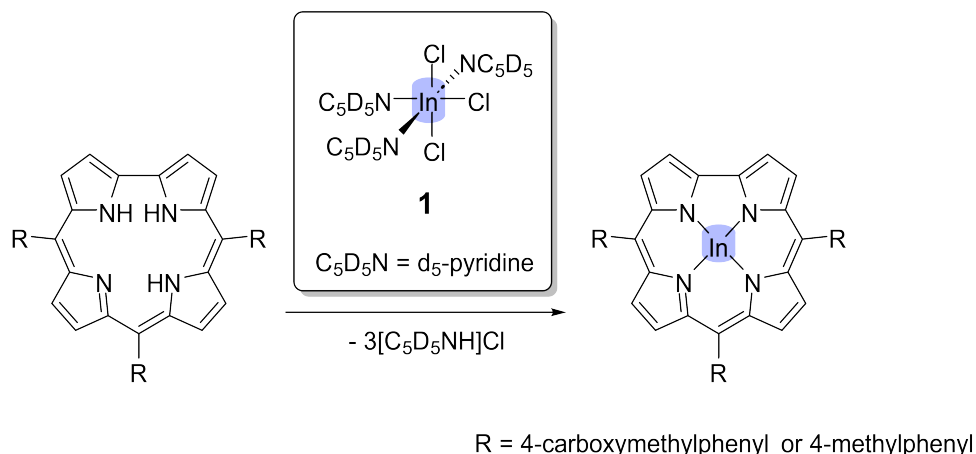
Scheme 1. *mer*-Trichlorotris(d5-pyridine)indium(III) (**1**) and its role in indium insertion to corroles.

2. MATERIALS AND METHODS

2.1. Materials
Indium(III) chloride (anhydrous, 99.95%) was purchased from ABCR Chemie, Germany. D5-pyridine (99.8 atom%D) was purchased from ARMAR Isotopes, Germany. Anhydrous pyridine (99.9%) and other supplements were obtained from VWR, Finland. Free-base corrole ligands were synthesized at the University of Rome "Tor Vergata" (Italy) according to the literature (18).

2.2. Preparation of Single Crystals and Powder
300.4 mg of anhydrous indium(III) chloride was dissolved in an excess amount of d5-pyridine (5-5.1 mL) and the mixture was refluxed for 30 min under an Ar atmosphere until the solution became transparent. The solution was then divided into two vials of relatively equal amount (2.5 mL) in a fume hood. One vial was covered with a lid and small holes were opened to allow slow evaporation of the solution at room temperature. The other vial was poured into a 25 mL single-neck round-bottom flask, and d5-pyridine was removed under reduced pressure at 50 °C to give a white powder. Crystals (**1**) were obtained from the first vial.

2.3. Preparation of Indium Corroles
mer-Trichlorotris(d5-pyridine)indium(III) obtained from the second vial as a white powder was added in small portions to a solution of the free-base ligand (50 mg each, 1 eq) in anhydrous pyridine at reflux, until indium insertions were completed. The metalation reaction progress was monitored by UV-Vis spectroscopy where the spectra were measured with a Cary 60 spectrophotometer.

2.4. Single Crystal Measurement
A suitable crystal of **1** was selected and immobilized on a polyamide loop using a small amount of paratone oil. X-ray diffraction data were collected on a Rigaku Micromax-007 HF generator equipped with a HyPix-6000HE hybrid photon counting detector. The crystal was kept at room temperature during data collection. The X-ray data were processed with CrysAlisPro (18).

Crystal Data for **1**: monoclinic, space group $P2_1$ (no. 4), $a = 13.3862(5)$ Å, $b = 8.9223(3)$ Å, $c = 17.0910(7)$ Å, $\beta = 101.666(4)°$, $V = 1999.11(13)$ Å^3, $Z = 4$, $T = 293(2)$ K, $\mu(Cu\ K\alpha) = 13.188$ mm^{-1}, $Dcalc = 1.713$ g/cm^3, 12904 reflections measured ($5.28° \leq 2\Theta \leq 136.498°$), 5305 unique ($R_{int} = 0.0839$, $R_{sigma} = 0.0626$) which were used in all calculations. The final R_1 was 0.0991 (I > 2σ(I)) and wR_2 was 0.2776 (all data).

2.5. Refinement
With Olex2 as the graphical interface, the structure was solved using intrinsic phasing in the SHELXT (19,20) structure solution program and refined by employing Least Squares minimization. All D atoms

were refined isotropically using idealized C-D sp^2 geometries and distances with $U_{iso(H)}$ = 1.2U_{eq}(C), whereas non-D atoms were refined anisotropically. In the final model, the atoms of the aromatic rings of the disordered d$_5$-pyridine groups could not be refined without geometrical restriction and were instead subjected to a rigid refinement procedure. Details of data collection and structure refinement are summarized in Table 1.

3. RESULTS AND DISCUSSIONS

The indium(III) chloride complex of d$_5$-pyridine (**1**) crystallizes in the monoclinic space group $P2_1$ with two *mer*-trichlorotris(d$_5$-pyridine)indium(III) molecules and one d$_5$-pyridine molecule within the asymmetric unit resulting in a 2:1 ratio between the complex units and non-coordinated solvate molecules (Figure 1). The three d$_5$-pyridine ligands are coordinated meridionally in a T-shape geometry around the metal center. One of the d$_5$-pyridine ligands was found to be disordered in two sites rotated by approximately 23° over the C$_5$N plane.
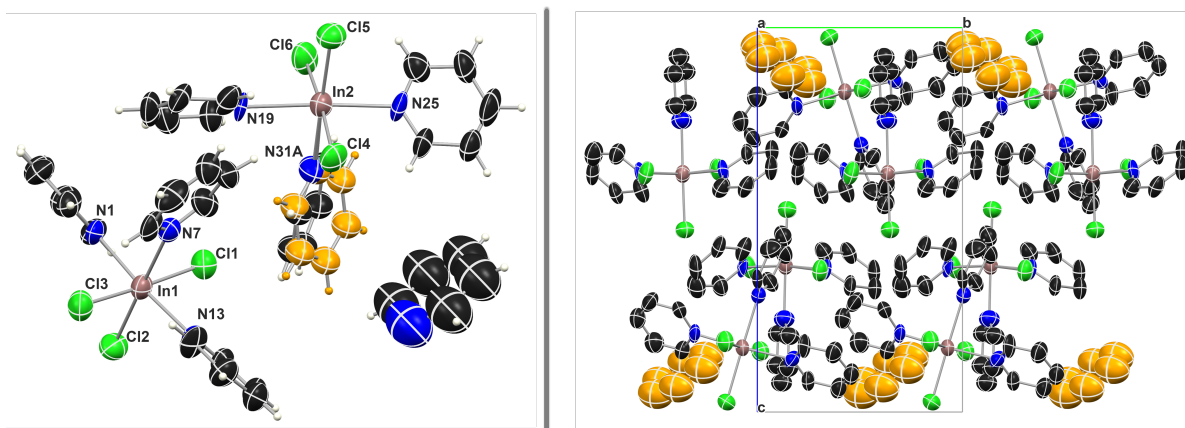
Figure 1   *Left*: Illustration of the asymmetric unit of the crystal structure of **1** where the disordered d$_5$-pyridine ligand at In2 is also shown. *Right*: Crystal packing of **1** viewed along the crystallographic *a*-axis (D atoms and disordered d$_5$-pyridine ligands omitted). The displacement ellipsoids are drawn at the 50% probability level.

Table 1 shows a list of crystallographic parameters of analogous trichlorotris(pyridine)indium(III) structures that have already been introduced in the literature and contain pyridine (**2**) (14), 4-methylpyridine (**3**) (15), and 4-ethylpyridine (**4**) (16) as ligands (Figure 2). Despite their similar molecular structures, **1** and **2** crystallize in different space groups and exhibit a different number of solvent molecules in their crystal lattices. Compounds **1** and **2** are crystallized with surrounding solvate molecules whereas the **3** and **4** are crystallized without any solvate molecules (Table 1). As mentioned above, compound **1** crystallizes in the monoclinic $P2_1$ space group with 0.5 non-coordinated d$_5$-pyridine solvate molecules per complex unit in the crystal lattice. This indicates a more complex packing arrangement, potentially influenced by the deuterium atoms in d$_5$-pyridine, which can affect intermolecular interactions and packing density.

The second structure (**2**), crystallizing in the orthorhombic $C222_1$ space group, differs from **1** by having an equivalent number of complex molecules to pyridine solvate molecules in the structure. The presence of one complex and one solvent molecule in the asymmetric unit as well as the higher crystallographic symmetry suggest a more straightforward packing arrangement in **2** compared to **1**. The use of d$_5$-pyridine instead of non-deuterated pyridine could lead to subtle differences in the crystal packing and intermolecular forces due to the slightly

different mass and vibrational properties of deuterium compared to hydrogen. These differences may contribute to the observed differences in the space group and stoichiometry between the two structures. Overall, the choice of solvate molecule and the resulting crystal packing appear to significantly influence the crystallographic properties and symmetry of the resulting structures.

The In–N bond lengths in **1** are systematically longer compared to the other analogous complexes **2**-**4** (Table 2). This difference is most evident for the N–In bond located trans to the Cl atom, while the N–In–N bond lengths are, in comparison, rather similar. The different In–N bond lengths between the complexes indicate subtle differences in the N-donor capabilities of the ligands, while crystal packing effects can also play a role. For example, in **2** – the closest analogue to **1** – the crystal packing is mostly dictated by the intermolecular interactions between the complex molecules and the solvent, while in **1** several intermolecular C–H···π and π···π contacts can be observed between the In complexes. This difference between these two crystal structures most likely arises from the higher complex-to-lattice solvent ratio in **2**. The observed differences in the In–N distances between the two crystal structures can also be related to isotopic effects. Isotopic substitution, in which atoms of different isotopes are present, may influence bond lengths owing to variations in atomic masses

and vibrational frequencies. Heavier isotopes tend to vibrate at lower frequencies, leading to slightly different bond lengths. Therefore, the minor variations in the bond lengths observed in the structures could be attributed to the presence of different isotopes of hydrogen, such as deuterium, resulting in subtle changes in the local bonding environment. A further comparison of all the four structures **1**-**4** shows that the In–Cl bonds appear to be less sensitive to changing the N-donor, although there is some variation in the In–Cl bonds lengths which does not seem to be systematical.
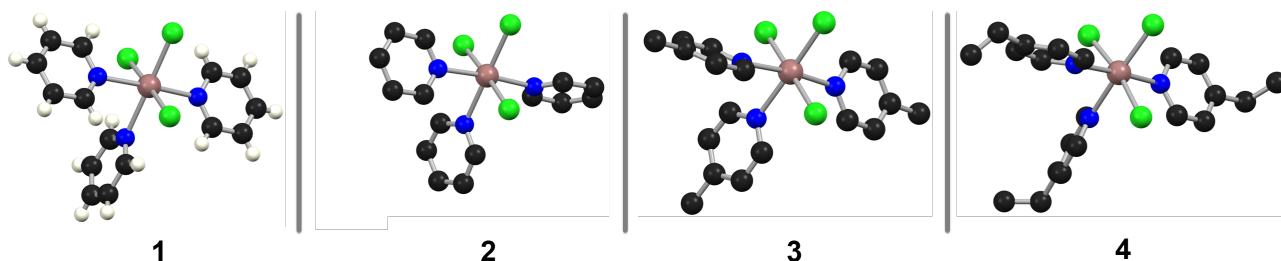
Figure 2   The complex molecule of structure 1 (this work) compared to 2-4 drawn using crystallographic data obtained from the Cambridge Structural Database (17). The ^{2}H atoms of 1 are highlighted while ^{1}H atoms are omitted from the figure.

Table 1   Crystal data for compound **1** (this work) compared to different *mer*-trichlorotris(pyridine)indium(III) derivatives (**2-4**) obtained from previous literature.

Parameters	1	2	3	4
pyridine derivative	d$_5$-pyridine	pyridine	4-methylpyridine	4-ethylpyridine
empirical formula	C$_{17.5}$Cl$_3$D$_{17.5}$InN$_{3.5}$	C$_{20}$H$_{20}$Cl$_3$InN$_4$	C$_{18}$H$_{21}$Cl$_3$InN$_3$	C$_{21}$H$_{27}$Cl$_3$InN$_3$
molecular weight	515.63 Da	537.58 Da	500.56 Da	542.64 Da
crystal system	monoclinic	orthorhombic	triclinic	triclinic
space group	$P2_1$	$C222_1$	$P\bar{1}$	$P\bar{1}$
a	13.3862(5) Å	9.117(7) Å	9.3240(3) Å	9.7330(1) Å
b	8.9223(3) Å	16.83(2) Å	13.9580(6) Å	20.826(2) Å
c	17.0910(7) Å	14.66(1) Å	16.7268(7) Å	25.311(3) Å
α	90°	90°	84.323(2)°	74.970(1)°
β	101.666(4)°	90°	80.938(2)°	83.31(2)°
γ	90°	90°	78.274(3)°	89.26(2)°
V	1999.11(13) Å^3	2250(5) Å^3	2099.8(2) Å^3	4920.0(9) Å^3
Z	4	4	4	8
ρ_{calc}	1.713 g/cm^3	1.586 g/cm^3	1.58 g/cm^3	1.465 g/cm^3
temperature	293 K	293 K	203 K	293 K
X-ray source	Cu Kα	Mo Kα	Mo Kα	Mo Kα
R$_1$	0.0991	0.050	0.035	0.0953
deposited on	this work	28/03/1985	28/12/2001	05/01/2001
published year	this work	1984	2013	2000
reference	this work	(14)	(15)	(16)
CSD reference	this work	CILYUR	WIBVEK	WOPYIJ

The formed *mer*-trichlorotris(d$_5$-pyridine)indium(III) structure is believed to play a key role in the metalation process of indium corrole formation in pyridine (11,13). To prove this claim, *mer*-trichlorotris(d$_5$-pyridine)indium(III) was used as a metal precursor in the metalation of corrole using different corrole ligands (Figure 3 and Figure 4). These UV-vis spectra suggest that the two selected corroles undergo metalation using the *mer*-trichlorotris(d$_5$-pyridine)indium(III) as a metal precursor.

Table 2   The average bond lengths for *mer*-trichlorotris(pyridine-derivative)indium(III) structures containing different pyridine derivatives (**1**-**4**). For **1**, only one of the two distinct complex molecules in the asymmetric unit is shown.

Bond	1[a]	2	3	4
In – N1	2.321(2) Å	2.302(7) Å	2.312(2) Å	2.279(1) Å
In – N2	2.410(2) Å	2.377(2) Å	2.324(2) Å	2.341(8) Å
In – N3	2.332(2) Å	2.302(7) Å	2.311(2) Å	2.304(1) Å
In – Cl1	2.479(5) Å	2.476(2) Å	2.482(2) Å	2.413(6) Å
In – Cl2	2.464(5) Å	2.471(8) Å	2.461(1) Å	2.468(6) Å
In – Cl3	2.472(6) Å	2.471(8) Å	2.475(4) Å	2.480(6) Å

[a] This work.
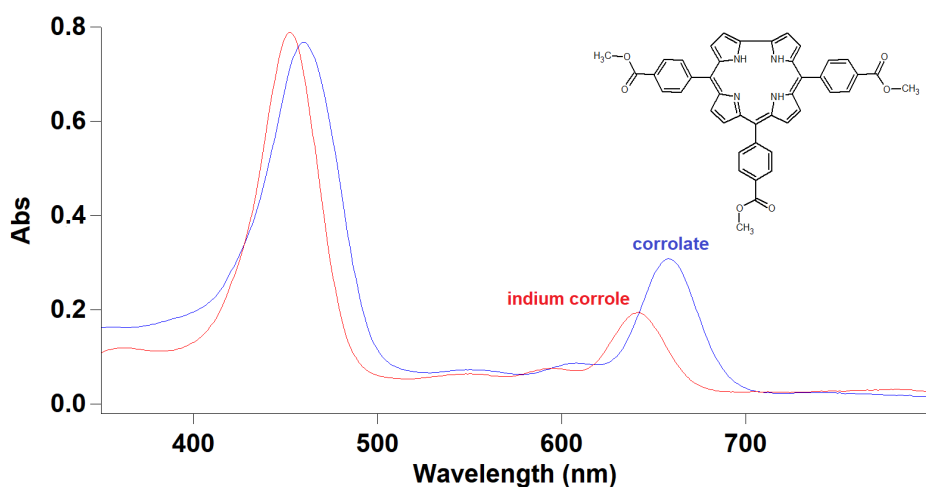
Figure 3   UV-vis spectra of free-base corrole as a corrolate anion and formed indium corrole complex using the 5,10,15-tris(4-carboxymethylphenyl)corrole ligand in pyridine.
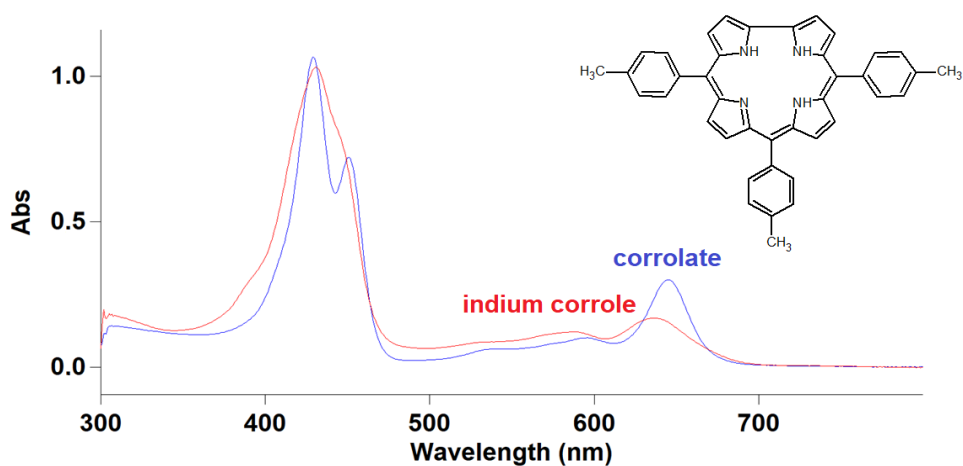
Figure 4   UV-Vis spectra of free-base corrole as a corrolate anion and formed indium corrole complex using the 5,10,15-tris(4-methylphenyl)corrole ligand in pyridine.

4. CONCLUSIONS

In conclusion, *mer*-trichlorotris(d_5-pyridine)indium(III) complex was crystallized and its crystal structure was determined and compared to analogous non-deuterated In complexes. The crystal structure indicates that changing H atoms to D atoms has a noticeable effect on the coordination environment of the In center, and a more profound effect on the crystal packing arrangements due to the crystallization of the complexes with different amounts of lattice solvent per complex molecule (0, 0.5, or 1). A further investigation showed that indium metal could be successfully transferred from the *mer*-trichlorotris(d_5-pyridine)indium(III) to different free-base corroles, 5,10,15-tris(4-carboxymethylphenyl)corrole and 5,10,15-tris(4-methylphenyl)corrole, respectively. The obtained UV-vis spectra were compared with the experimental data presented in a previous study on indium corrole synthesis as a result of successful indium corrole formations as significant spectral shifts on Soret and Q band patterns. In parallel, we are currently investigating the preparation of new indium corrole complexes with more detailed characterization data and further crystallization attempts to elucidate the first X-ray structure of an indium corrole.

5. ACKNOWLEDGMENT

Supplementary Materials: The following supporting information can be downloaded at:.

Conflict of Interest: All authors declare that they have no conflicts of interest.

Data Availability Statement: CCDC 2392242 contains the supplementary crystallographic data for this paper. These data can be obtained free of charge via http://www.ccdc.cam.ac.uk/conts/retrieving.html (or from the CCDC, 12 Union Road, Cambridge CB2 1EZ, UK; Fax: +44 1223 336033; E-mail: deposit@ccdc.cam.ac.uk).

Author Contributions:
A. T.: conceptualization, data curation, formal analysis, investigation, methodology, validation, visualization, writing—original draft preparation, writing—review and editing.
A. C. P.: formal analysis, writing—original draft preparation, writing—review and editing.
A. P.: data curation, validation, visualization, writing—original draft preparation, writing—review and editing.
P.P.: resources, supervision, writing—review and editing.
G. K.: supervision, validation, writing—review and editing.

6. REFERENCES

1. Janiak C, Meyer HJ, Gudat D, Kurz P. Riedel Moderne Anorganische Chemie [Internet]. Riedel E, Meyer HJ, editors. De Gruyter; 2018 [cited 2024 Dec 2]. Available from: https://www.degruyter.com/document/doi/10.1515/9783110441635/html

2. Hoffmann R, Beier BF, Muetterties EL, Rossi AR. Seven-coordination. A molecular orbital exploration of structure, stereochemistry, and reaction dynamics. Inorganic Chemistry. 1977;16(3):511–22.

3. Ehnbom A, Ghosh SK, Lewis KG, Gladysz JA. Octahedral Werner complexes with substituted ethylenediamine ligands: a stereochemical primer for a historic series of compounds now emerging as a modern family of catalysts. Chem Soc Rev [Internet]. 2016 [cited 2024 Dec 2];45(24):6799–811. Available from: https://xlink.rsc.org/?DOI=C6CS00604C

4. Sato H, Yamagishi A. Application of the ΔΛ isomerism of octahedral metal complexes as a chiral source in photochemistry. Journal of Photochemistry and Photobiology C: Photochemistry Reviews [Internet]. 2007 Oct [cited 2024 Dec 2];8(2):67–84. Available from: https://linkinghub.elsevier.com/retrieve/pii/S1389556707000457

5. Scharwitz MA, Ott I, Gust R, Kromm A, Sheldrick WS. Synthesis, cellular uptake and structure-activity relationships for potent cytotoxic trichloridoiridium(III) polypyridyl complexes. Journal of Inorganic Biochemistry [Internet]. 2008 Aug [cited 2024 Dec 2];102(8):1623–30. Available from: https://linkinghub.elsevier.com/retrieve/pii/S0162013408000810

6. Von Zeiewsky A, Belser P, Hayoz P, Dux R, Hua X, Suckling A, et al. Tailor made coordination compounds for photochemical purposes. Coordination Chemistry Reviews [Internet]. 1994 May [cited 2024 Dec 2];132:75–85. Available from: https://linkinghub.elsevier.com/retrieve/pii/001085459480026X

7. Soro B, Stoccoro S, Minghetti G, Zucca A, Cinellu MA, Gladiali S, et al. Synthesis of the First C-2 Cyclopalladated Derivatives of 1,3-Bis(2-pyridyl)benzene. Crystal Structures of [Hg(N-C-N)Cl], [Pd(N-C-N)Cl], and [Pd$_2$ (N-C-N)$_2$ (μ-OAc)]$_2$ [Hg$_2$ Cl$_6$]. Catalytic Activity in the Heck Reaction. Organometallics [Internet]. 2005 Jan 1 [cited 2024 Dec 2];24(1):53–61. Available from: https://pubs.acs.org/doi/10.1021/om040102o

8. Hietkamp S, Stufkens DJ, Vrieze K. Activation of C☐H bonds by transition metals. Journal of Organometallic Chemistry [Internet]. 1979 Mar [cited 2024 Dec 2];168(3):351–61. Available from: https://linkinghub.elsevier.com/retrieve/pii/S0022328X00832167

9. Gouterman M, Sayer P, Shankland E, Smith JP. Porphyrins. 41. Phosphorus mesoporphyrin and phthalocyanine. Inorganic Chemistry. 1981;20(1):87–92.

10. Knör G. Photophysik und Photochemie von Porphyrinkomplexen des Antimons: Entwicklung homogener photokatalytischer Modellsysteme zur Nutzung, Umwandlung und Speicherung von Solarenergie [Doctoral Thesis]. [Regensburg, Germany]: University of Regensburg; 1994.

11. Paolesse R, Licoccia S, Boschi T. Towards the periodic table of metallocorrolates: synthesis and characterization of main group metal complexes of octamethylcorrole. Inorganica Chimica Acta [Internet]. 1990 Dec [cited 2024 Dec 2];178(1):9–12. Available from: https://linkinghub.elsevier.com/retrieve/pii/S0020169300881256

12. Weaver JJ. CORROLES [Internet] [Doctoral Thesis]. [California, USA]: California Institute of Technology; 2005. Available from: https://core.ac.uk/download/pdf/11810364.pdf

13. Tuna A, Peljo P, Paolesse R, Knör G. Tris(pentafluorophenyl)corrolatoindium(III) – A Long-awaited Metallocorrole: Synthesis and Characterization. Journal of the Turkish Chemical Society Section A: Chemistry [Internet]. 2024 May 15 [cited 2024 Dec 2];11(2):803–12. Available from: http://dergipark.org.tr/en/doi/10.18596/jotcsa.1425456

14. Jeffs SE, Small RWH, Worrall IJ. Structure of the 4:1 complexes formed by pyridine and the Group III halides InCl3 and TlCl3: mer-trichlorotris(pyridine)indium(III)–pyridine (1/1), [InCl3(C5H5N)3].C5H5N, and mer-trichlorotris(pyridine)thallium(III)–pyridine (1/1), [TlCl3(C5H5N)3].C5H5N. Acta Crystallogr C Cryst Struct Commun [Internet]. 1984 Aug 15 [cited 2024 Dec 2];40(8):1329–31. Available from: https://scripts.iucr.org/cgi-bin/paper?S010827018400785X

15. Hepp AF, Schuff JD, Williams JN, Duraj SA, Fanwick PE. Preparation and Single-Crystal X-Ray Structures of Four Related Mixed-Ligand 4-Methylpyridine Indium Halide Complexes [Internet]. NASA; 2013. Available from: https://ntrs.nasa.gov/api/citations/20130011563/downloads/20130011563.pdf

16. Green M, Norager S, Moriarty P, Motevalli M, O'Brien P. On the synthesis and manipulation of InAs quantum dots. Journal of Materials Chemistry. 2000;10(8):1939–43.

17. Groom CR, Bruno IJ, Lightfoot MP, Ward SC. The Cambridge Structural Database. Acta Crystallogr B Struct Sci Cryst Eng Mater [Internet]. 2016 Apr 1 [cited 2024 Dec 2];72(2):171–9. Available from: https://scripts.iucr.org/cgi-bin/paper?S2052520616003954

18. Paolesse, R., Nardis, S., Sagone, F., Khoury R. G. Synthesis and functionalization of meso-aryl-substituted corroles. *J. Org. Chem.* 2001, 66, 550–556.

19. CrysAlis[Pro]: An All-in-one Software Package for Single Crystal X-ray Diffraction [Internet]. Rigaku, Inc.; Available from: https://rigaku.com/products/crystallography/x-ray-diffraction/application-notes/px018-crysalispro-software-package-single-crystal

20. Dolomanov OV, Bourhis LJ, Gildea RJ, Howard JAK, Puschmann H. *OLEX2*: a complete structure solution, refinement and analysis program. J Appl Crystallogr [Internet]. 2009 Apr 1 [cited 2024 Dec 2];42(2):339–41. Available from: https://scripts.iucr.org/cgi-bin/paper?S0021889808042726

21. Sheldrick GM. SHELXT–Integrated space-group and crystal-structure determination. Acta Crystallographica Section A: Foundations and Advances. 2015;71(1):3–8.

Synthesis, Characterization, and Photophysical Properties of Novel BODIPY and [Zn(dipyrrin)₂] Complexes from an Asymmetrical Dipyrromethene Ligand

Gökhan Sevinç[1*] iD

[1]Bilecik Seyh Edebali University, Faculty of Science, Department of Chemistry, TR 11100 Bilecik, Turkiye.

Abstract: In this study, novel homoleptic BF_2 and Zn (II) complexes derived from an asymmetric dipyrromethene ligand were synthesized, with their chemical structures elucidated through NMR, and HRMS techniques. The photophysical characteristics in solution were investigated utilizing UV-visible absorption and fluorescence spectroscopy. The experimental results are clarified through Density Functional Theory (DFT) calculations and electron-hole analysis. Theoretical analyses have demonstrated that, following excitation, both electrons and holes remain confined exclusively within the BODIPY core. The charge-transfer transitions were identified between reciprocal ligands, which are responsible for the redshift observed in the main absorption band, as evidenced by electron-hole analysis. The energy levels of the frontier molecular orbitals converge contingent upon the incorporation of naphthyl and p-methoxyphenyl substituents. When analyzed under an inert nitrogen atmosphere, the compounds exhibited considerable thermal stability. Despite the similarity in the TGA curves of the complexes, the formation of the homoleptic complex resulted in an enhancement in degradation temperatures. This study indicates that chromophoric dipyrromethene complexes present advantageous prospects for advancing the development of novel materials that are both photostable and thermostable, effectively integrating charge transfer with low energy within the visible and/or near-infrared spectra.

1. INTRODUCTION

Dipyrromethene (dpm) compounds, also known as dipyrrins, represent a significant group of conjugated, bipyrrolic chelators that have gained growing interest in recent years. These compounds are organic moieties capable of coordinating with various metal atoms to form stable complex structures. Dipyrromethene-metal complexes are characterized by notable features such as photostability and thermal stability, facile chemical synthesis, and significant absorptive capacity, particularly within the visible spectrum (1–3). The π-conjugation within these bis-pyrrolic systems enhances the efficient absorption of visible light via π – π* transitions. Dipyrrins are crucial in current chemical research due to their easy synthesis, intriguing photophysical properties, and diverse self-assembled architectures. Dipyrrin compounds are particularly significant as they serve as precursors to porphyrin and dipyrromethene-BF_2 complexes known as BODIPYs (4,5). Porphyrins can be synthesized artificially and are also found in numerous natural substances, including hemoglobin and chlorophyll (6). BODIPY (4,4-difluoro-4-bora-3a,4a-diaza-*s*-indacene) dyes (4,5,7,8) are actively researched within diverse applications such as chemical and biological sensors (9–12), two-photon absorption (13,14), dye-sensitized solar cells (15,16), and cellular imaging (17,18). This is owing to their pronounced fluorescence in the visible spectrum, distinct absorption and emission peaks, inherent stability, and adaptability to chemical modifications. Dipyrrin compounds are typically synthesized through the condensation of aromatic aldehydes and pyrroles, resulting in the formation of symmetric products. (1,3). BODIPY compounds are generally synthesized from aromatic aldehyde and pyrrole starting materials. The dipyrromethane

intermediates obtained in the first stage are converted to dipyromethane ligands by oxidation in the presence of *p*-chloranil (Tetrachloro-p-benzoquinone) or DDQ (2,3-Dichloro-5,6-dicyano-1,4-benzoquinone). The complexation is completed with $BF_3.OEt_2$ in the presence of an organic base such as triethylamine (Scheme 1).
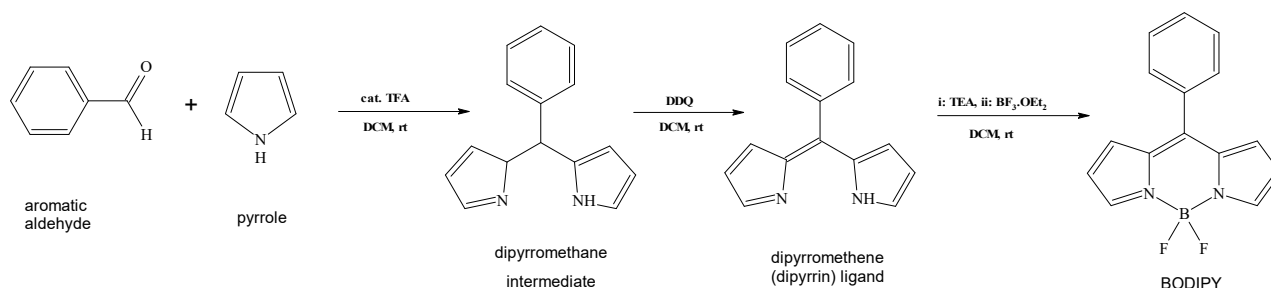
Scheme 1: The sample reaction in BODIPY synthesis from an aromatic aldehyde (benzaldehyde) and pyrrole starting materials.

The literature documents the synthesis, characterization, and diverse applications of these symmetrical dipyrrins and their corresponding metal or BODIPY complexes (1–3). Research on asymmetrically structured dipyrrins and their metal complexes, including BF_2, is limited (19,20). This scarcity may be due to the challenges in synthesizing asymmetrical dipyrromethenes. The asymmetric structure can be imparted via Knoevenagel reactions from alpha alkyl substituted dipyrromethene or generally BODIPY compounds. In these reactions, binary symmetric products (distyryl products) are mostly obtained. An alternative to this method, which limits the yield of response, is to use different pyrroles to obtain asymmetric dipyrromethenes. Therefore, in order to make complex purification procedures, a 1,3-dimethyl-BODIPY scaffold can be used, which can only lead to monostyryl products (19,20). Apart from this, one of the key steps in the formation of the asymmetrical dipyrrin backbone is the condensation of pyrrole carboxaldehyde and pyrrole derivatives. When the substituent groups on the pyrroles are the same, symmetric dipyrins are obtained, and when they are different, asymmetric dipyrrin ligands are obtained.

The transition metal coordination chemistry of dipyrrine ligands, which are notable for their intense absorption in the red region of the spectrum, is a current topic (1–3). Coordination of dipyrromethenes with the Zn (II) gives $M(L)_2$ type homoleptic complexes with distorted tetrahedral geometry. In this search to incorporate the hyperconjugated asymmetrical structures, Zn(II) was preferred as the metal ion of choice for comparing with the Boron (III) coordination because the closed-shell (d^{10}) configuration of Zn (II) and allowing for faster theoretical calculations. Unlike the previous studies, pyrroles containing aromatics such as phenyl and naphthyl groups at the 2,4-positions of the pyrrole were used, and thus, increased conjugation was aimed. To achieve this, two novel dyes featuring asymmetric structures were synthesized from the 2,4-diaryl-1*H*-pyrrole derivatives. The dipyrromethene framework, incorporating different aromatic groups at the -α (-1, -9) and -β (-3, -7) positions, was obtained. The structural elucidation of the compounds was conducted utilizing $^1H/^{13}C$ NMR,

and HRMS techniques. The effect of the asymmetric structure and metal/semimetal coordination on the absorption and fluorescence characteristics of the compounds was ascertained. The relationships between chemical structure and photophysical properties were examined through the application of density functional theory (DFT) calculations. In the final step, the impact of substituted groups, conjugation, and asymmetric formation on the thermal properties of the compounds was examined through thermogravimetric analysis (TGA).

2. EXPERIMENTAL SECTION

2.1. Materials and Instruments
The novel compounds **NafmetBDP** and **NafmetZn** were synthesized utilizing reagents sourced from commercial suppliers. The solvents employed in the absorption and fluorescence measurements were of spectroscopic grade. Reaction progress was monitored using thin-layer chromatography (TLC) aluminum sheets coated with silica gel (Merck 60 F254) and illuminated with a UV lamp. Column chromatography was conducted employing silica gel 60 with a mesh size of 230 - 400. High-resolution mass spectra were acquired using the Agilent 6224 LC/MS spectrometer, operating in both positive and negative modes. ^1H-NMR spectra were acquired using a Bruker Avance 500 MHz spectrometer in deuterated chloroform ($CDCl_3$) with tetramethylsilane (TMS) as the internal standard, whereas ^{13}C-NMR spectra were recorded at a frequency of 125 MHz in the same solvent. Chemical shifts (δ) were given in ppm relative to the solvent peaks ($CDCl_3$: ^1H: δ 7.26; ^{13}C: δ 77.4). The coupling constants (*J*) were reported in hertz. Thermogravimetric analysis (TGA) of the dyes was performed by heating the compounds with the Exstar SII TGA/DTA 7200 device under nitrogen flow with a heating rate of 10 °C / min in the range of 30-1100 °C. 2,4-bis[4-methoxyphenyl]-1*H*-pyrrole and 2-[4-methoxyphenyl]-4-[1-naphthyl]-1*H*-pyrrole were synthesized following the experimental procedure outlined in Refs (21,22).

2.2. Synthesis
2.2.1. Synthesis of the compound NafmetBDP

400 µL of phosphoryl chloride was slowly added to dimethyl formamide (400 µL) at -4 °C, then stirred for 10 minutes at 0 °C. The ice bath was removed before stirring for another 10 minutes. Subsequently, the ice bath was reapplied, and 10 minutes thereafter, dichloroethane (2 mL) was introduced. Following 5 minutes of stirring, a solution of 2,4-bis[methoxyphenyl]-1*H*-pyrrole (400 mg, 1.79 mmol) in dichloroethane (10 mL) was added to the reaction mixture in a dropwise manner. After the addition, the ice bath was removed, and the mixture was refluxed for 30 minutes. The mixture cooled to room temperature; NaOAc (1.62 g, 19.7 mmol, 10 mL H_2O) was added, followed by 30 minutes of reflux. The mixture was cooled to rt, and water (30 mL) was added. The organic phase was extracted with chloroform (2 x 30 mL). Evaporating the solvent under reduced pressure yielded the formylated pyrrole used without purification. The formyl pyrrole (150 mg, 0.49 mmol) and 2-[4-methoxyphenyl]-4-[1-Naphthyl]-1*H*-pyrrole (146 mg, 0.49 mmol) were dissolved in 5 mL of anhydrous dichloromethane. Phosphoryl chloride (50 mL) was added in five portions under cooling at 0 °C and stirred for 2 hours. The mixture was warmed to ambient temperature, after which 5 mL of dichloromethane was added and stirred for another hour. Water (50 mL) was added, and the mixture was extracted with chloroform (2 × 30 mL), with subsequent evaporation of the solvent under reduced pressure yielding 220 mg of crude dipyrromethene ligand. The ligand 100 mg (0.19 mmol) was dissolved in 50 mL of DCM, then N,N-diisopropylethylamine (1.0 mL) and BF_3.OEt_2 (1.00 mL) were added dropwise. After stirring the mixture at room temperature for 12 hours, it was neutralized with saturated $NaHCO_3$ (100 mL) and washed with water; the organic layer was then dried over Na_2SO_4, filtered, and the solvent was removed. Silica gel chromatography (eluent: $CHCl_3$) yielded **NafmetBDP** as a red powder. Yield: 64 mg (10%). ^{1}H-NMR (500 MHz, $CDCl_3$): δ[ppm]: 3.81 (s, 3H), 3.90 (s, 6H), 6.67 (s, 1H), 6.89-6.86 (m, 3H), 7.04-7.01 (dd, *J*:9.0 Hz, 4H), 7.17, (s, 1H), 7.35 (d, *J*:9.0 Hz, 2H), 7.49 (d, *J*:7.0 Hz, 1H), 7.58-7.55 (m, 3H), 7.96-7.92 (m, 2H), 7.99 (d, *J*:9.0 Hz, 2H), 8.05 (d, *J*:9.0 Hz, 2H), 8.24 (d, *J*:9.0 Hz, 1H). ^{13}C-NMR (125 MHz, $CDCl_3$) δ: 161.0, 160.8, 160.2, 158.1, 156.1, 145.5, 142.6, 139.3, 135.6, 134.6, 134.0, 132.1, 131.2, 130.0, 129.1, 128.9, 128.4, 128.3, 126.5, 126.2, 126.1, 125.8, 125.4, 125.1, 125.0, 120.8, 118.3, 114.5, 114.1, 113.9, 113.8, 55.3. HRMS (Q-TOF-ESI) m/z Calcd: 636.23960 ($C_{40}H_{31}BF_2N_2O_3$), found: 636.23846 [M]⁻, Δ = 1.79 ppm.

2.2.2. Synthesis of the compound NafmetZn

A mixture of the dipyrromethene ligand synthesized in the prior step (100 mg, 0.17 mmol) and $Zn(OAc)_2$.$2H_2O$ (25 mg, 0.11 mmol) was dissolved in n-butanol (15 mL) and subjected to stirring at 120 °C for a duration of 4 hours. After cooling to room temperature, the reaction mixture was filtered, and the resulting blue solid was washed with 10 mL of cold EtOH and then dried in vacuum. Blue-Brown solid, yield: 152 mg (72%). ^{1}H-NMR (500 MHz, $CDCl_3$): δ[ppm]: 3.52 (s, 6H), 3.71 (s, 6H), 3.82 (s, 6H), 6.40 (s, 2H), 6.58 (s, 2H), 6.74-6.69 (m, 12H), 7.02 (s, 2H), 7.16-7.15 (m, 4H), 7.66-7.41 (m,

16H), 7.87 (d, *J*:8.5 Hz, 2H), 7.96 (d, *J*:8.0 Hz, 2H). ^{13}C-NMR (125 MHz, $CDCl_3$) δ: 159.6, 158.8, 133.9, 133.7, 132.4, 130.1, 128.6, 128.5, 128.3, 128.2, 127.9, 127.7, 126.9, 126.1, 125.7, 117.7, 115.3, 113.6, 113.3, 113.2, 55.3, 55.2, 55.1. HRMS (Q-TOF-ESI) m/z Calcd: 1238.39612 ($C_{80}H_{62}N_4O_6Zn$), found: 1239.39946 [M+H]⁺, Δ = 2.81 ppm.

2.3. Photophysical Measurements

Compounds were initially dissolved in chloroform; after evaporation, final solutions at 1.0×10^{-5} M concentration were achieved by adding THF. The steady-state UV-vis spectra of the compounds were recorded on a Shimadzu UV-1800 scanning spectrophotometer, while the fluorescence spectra were measured on a Perkin Elmer LS55 spectrophotometer. In fluorescence measurements conducted at 25 °C, a 1 cm quartz cell was used with the excitation and emission slit intervals set to 10.0 nm and 8.0 nm, respectively. Baseline corrected UV-vis spectra were collected from 200 to 1100 nm, and fluorescence spectra from 200 to 900 nm. The BODIPY dyes were excited at the wavelengths of maximum UV-vis absorption. Fluorescence quantum (Φ_F) yields were calculated using equation 1, with Rhodamine B (Φ_F=0.70 in ethanol) as the reference (23,24).

$$\Phi_F = \Phi_F(Std) \frac{F . A_{Std} . n^2}{F_{Std} . A . n_{Std}^2}$$
(1)

In the equation: Φ_F is the quantum efficiency of the sample; Φ_F (Std) is the reference's quantum yield; F and F_{Std} are the areas under the fluorescence emission curves for the sample and standard, respectively; A and A_{Std} are absorbance values at the excitation wavelength for the sample and standard; n and n_{Std} are the refractive indices of the solvents for the sample and standard.

2.4. DFT Calculations

Ground state geometric optimizations and excited state calculations were conducted using Density Functional Theory (DFT) and time-dependent DFT (TDDFT). These methods provided results that were consistent with experimental data reported in the literature (25–27). Computational calculations and visualizations regarding the compounds were executed utilizing Gaussian 09 Rev. C.01 and GaussView 5.0.9, respectively (28). The hybrid B3LYP functional with a mixed basis set was used to optimize molecular geometries. 6-311G was applied to **NafmetBDP**, and LANL2DZ to **NafmetZn** in the ground state at the gas phase. Frequency analysis confirmed optimised structures as true energy minima. TDDFT calculated the dyes' excited-state properties using the same functional and basis set as for the ground state. The keyword *IOp (9/40=4)* was employed to improve the precision of configuration coefficients in TDDFT calculations. Natural transition orbitals (NTOs) and hole-electron analysis of the final compounds were obtained from the transition density matrices and first excited-state energies,

respectively, using TDDFT calculations with Multiwfn (29).

3. RESULTS AND DISCUSSION

3.1. Synthesis and Characterization
The asymmetrical complexes (**NafmetBDP** and **NafmetZn**) were synthesized through a series of procedural steps, as depicted in Scheme 2.
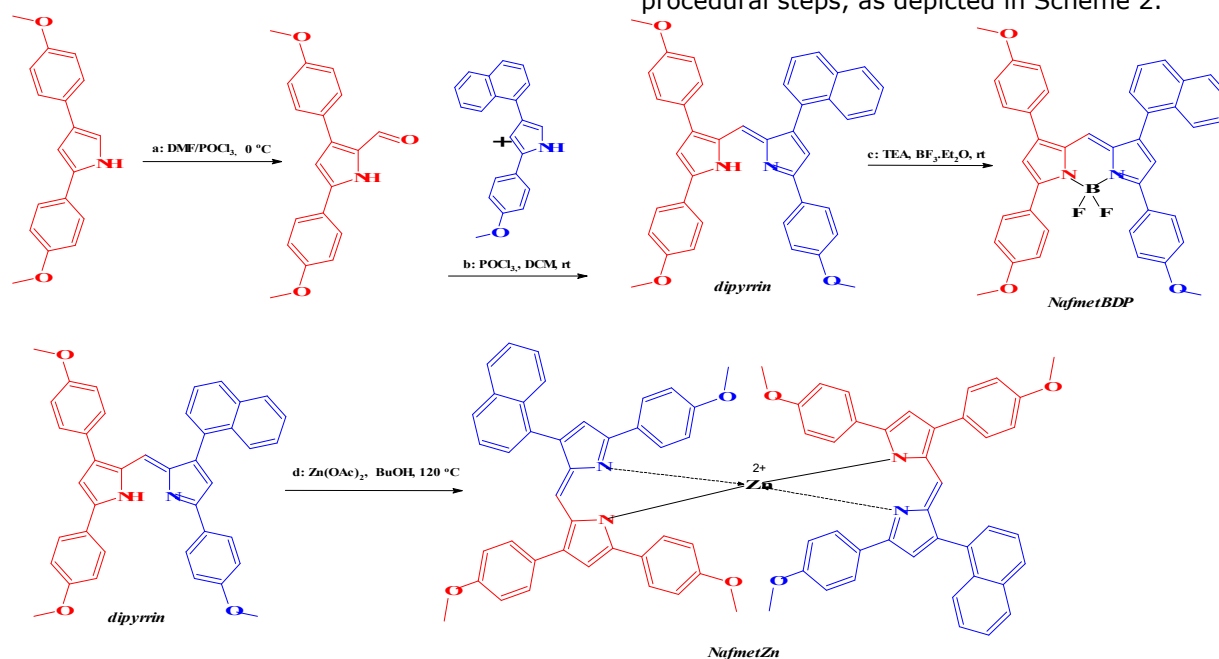
Scheme 2: The synthesis of the target molecules.

The individual preparation methodologies of these compounds are documented in literature and are conducted under mild conditions, yielding moderate synthesis efficiency (4). Initially, the precursor 2,4-bis(methoxyphenyl)-1*H*-pyrrole underwent formylation via the Vilsmeier-Haack reaction. Subsequently, the ultimate product was synthesized through acid-catalyzed condensation with a secondary pyrrole compound (2-methoxy-4-naphthyl-1*H*-pyrrole), resulting in the formation of an asymmetric dipyrromethene structure. Partitioned into two fractions, the initially isolated crude product facilitated the synthesis of BODIPY using $BF_3.OEt_2$, and a Zinc (II) complex was subsequently prepared to form a homoleptic complex utilizing Zinc (II) acetate salt. The BODIPY compound was subjected to purification via column chromatography, whereas the Zinc (II) complex underwent purification through cold precipitation in the butanol reaction solvent. The characterizations were conducted using $^1H/^{13}C$ NMR and HRMS analysis, confirming the data matched the expected structures. The ^1H-NMR measurements of the resulting compounds gave well-resolved spectra in the typical range of 0–9 ppm. The protons in aromatic groups gave singlet or distinct multiplets in the range of 6.67-8.25 ppm, depending on coupling. The pyrrole hydrogen atoms located at the -2 and -6 positions of the BODIPY core in **NafmetBDP** were identified as two separate singlet peaks at 6.67 ppm and 6.89 ppm, respectively. In contrast, the hydrogen atom at the *meso* (8) position exhibited a singlet peak at 7.17 ppm. This observation aligns with the inherent asymmetrical attributes of the structure. Furthermore, the methoxy (-OCH3) hydrogens are situated in the -α (-3, -5) and -β (-1,

-7) positions in the BODIPY core exhibit two distinct chemical shifts. Even though the structure contains three methoxy groups, the ones located at the -α position gave a singlet peak at 3.90 ppm corresponding to six hydrogen atoms (Fig. 1a). The hydrogens belonging to the methoxy groups in the alpha position of the structure were observed as a singlet peak at 3.81 ppm (Fig. 1a). This shows that the methoxy hydrogens at distant core positions have limited influence on the chemical environment, despite the structure's asymmetry. This indicates that the distant methoxy hydrogens in the asymmetric structure minimally affect the chemical environment. In the **NafmetZn**, the aforementioned methoxy peaks were detected as three singlets at 3.82, 3.71, and 3.52 ppm, as expected (Fig. 1b). The methoxy protons located adjacent to the Zn coordination center (-α positions) displayed broadened peaks, a phenomenon attributed to the Zn central atom's fully occupied d^{10} electronic configuration. In contrast, the protons positioned at the -β positions of the structure were characterized by distinct sharp singlets (Fig. 1b). In the **NafmetZn**, it was ascertained that the observed spectral peaks, primarily comprising multiplets, were in agreement with the hydrogen numbers. The differentiation of methoxy carbons, which are highly specific within these compounds, was evident in the ^{13}C NMR spectra and mirrored in ^1H NMR. The differentiation of methoxy carbons was apparent in the **NafmetZn** complex, identified at 55.3, 55.2, and 55.1 ppm (Fig. 1d), whereas in the BODIPY analog, the corresponding carbons exhibited overlapping signals (Fig. 1c). The carbon numbers in the compounds match the natural asymmetric structures of the compounds.
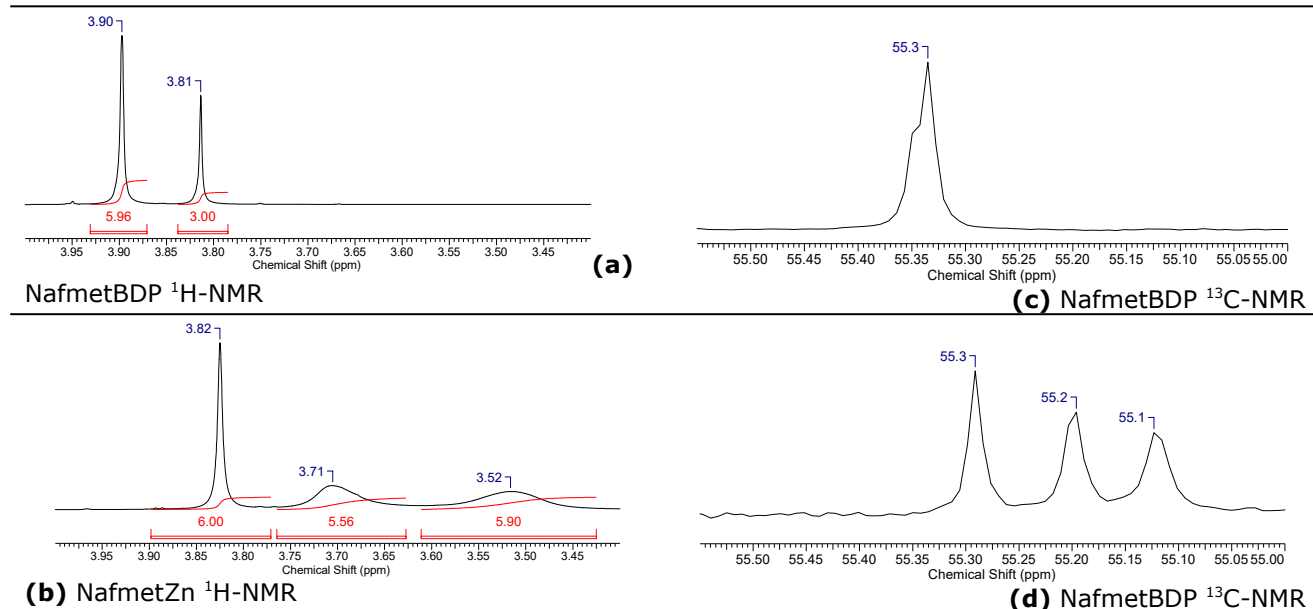
Figure 1: The scale of chemical shifts for NafmetBDP and NafmetZn for methoxy group peaks in ^{1}H-NMR (left) and ^{13}C-NMR (right).

Employing the ESI-TOF methodology, high-resolution mass spectra (HRMS) were acquired, and theoretical molecular masses were computed with consideration of isotopic contributions. The respective peaks were identified as the molecular ion peaks [M]$^-$ for **NafmetBDP** and [M+H]$^+$ for **NafmetZn**. The deviations in mass accuracy, expressed in parts per million (ppm, Δ), were ascertained to be 1.79 and 2.81 for the mentioned compounds, respectively.

The HRMS/TOF data substantiated that the experimentally observed structures corresponded with their theoretical values.

3.2. Photophysical Properties

The absorption and fluorescence spectra of the compounds in THF at room temperature were obtained. The related spectra of the dyes are shown in Figure 2a-b, with photophysical data in Table 1.
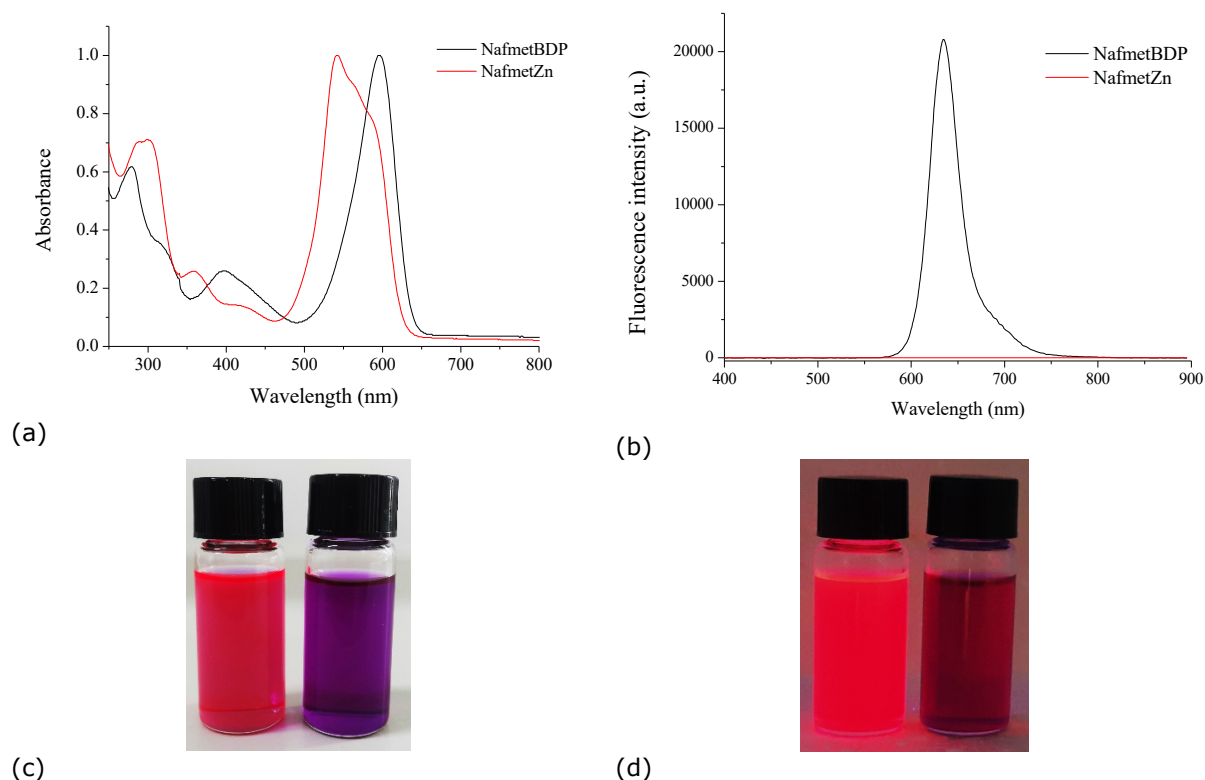
Figure 2: (a) Normalised absorption and (b) fluorescence spectra of the dyes **NafmetBDP** (λ_{exc}: 597 nm, slit 10.0 nm; λ_{ems}: 635 nm, slit 8.0 nm) and **NafmetZn** (λ_{exc}: 542 nm, slit 10.0 nm; ems slit 8.0 nm) in 1×10^{-6} M THF (c) The samples of **NafmetBDP** and **NafmetZn** solutions in THF under ambient light and (d) under UV illumination (λ_{exc}:365 nm). From left to right, **NafmetBDP** and **NafmetZn**.

The absorption spectrum of **NafmetBDP**, characterized as a BODIPY dye, exhibited a prominent absorption band at 597 nm, corresponding to the S_0-S_1 (π-π*) transition. Broader and less intense absorption bands within the 250-500 nm range, ascribed to the presence of substituted naphthyl and methoxy phenyl groups, correspond to transitions to higher energy states of S_0-S_2 and S_0-S_3. The shoulder attributed to the 0−1 vibrational transition associated with the main transition (S_0-S_1) in the high-energy region of the primary absorption band, typically observed in classical alkyl-substituted BODIPY compounds (4,30), was absent in this material. The full width at half maximum (FWHM) of the absorption band, covering the range of 500-650 nm, has substantially increased due to the presence of conjugated aryl substituents. The BODIPY fluorescence spectra display a single band from 580 nm to 730 nm when excited at the wavelength of maximum absorption, notably mirroring the absorption spectra. Upon excitation, the compound exhibits a pronounced emission at 635 nm, accompanied by a Stokes shift of 38 nm. The Stokes shift of the Boron complex (**NafmetBDP**) is greater compared to classical alkyl-substituted BODIPYs (4,30)—the emission peak exhibits broadening similar to that of the absorption peak. The **NafmetZn** complex gives a main absorption at 542

nm along with a shoulder at 586 nm. The absorption intensities at higher energy levels, specifically within the 250-350 nm range, showed an enhancement, which is concomitant with the augmentation in the number of aromatic substituents. The spectral bandwidth expanded from 61 nm to 81 nm, while the absorption coefficient elevated from 75400 to 89260 when compared to **NafmetBDP**. The molar absorption coefficients of the complexes are sufficiently high at the maximum of the $S_0{\rightarrow}S_1$ electronic transition band, rendering them comparable to structurally analogous BODIPYs. The Zinc (II) complex does not exhibit fluorescence regardless of the excitation wavelength. The observed fluorescence quenching may be attributed to the presence of aryl substituents at the -α and -β positions. The free rotation of the substituents enhances the probability of nonradiative transitions, thereby resulting in considerable fluorescence quenching of the complexes (22). According to literature on dipyrromethene-zinc complexes, the shoulder observed in the main absorption band is attributed to charge transfer transitions (31−33). The lower absorption band identified within the main absorption band in the experimental UV-Vis spectrum of **NafmetZn** may appear to correspond to the charge transfer transitions between reciprocal ligands.

Table 1: Experimental and theoretical photophysical parameters of the compounds.

Com-pound	ε_{abs} (max/ nm)	ε_{ems} (max/ nm)	εM^{-1} cm^{-1})	FWHM Abs / ems (nm)	Stoke s shift (nm)	$^a\Phi_F$	Electronic transition	Vertical excitation energy eV/nm	Oscillator Strength f	Major Contribution
	Experimental						*DFT calculation*			
Nafm etBD	597	635	75400	61 / 37	38	0.61	$S_0{\rightarrow}S_1$	2.17 / 571	0.91	H → L (99%)
							$S_0{\rightarrow}S_2$	2.53 / 490	0.05	H−1 → L (98%)
							$S_0{\rightarrow}S_3$	2.65 / 468	0.32	H-2 → L (98%)
NafmetZn	542	-	89260	87 / -	-	<0.0 01	$S_0{\rightarrow}S_1$	1.92 / 647	<0.01	H-1 → L (48%), H-1 → L+1 (36%), H → L (8%), H → L+1 (8%)
							$S_0{\rightarrow}S_2$	2.27 / 546	0.71	H-1 → L+1 (44%), H → L (42%), H → L+1 (10%)
							$S_0{\rightarrow}S_3$	2.29 / 540	0.76	H−1 → L (41%), H → L+1 (40%), H -1→ L+1 (12%)
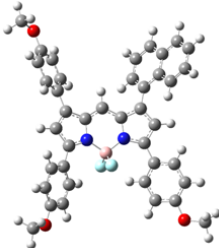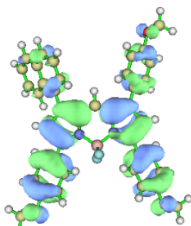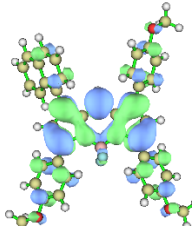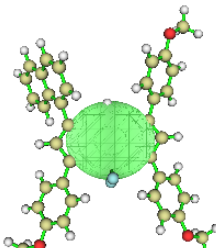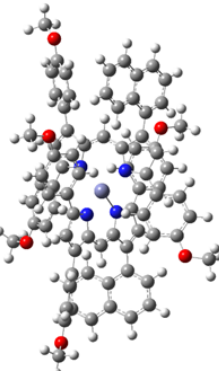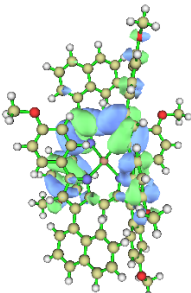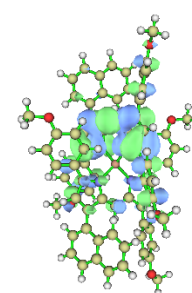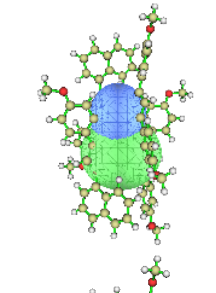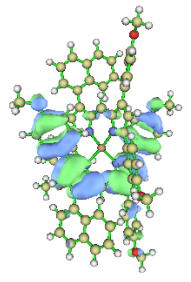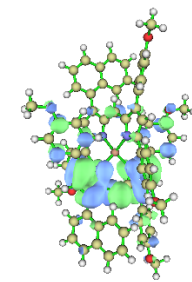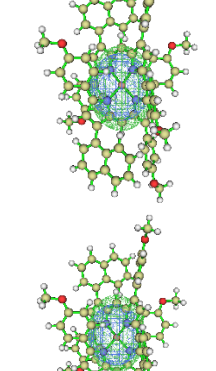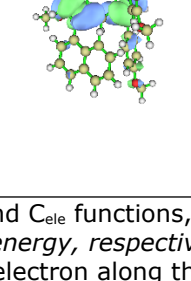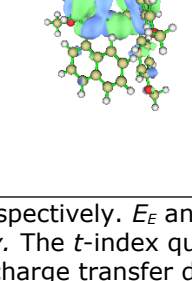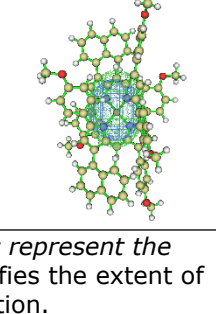
a: Rhodamine B in ethanol (Φ_F =0.70) was used as the fluorescence standard for fluorescence quantum yield calculations, and correction for the solvent refractive index (η) was applied [THF: η = 1.4072, EtOH: 1.3614].

The proximal arrangement of aryl groups at the -α and -β positions of the dipyrrin core resulted substantial bathochromic shift of the main absorption band. Beyond the π - π* transitions stemming from the naphthyl group, the n - π* transitions in methoxyphenyl subunits enhance the shifting. The substituent at the meso (8) position induces steric hindrance in the BODIPY core, thereby impeding the conjugation of distal aryl groups. Its absence results in the shift of BODIPY absorbance from the typical range of 500-550 nm to approximately 600 nm.

The Density Functional Theory (DFT) method has been extensively employed to elucidate the photophysical characteristics of BODIPY dyes, as it gives consistent results with the experimental findings (26,27,34). Therefore, to explain the photophysical properties of the compounds analyzed, we conducted calculations utilizing DFT/TD-DFT methods. The theoretical data that include dipole moments (μ), the electronic excitation energies (E_v), corresponding oscillator strengths (f), and the main configurations are summarized in Table 1. The optimized structures, natural transition orbitals (NTOs), and centroids of hole/electron (C_{hole} & C_{ele}) are demonstrated in Table 2.

Table 2: Optimized structures**,** Natural transition orbitals (NTOs) for the lowest-energy transitions (S_0-S_1) of the compounds (isosurface value = 0.02 au), centroids of hole and electron (C_{hole} & C_{ele}, isosurface value = 0.0003 au).

| Comp. | Transition | Optimized structure | NTOs | | C_{hole} & C_{ele} |
			Electron	Hole	
NafmetBDP	Dipole moment (μ): 5.99 Debye S_0-S_1 E_E : 2.17 eV t (Å): -1.683 E_C: 3.66 eV				
NafmetZn	Dipole moment (μ): 1.42 Debye S_0-S_1: E_E :1.92 eV t (Å): 1.049 E_C: 2.87 eV				
	S_0-S_2 E_E : 2.27 eV t (Å): -2.586 E_C: 3.09 eV				
	S_0-S_3 E_E :2.29 eV t (Å): -2.502 E_C: 2.87 eV				

Blue and green isosurfaces represent C_{hole} and C_{ele} functions, respectively. E_E and *Ec represent the excitation energy and the Coulomb attractive energy, respectively.* The *t*-index quantifies the extent of separation between the hole and electron along the charge transfer direction.

Geometry optimizations revealed that the Borondipyrromethene core in **NafmetBDP** assumes a planar geometric configuration, while the complexes exhibit a pseudo-tetrahedral geometry. The angles formed between the F-B-F atoms and the N-B-N atoms are calculated to be 109.3° and 109.4°, respectively. The dihedral angles between the BODIPY moiety and the naphthyl and methoxyphenyl groups at the distal (1,7) positions were determined to be 52.8º and 39.94º, respectively. The dihedral angles between the methoxyphenyl groups in the proximal (3,5) positions of the compound and the dipyrrin core were determined to be 36.5º. The influence of steric hindrance exerted by the naphthyl group results in a reduction of the angle at the distal positions. Consequently, this enhances the π-π interactions between the aromatic structures situated at the proximal positions and the planar core framework. Consequently, it can be inferred that the proximal positions exert a more pronounced bathochromic effect on the photophysical characteristics of the compound. In the Zn (II) complex, the dihedral angles of the naphthyl-dipyrrine entities increased from 52.8° to 68.2°, whereas the angles involving the methoxyphenyl substituents exhibited minimal alteration. The most significant modification was observed at the proximal (3,5) positions, where the angle decreased from 36.5° to 19.9°. The formation of a stable homoleptic complex with the Zinc (II) ion between the two macrostructures was facilitated by adjusting the angles to achieve values approaching linearity.

Also, the complexes have polar character, and the dipole moments were 5.99 and 1.42 Debye for the **NafmetBDP** and **NafmetZn**, respectively. The molecular dipole moments were oriented at approximately 45° from the dipyrrin core towards the exterior of the molecules. The tetrahedral configuration of the two identical ligands in the **NafmetZn** resulted in a reduction of the dipole moment, which aligns with theoretical predictions.

The main transition in BODIPY (**NafmetBDP**) occurs between HOMO→LUMO (99% contribution) due to electronic excitations from the S_0-S_1 energy levels (Table 1), while in the **NafmetZn**, absorption processes also involve the HOMO-1 and LUMO+1 orbitals. The calculated energy band gaps ($\Delta E = |E_{HOMO} - E_{LUMO}|$) for the compounds were found to be 2.17 eV and 2.27 eV, respectively, aligning well with experimental data. It should be noted that the main transition calculated for the Zinc (II) complex exhibits a low oscillator strength (<0.01) and does not constitute a band maximum. The main transition corresponds to the S_0-S_2 transition (f: 0.71) as indicated in Table 1. The singlet excitation energies (E_E) calculated by the TDDFT method for absorption spectra (λ_{cal}) validated the experimental values (λ_{exp}), with $\lambda_{exp}/\lambda_{cal}$ ratios of 1.05 and 0.99 for **NafmetBDP** and **NafmetZn**, respectively (Figure S1.).

Natural transition orbitals (NTOs) were calculated to visualize electronic transitions, representing excited electron-hole pairs from transition density matrices via TDDFT. Table 2 lists the NTOs and centroids of hole/electron isosurfaces for the singlet transitions of the dyes. The detailed isosurfaces of all singlet transitions belonging to **NafmetBDP** are given in supplementary material. Within the NTO isosurfaces, the main distribution regions for the electron and hole are denoted by green and blue, respectively. The calculations indicate that the distribution of excited electrons and holes across the molecule constitutes the main S_0-S_1 transition. The transition occurs without the involvement of charge transfer (CT), and is predominantly localized on the BODIPY core (Table 2, C_{hole} & C_{ele}, isosurface). However, it was determined that during high-energy transitions (S_0-S_2, S_0-S_3), a net charge separation (t>0) occurred from the BODIPY core to distal positions. The electrons for the transitions were exclusively localized on the dipyrrin skeleton, while the holes

were partially spread on the substituents at the -1, -3, -5, -7, and -8 (*meso*) positions. The centroids of the hole and electron, denoted as C_{hole}/C_{ele}, facilitated the smoothness of the electron/hole distribution behavior as outlined in Table 2. There is a significant overlap between the electron and hole pairs for the S_0-S_1 transition in **NafmetBDP**.

Notably, in the low-energy S_0-S_1 transition (E_E: 1.92 eV) of the **NafmetZn**, the two ligands exhibit charge separation manifesting as electrons and holes. In this context, Zinc (II) functions as a connecting entity between the opposing ligands, facilitating a charge transfer process. In the main transitions of this complex (characterized by elevated Oscillator Strength values of f: 0.71 and 0.76, respectively), S_0-S_2 and S_0-S_3, the negative t index indicates the absence of charge separation, demonstrating that the pertinent transitions are not charge transfers. Instead, these are locally excited electronic transitions originating from dipyrrin groups. The both complexes exhibited higher Coulomb attractive energies (E_c, exciton binding energies), reducing exciton dissociation compared to transition energies (E_E).

3.3. Thermal Properties

A significant attribute of the dyes applicable to technical fields is the range of temperatures at which these compounds maintain thermal stability and exhibit no alterations in their spectral properties. Therefore, the thermal properties of the compounds were determined in an inert N_2 atmosphere utilizing thermogravimetric analysis (TGA). The thermal stability of the compounds has been characterized through a variety of quantifiable metrics. Figure 3 presents the thermal degradation graphs of the compounds, while Table 3 provides the associated thermogram parameters.

Table 3: The decomposition temperatures and thermal stability of the compounds.

Compound	T_{max} (°C)*	Mass loss (%)	Decomposition rate (%/min)	**T10% (°C)	T30% (°C)	T50% (°C)
NafmetBDP	200	17	2.11	164	286	426
	360	41	2.96			
	590	70	2.37			
	760	97	1.42			
NafmetZn	447	10	0.97	440	665	890
	878	48	1.27			
	947	57	1.86			
	994	67	2.39			

*Maximum decomposition temperatures based on DTG plot. ** T10% (the temperature at which 10% of the initial mass is lost), etc.
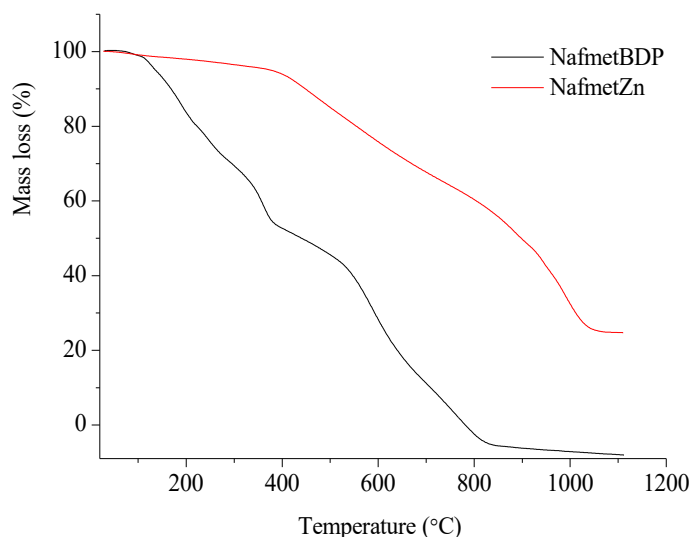
Figure 3: TGA thermogram of the compounds at a temperature ramp of 10 °C/min under N_2.

The thermal degradation of compounds, similar to that of other dipyrromethene dyes, occurs as a result of intramolecular oxidation-reduction reactions (35). The thermal destruction processes of the **NafmetBDP** and **NafmetZn** occurred in four stages, as evidenced by the TG curves displaying phases of sample weight loss. **NafmetBDP** underwent primary decomposition at 200 °C in an inert N_2 atmosphere, while the Zinc (II) complex (**NafmetZn**) began to decompose at a higher temperature of 447 °C. The most rapid degradation of the BODIPY derivative was observed in the second phase at 360 °C. Hence, it can be inferred that the thermal stability of the metal complex is considerably elevated despite the presence of identical organic substituents. Between 200-900 °C, the degradation phases showed reduced rates and mass loss, likely due to the breaking of covalent bonds and the carbonization of organic groups in the dipyrromethene framework. It should be noted that even at 994 °C, representing the final stage of decomposition, 33% of the structure of the Zn (II) complex persisted. The decomposition rates (%/min) of the BODIPY derivative are considerably greater, almost by two orders of magnitude, in comparison to those of the Zinc (II) complex. Utilizing T10% temperatures as a comparison basis, it is observed that **NafmetBDP** decomposes at 164 °C and **NafmetZn** at 440 °C, indicating that **NafmetZn** exhibits nearly threefold greater thermal stability. The carbonization efficiencies at 700 °C, generally regarded as a reference point, are 89% for **NafmetBDP** and 33% for **NafmetZn**, respectively. The coordination of homoleptic metal with an identical ligand resulted in an enhancement of the thermal stability of the dipyrromethene core when compared to its coordination with Borondifluoride (BF_2). The comparatively reduced thermal stability of BODIPY relative to Zinc (II) dipyrromethene might be attributed to the involvement of fluorine atoms in intramolecular redox processes. The residue observed at elevated temperatures in the thermogram of the compound **NafmetZn** may be due to lower oxidation potential of Zinc atoms in contrast to the substantially higher oxidation potential of fluorine atoms and the strong covalent nature of B–F bonds (36,37). Consequently, the formation of ZnO and carbonized products may occur, given that the analysis was conducted under a nitrogen atmosphere. The incorporation of aryl groups into pyrrole moieties has been found to significantly influence the thermal stability of Zinc (II) dipyrromethenates when compared to their alkyl-substituted counterparts as reported in the literature (35).

4. CONCLUSION

In summary, novel homoleptic BODIPY and [Zn(dipyrrin)₂] complexes were synthesized from an asymmetric dipyrromethene ligand, with structures confirmed by NMR and HRMS. Their photophysical properties in solution were examined using UV-visible absorption and fluorescence spectroscopy. The absorption band's FWHM from 500-650 nm significantly increased due to conjugated aryl substituents. While the BODIPY fluorescence spectra display a single band from 580 to 730 nm, similar to the absorption spectra at the maximum absorption wavelength, the Zinc (II) complex does not fluoresce at any excitation wavelength. Aryl groups positioned at the -α and -β sites of the dipyrrin core cause a significant bathochromic shift in the main absorption band. The shift is further enhanced by n - π* transitions in methoxyphenyl subunits and π - π* transitions from the naphthyl group, extending BODIPY absorbance from the typical range of 500-

550 nm to ca. 600 nm. Density Functional Theory (DFT) calculations and electron-hole analysis reveal that the complexes have a pseudo-tetrahedral geometry and polar character. The calculations show that the main S_0-S_1 transition involves the distribution of excited electrons and holes across the molecule, and it is mainly localized on the BODIPY core without charge transfer in **NafmetBDP**. During high-energy transitions, charge separation occurs from the dipyrrin core to distant positions, with electrons localized on the dipyrrin skeleton and holes spread on the substituents at the -1, -3, -5, -7, and -8 positions. In **NafmetZn** complex, charge-transfer transitions between reciprocal ligands cause the main absorption band's redshift, as shown by electron-hole analysis. The proximal positions significantly enhance the bathochromic effect on the compounds' photophysical properties. According to TGA, the coordination of Zinc (II) resulted in considerable thermal stability and enhanced degradation temperatures. **NafmetZn** demonstrates a thermal stability that is nearly three times greater than BODIPY analogue. Aryl groups in pyrrole moieties significantly enhanced the thermal stability of Zinc (II) dipyromethenates compared to their alkyl counterparts. This work shows that chromophoric dipyrromethene complexes hold promise for developing photostable and thermostable materials capable of energy transfer in the visible spectra.

5. CONFLICT OF INTEREST

The author declares no competing interests.

6. ACKNOWLEDGMENTS

7. REFERENCES

1. Wood TE, Thompson A. Advances in the chemistry of dipyrrins and their complexes. Chem Rev [Internet]. 2007 May 1;107(5):1831–61. Available from: <URL>.

2. Baudron SA. Dipyrrin based metal complexes: reactivity and catalysis. Dalt Trans [Internet]. 2020 May 19;49(19):6161–75. Available from: <URL>.

3. Shikha Singh R, Prasad Paitandi R, Kumar Gupta R, Shankar Pandey D. Recent developments in metal dipyrrin complexes: Design, synthesis, and applications. Coord Chem Rev [Internet]. 2020 Jul 1;414:213269. Available from: <URL>.

4. Loudet A, Burgess K. BODIPY dyes and their derivatives: Syntheses and spectroscopic properties. Chem Rev [Internet]. 2007 Nov 1;107(11):4891–932. Available from: <URL>.

5. Lu H, Shen Z. BODIPYs and their derivatives: The past, present and future. Front Chem [Internet]. 2020 Apr 28;8:541725. Available from: <URL>.

6. Tahoun M, Gee CT, McCoy VE, Sander PM, Müller CE. Chemistry of porphyrins in fossil plants and animals. RSC Adv [Internet]. 2021 Feb 17;11(13):7552–63. Available from: <URL>.

7. M. Ravikanth M, Vellanki L, Sharma R. Functionalized boron-dipyrromethenes and their applications. Reports Org Chem [Internet]. 2016 Jan;6:1–24. Available from: <URL>.

8. Yilmaz RF, Derin Y, Misir BA, Atalay VE, Tutar ÖF, Ökten S, et al. Synthesis and spectral properties of symmetrically arylated BODIPY dyes: Experimental and computational approach. J Mol Struct [Internet]. 2023 Nov 5;1291:135962. Available from: <URL>.

9. Wang L, Ding H, Ran X, Tang H, Cao D. Recent progress on reaction-based BODIPY probes for anion detection. Dye Pigment [Internet]. 2020 Jan 1;172:107857. Available from: <URL>.

10. Bumagina NA, Antina E V. Review of advances in development of fluorescent BODIPY probes (chemosensors and chemodosimeters) for cation recognition. Coord Chem Rev [Internet]. 2024 Apr 15;505:215688. Available from: <URL>.

11. Nuri Kursunlu A, Guler E. The sensitivity and selectivity properties of a fluorescence sensor based on quinoline-Bodipy. J Lumin [Internet]. 2014 Jan 1;145:608–14. Available from: <URL>.

12. Boens N, Leen V, Dehaen W. Fluorescent indicators based on BODIPY. Chem Soc Rev [Internet]. 2012 Jan 17;41(3):1130–72. Available from: <URL>.

13. Yang J, Jiang H, Desbois N, Zhu G, Gros CP, Fang Y, et al. Synthesis, spectroscopic characterization, one and two-photon absorption properties, and electrochemistry of truxene π-expanded BODIPYs dyes. Dye Pigment [Internet]. 2020 May 1;176:108183. Available from: <URL>.

14. Song G, Li Z, Han Y, Jia J, Zhou W, Zhang X, et al. Enhancement of two-photon absorption in boron-dipyrromethene (BODIPY) Derivatives. Molecules [Internet]. 2022 Apr 29;27(9):2849. Available from: <URL>.

15. Klfout H, Stewart A, Elkhalifa M, He H. BODIPYs for dye-sensitized solar cells. ACS Appl Mater Interfaces [Internet]. 2017 Nov 22;9(46):39873–89. Available from: <URL>.

16. Singh SP, Gayathri T. Evolution of BODIPY dyes as potential sensitizers for dye-sensitized solar cells. European J Org Chem [Internet]. 2014 Aug 16;2014(22):4689–707. Available from: <URL>.

17. Kaur P, Singh K. Recent advances in the application of BODIPY in bioimaging and chemosensing. J Mater Chem C [Internet]. 2019 Sep 26;7(37):11361–405. Available from: <URL>.

18. Kolemen S, Akkaya EU. Reaction-based BODIPY probes for selective bio-imaging. Coord Chem Rev [Internet]. 2018 Jan 1;354:121–34. Available from: <URL>.

19. Ono M, Watanabe H, Kimura H, Saji H. BODIPY-based molecular probe for imaging of cerebral β-amyloid plaques. ACS Chem Neurosci [Internet]. 2012 Apr 18;3(4):319–24. Available from: <URL>.

20. Lee JS, Kang N young, Kim YK, Samanta A, Feng S, Kim HK, et al. Synthesis of a BODIPY library and its application to the development of live cell glucagon imaging probe. J Am Chem Soc [Internet]. 2009 Jul 29;131(29):10077–82. Available from: <URL>.

21. Gawley RE, Mao H, Haque MM, Thorne JB, Pharr JS. Visible fluorescence chemosensor for saxitoxin. J Org Chem [Internet]. 2007 Mar 1;72(6):2187–91. Available from: <URL>.

22. Sevinç G, Küçüköz B, Elmalı A, Hayvalı M. The synthesis of −1, −3, −5, −7, −8 aryl substituted boron-dipyrromethene chromophores: Nonlinear optical and photophysical characterization. J Mol Struct [Internet]. 2020 Apr 15;1206:127691. Available from: <URL>.

23. Bittel AM, Davis AM, Wang L, Nederlof MA, Escobedo JO, Strongin RM, et al. Varied length stokes shift BODIPY-based fluorophores for multicolor microscopy. Sci Rep [Internet]. 2018 Mar 15;8(1):4590. Available from: <URL>.

24. Kubin RF, Fletcher AN. Fluorescence quantum yields of some rhodamine dyes. J Lumin [Internet]. 1982 Dec 1;27(4):455–62. Available from: <URL>.

25. Emirik M, Karaoğlu K, Serbest K, Çoruh U, Vazquez Lopez EM. Two novel unsymmetrical ferrocene based azines and their complexing abilities towards Cu(II): Spectroscopy, crystal structure, electrochemistry and DFT calculations. Polyhedron [Internet]. 2015 Mar 9;88:182–9. Available from: <URL>.

26. Laine M, Barbosa NA, Wieczorek R, Melnikov MY, Filarowski A. Calculations of BODIPY dyes in the ground and excited states using the M06-2X and PBE0 functionals. J Mol Model [Internet]. 2016 Nov 7;22(11):260. Available from: <URL>.

27. Matveeva MD, Zheleznova TY, Kostyuchenko AS, Miftyakhova AR, Zhilyaev DI, Voskressensky LG, et al. 1,7-isoxazolyl substituted BODIPY dyes – synthesis and photophysical properties. ChemistrySelect [Internet]. 2023 Feb 3;8(5):e202204465. Available from: <URL>.

28. Frisch R, Trucks GW, Schlegel HB, Scuseria GE, Robb MA, Cheeseman JR. Gaussian09, 1 121, gaussian. 2009;150–66.

29. Lu T, Chen F. Multiwfn: A multifunctional wavefunction analyzer. J Comput Chem [Internet]. 2012 Feb 15;33(5):580–92. Available from: <URL>.

30. Sevinç G, Küçüköz B, Yılmaz H, Şirikçi G, Yaglioglu HG, Hayvalı M, et al. Explanation of pH probe mechanism in borondipyrromethene-benzimidazole compound using ultrafast spectroscopy technique. Sensors Actuators B Chem [Internet]. 2014 Mar 31;193:737–44. Available from: <URL>.

31. Akhüseyin E, Türkmen O, Küçüköz B, Yılmaz H, Karatay A, Sevinç G, et al. Two photon absorption properties of four coordinated transition metal complexes of tetraarylazadipyrromethene compounds. Phys Chem Chem Phys [Internet]. 2016 Feb 3;18(6):4451–9. Available from: <URL>.

32. Teets TS, Partyka D V., Updegraff JB, Gray TG. Homoleptic, four-coordinate azadipyrromethene complexes of d10 zinc and mercury. Inorg Chem [Internet]. 2008 Apr 1;47(7):2338–46. Available from: <URL>.

33. Bumagina NA, Krasovskaya ZS, Ksenofontov AA, Antina E V., Berezin MB. Reactivity and zinc affinity of dipyrromethenes as colorimetric sensors: structural and solvation effects. J Mol Liq [Internet]. 2024 Apr 1;399:124397. Available from: <URL>.

34. Helal W, Marashdeh A, Alkhatib Q, Qashmar H, Gharaibeh M, Afaneh AT. Tuning the photophysical properties of BODIPY dyes used in DSSCs as predicted by double-hybrid TD-DFT: The role of the methyl substituents. Int J Quantum Chem [Internet]. 2022 Dec 15;122(24):e27000. Available from: <URL>.

35. Berezin MB, Dogadaeva SA, Antina E V., Lukanov MM, Ksenofontov AA, Semeikin AA. Design and physico-chemical properties of unsymmetrically substituted dipyrromethenes and their complexes with boron(III) and zinc(II). Dye Pigment [Internet]. 2022 Jun 1;202:110215. Available from: <URL>.

36. Bumagina NA, Kritskaya AY, Antina E V., Berezin MB, V'yugin AI. Effect of alkyl, aryl, and meso-aza substitution on the thermal stability of BODIPY. Russ J Inorg Chem [Internet]. 2018 Oct 16;63(10):1326–32. Available from: <URL>.

37. Sevinç G. Photophysical, thermal, and DFT studies on a tetraaryl-azadipyrromethene ligand and its zinc(II) complex. Turkish J Chem [Internet]. 2023 Dec 29;47(6):1438–51. Available from: <URL>.

DSSC Sensitizers: A Panoramic Comparison

Mussarat Jabeen[1] iD **, Iqra Mutaza[2]** iD **, Rabia Anwar[2]** iD

[1]Department of Chemistry, Govt. Sadiq College Women University, Bahawalpur 63100, Pakistan.
[2]Chemistry Department, UCP, Lahore 54000, Pakistan.

Abstract: Currently, energy and greenhouse gas emissions are the biggest problems. As a result of overpopulation and high energy consumption, non-renewable energy sources are continuously depleting. Greenhouse gases are also being emitted at a very high rate. The modern world must use renewable energy sources, among which solar energy is safe and available everywhere. Solar energy is efficiently transformed into electrical energy by photovoltaics (solar cells). During the past decades, DSSC the type of thin-film photovoltaics, gained importance due to cost-effectiveness, durability, ease of fabrication, and low toxicity. These cells convert sunlight into electricity with a power conversion efficiency of approximately 20%. Glass substrate, photo-anode, sensitizer, electrolyte and counter electrode are the key components of DSSCs. Among these, sensitizers are the most important part of these cells that absorb photons, generate electrons, create electron-hole-pair and produce electricity. In the beginning, only ruthenium metal complexes were used as dyes, but now a large number of organic, inorganic and natural compounds are widely used to enhance the overall performance of these cells. This is an in-depth review on solar cells but mainly focuses on the construction, operating principle, and performance of DSSCs. In this review, we not only presented a library of sensitizers used in DSSCs but also gives a brief comparison between these sensitizers to help future research.

1. INTRODUCTION

Energy plays a vital role in the country's economic development, but with an increase in population, modernization and decreasing energy resources, its demand is constantly rising (1,2) Today, countries development is negatively affected by energy shortage (3). Nearly 80% of the world's energy demand is met by fossil fuels such as oil, gas, and coal (4). Using these resources to produce energy generates massive CO_2 emissions, which mainly contribute to global warming and climatic disturbances (1).

Energy resources are classified into two classes: renewable and non-renewable (5). Among them, non-renewable sources of energy, like fossil fuels (coal, gas, natural gas, and petroleum) are economically more important and depleting rapidly but import a negative role on the environment, producing a large amount of harmful gases (6), such as carbon dioxide (CO_2), methane or natural gas

(CH_4), chlorofluorocarbons or CFCs (CCl_2F_2), nitrous oxide or laughing gas (N_2O), ozone (O_3) and peroxyacetyl nitrate (PAN) responsible for trapping heat radiated from earth's surface (7), ultimately raising the temperature of earth and causing photochemical smog (8). Around 60% of the world's population lives in Asia and faces environmental challenges due to the excessive use of fossil fuels. In China, Taiwan, Pakistan, India, Hong Kong, Macao, Nepal, Bangladesh, Indonesia, Malaysia and in other developing countries, carbon dioxide and other pollutants are causing serious ecological changes (9). In contrast, renewable energy sources include wind, solar, geothermal, and hydropower (10). Today, renewable energy is essential, clean, sustainable, fascinating and stabilizes modern energy demand (11).

2. SOLAR ENERGY

Earth receives solar radiations as light and energy. Due to its abundance and ease of availability, solar

energy can meet the global energy demand. As energy demand grows in developing countries, they are seeking reliable sources of energy (12). A large portion of Europe's solar resources are located in Spain. In 2016, Spain led the PV market with 2.6 GW of grid-connected installations. In response, the global PV market has grown by around 5600 MW (13). After Spain, Germany ranked second in the world for PV installations. Approximately a third of all PV power installed globally is in Germany (14). In terms of energy production, China ranks second behind the United States. The solar energy potential of China is enormous (15). In 2010, energy production was 0.15GW. By 2020, it is projected to increase to 4-8 GW and in 2030, it is expected to reach 16.9TG (16,17). Solar radiation is most prevalent in Asian countries as compared to others because of long sunshine duration (12).

2.1. Solar Cell

Solar cells or photovoltaics convert sunlight directly into electricity by using the photovoltaic effect (12). The photovoltaic effect was discovered in 1839 by Alexandre Edmond Becquerel. The first silicon photovoltaic cells were created by Russell Ohl in 1946. Increasing the efficiency of solar cells is a major goal in solar cell development (18). Photovoltaic technology is currently based on the creation of electron holes in multiple layers (p-type and n-type materials) of semiconductor materials. The p-type and n-type junctions are arranged so that when light of sufficient energy strikes them, an electron is ejected and moves from one layer to the next. Electrons and holes are created in the process, which generates electricity (19). Solar cells convert solar energy into electricity as a function of the proportion of incoming solar output to the maximum electrical power produced by the cell under concentrated loads. Because it is so effective and thought to be so relevant, this predictable metric is now widely used for judging the worth of products (20).

2.1.1. Types of solar cells
Based on manufacturing material, cost, efficiency, size and life cycle, solar cell technologies can be roughly categorized as:

a) 1st generation solar cells: Silicon wafer based solar cells are "first-generation solar cells" made from single silicon crystals (monocrystalline) or many silicon crystals (poly-crystalline) (21,22) with efficiencies of 26.7% and 22.3%, respectively (23). Due to their rigidity, these cannot bend easily but covers 86% of the market with a maximum efficiency of 40%.

b) 2nd Generation Solar Cells: Thin-film solar cells are "second generation solar cells", made of copper indium gallium selenide (CIGS) (24), cadmium telluride (CdTe), CZTs (25,26), Gallium Arsinide (GaAs) and amorphous silicon (a-Si) (27) having efficiencies of 23.4% (23,28), 21.0% (23), 37.4% (29) and 10.2-13.4% (23). Due to their flexibility, durability, stability, low cost, high optical absorbance, light weight, and portability, these are widely used in wearable electronic devices, agricultural infrastructure, space applications, and transportation but are extremely toxic because of the poisonous metals (30).

c) 3rd Generation Solar Cells: Unlike previous generations, third-generation solar cells are designed to improve efficiency, cost-effectiveness, and versatility while overcoming some limitations associated with previous generations. Third-generation solar cells encompass a number of different approaches, each with its own set of characteristics and potential applications. These includes, Nano crystal based SC (31), Polymer SC, Thermo-photovaltic (32), Dye sensitized SC (33), Graphene based SC (34), Quantum dots SC (35) and concentrated SC (22,36) with efficiencies of 5.14% (37), 18% (38), 40% (39), 11.1% (23) -15.4 (40), 14.1% (41), 12% (42), and 25% (43). These solar cells exhibit different efficiency with inexpensive material (44), and because of modernization and the increased demand for energy, researchers are always working to increase it.

3. DYE SENSITIZED SOLAR CELL

A DSSC is also known as Gratzel's cell, a thin-film solar cell that converts sunlight into electricity using a dye that can either be organic or inorganic (45). In 1991, Michael Grätzel and Brian O'Regan invented them. Due to their structure and materials, these are more suitable for certain applications than traditional silicon-based solar cells. Originally, DSSCs were a part of the second generation, but improvements in their design and materials contribute to their classification as third-generation solar cells (46). Due to their dramatic applications (47), like low cost (48), easy fabrication (49), flexibility (50), light weight, transparency (51), ease of manufacturing (52), efficiency (53), reuse of dyes and low toxicity, these are widely used nowadays (54).

Dye + Semiconductor + sunlight= Efficiency

3.1. Components of Dye Sensitized Solar Cell
Dye-Sensitized Solar Cells (DSSCs) comprise crucial elements, each playing a vital role in converting sunlight into electricity (55). The primary components include:

3.1.1. Glass-substrate
Glass substrate, the transparent and conducting surface on which the photo electrode is deposited (56). Mostly, FTO (Fluorine doped tin oxide) (57) and ITO (Indium tin oxide) (58) are used as conducting glass substrates. Conducting glass provides electrical conductivity necessary for shuttling electrons between anode and external circuit and allows sunlight to pass through photo-anode without significant absorption or reflection (59).

3.1.2. Photo-anode
Light absorption and electron generation in DSSC take on anode known as Photo-anode or photo-active electrode (60). Typically consists of nanocrystalline titanium dioxide (TiO_2) layered on a conductive glass substrate, with TiO_2 acting as the semiconductor. The nanocrystalline TiO_2 provides a large surface area for

sensitizer, allowing sufficient light absorption (61,62). Except titanium oxide, other materials like ZnO (63), SnO (64), NiO (65), and CuO (66). The main function of photo-anode is to absorb light and facilitate electron injection into the semiconductor (51).

3.1.3. Sensitizer

The most important component of DSSC is dye, also known as sensitizer or photosensitizer, that is responsible for the absorption of light, permute electrons to the excited states, and generating electron hole (67). This dye is usually naturally extracted from plants (68), inorganic metal ions (69), organic compounds (70) that are absorbed on titanium surface.

3.1.4. Electrolyte

Electrolyte in DSSC is a redox couple that shuttles electron between anode and cathode; it accepts electrons from phto-anode, regenerates sensitizer and completes the circuit, allowing the cell to convert sunlight into electrical energy continuously (33,71). Different electrolytes are used to increase the efficiency of cells, like I^-/I_3^- redox couple (71), Cu^+/Cu^{+2} (72), Co^{2+}/Co^{3+} (73), cobalt-polypyridine (74), Br^-/Br_3^- (62), LiI and N,N-methylpyrrolidinium dicyanamide (75).

3.1.5. Counter electrode

Counter electrode is a cathode, which is made from conducting material that collects and transfers electrons from external circuit (76) and also catalyzes the redox reaction of electrolyte or redox

couple (77). Different types of counter electrodes are now used to improve efficiency, like Pt (78), carbon (79), black carbon (80), graphene (81), transition metals (82), conducting polymers (83), carbides, nitrides and charcoginides (77).

3.2. Working of DSSC

The working of DSSC is continuous and cyclic, and the main steps include (84,85).

a. Dye adsorption: Nano-crystalline titanium oxide coated on conducting glass, on which dye is adsorbed.

b. Excitation of Sensitizer: Dye becomes electronically excited by absorbing photons from sunlight.

c. Electron-hole-pair creation: Electrons are injected into the semiconductor material by sensitizer, and electron-hole pairs are created.

d. Electron transportation: Electrons moved through the semiconductor material towards the external circuit and generated the electric current.

e. Redox reaction of electrolyte: By accepting electrons, the electrolyte is reduced, and electrons return to sensitizer for regeneration to its original state. As, electrolyte is redox couple, it oxidized to its original state by releasing electrons.

f. Generation of electric current: Through the external circuit, the released electrons are directed to the counter electrode, where they generate an electric current.
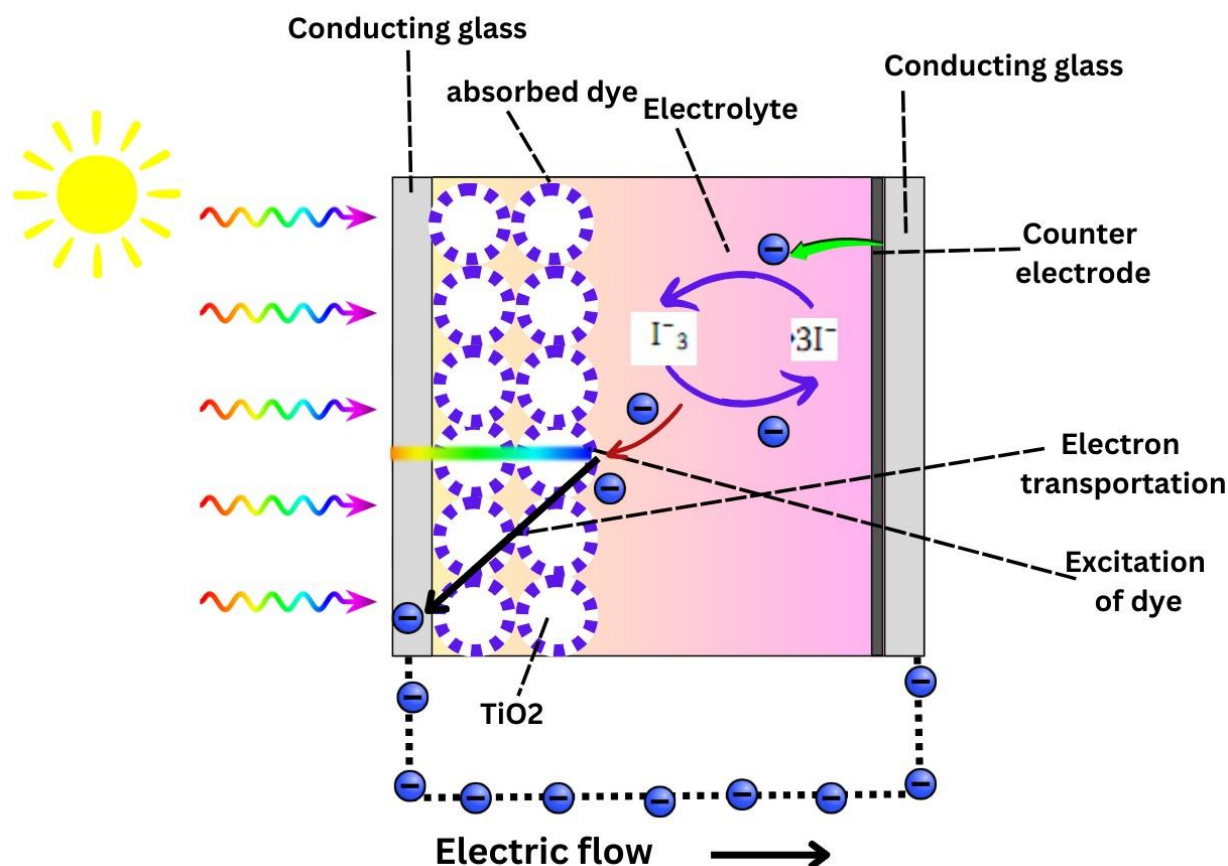

Figure 1: DSSC's working principle.

Jabeen M et al. JOTCSA. 2025; 12(1): 35-46

REVIEW ARTICLE

3.3. Efficiency of DSSC

Efficiency of DSSC was calculated by the given formula (68)

$$\eta = \frac{J_{ac} \times V_{oc} \times FF}{P_{in}} \times 100$$

J_{ac}= short circuit current; the largest current that may be drawn from solar cell (mA cm^{-2}); V_{oc}= open circuit voltage (mV), the maximum voltage available from solar cell; P_{in}= input power or power density of incident light, light power per unit area; FF= fill factor (It shows how effectively solar cells convert sunlight into electrical energy. The typical range is 0.5 to 0.85; represented in percentage, a high number denotes great efficiency (86) & can be calculated by the formula below (87).

$$FF = \frac{Pm}{(Jac \times Voc)}$$
Pm= maximum power output

3.4. Sensitizers/Dyes Used in DSSC's

Sensitizer is the most important part in DSSC, which absorbs photons and is responsible for injection of electrons (88). This sensitizer must have a) broad absorption spectra that cover the visible region and NIR b) anchoring groups that strongly bind with semiconductor layers like –COOH, –CN, –NH$_2$, –PO$_3$H$_2$, (89,90) c) cost-effectiveness (91,92), d) chemically compatible with all components like electrolyte and semiconductor material (93), e) stable (94), and f) non-toxic (95). A large number of sensitizers can be used in DSSC, and researchers are trying to synthesize dyes with maximum efficiency (96). Normally these dyes are categorized as:

Natural photosensitizers
Synthetic photosynthesizes

3.4.1. Natural sensitizers

Natural dyes offer a great potential for reducing the environmental impact of solar cell production and increasing sustainability due to their abundant affordability and eco-friendly nature. These dyes can be extracted from insects, plants, flowers, etc., and offer a wide range of colors like green, purple, blue, red, orange and many more. These natural dyes absorbing a broad range of light wavelengths makes them a viable option for improving the efficiency and performance of solar cells. many compounds like (97). In contrast to artificial dyes, natural dyes are readily available, less expensive, simple to make, non-toxic, eco-friendly, and completely biodegradable (95). Usually, they belong to the anthocyanin family, which can be found in red, blue, orange, purple, violet, and intermediate shades (95). As well as the purple-red color of autumn leaves, the red color of budding and young shoots is also due to anthocyanin (98). Anthocyanin is frequently used as sensitizer due to widespread availability, solubility in water, eco-friendliness and cost-effectiveness but mostly absorb visible light (95). Except for anthocyanin, chlorophyll, and carotenoids, extracted from plant leaves can also be used as dye sensitizers (68). However, chlorophyll alone is not favorable for DSSC and gives low efficiency due to the steric hindrance of its long chains (52). These natural photosensitizers showed different efficiencies summarized in Supplementary Table S1. Here, a total of 145 natural sensitizers with their efficiencies were summed up to show the importance of these natural sensitizers. These sensitizers are easy to extract but difficult to store, as they easily decompose with temperature change or light interaction.

3.4.2. Synthetic sensitizers

Today, a variety of synthetic sensitizers are used, including organic and inorganic compounds.

I. Organic sensitizers: Furthermore, organic dyes are now a practical alternative to inorganic dyes, which are perceived to be hazardous, costly, and difficult to synthesize (99). Researchers are investigating a wide range of organic compounds because of their benefits, which include low cost, ease of synthesis, environmental friendliness, stability, co-sensitization, a broad absorption spectrum, and redox mediators that enhance injection as well as electron transport (70). These compounds include carboxylic acids (100), indoles (101), hydrazones (102), pyridines (103), phorphyrins (104), Schiff bases (105), and aromatics that are currently used as sensitizers in DSSCs (70,106). The first usage of organic compounds as DSSC dyes occurred in the 2000s. Initially, DSSCs use eight organic dyes—methyl orange, crystal violet, fast green, aniline blue, alcian blue, methyl orange, and carbolfuchsian—as dye sensitizers. Eosin Y was expected to be the best among all of them, with the maximum efficiency of 0.399 (Voc = 0.671, Jsc = 1.02, and FF = 58.1) (107). Due to pi-conjugation, donor electrons and heteroatoms, these metal-free organic sensitizers exhibited high efficiency (52).

As a result of ongoing research, a wide variety of organic compounds are currently employed as DSSC sensitizers. To aid in comprehension, the material is summarized in Supplementary Table S2. During the past 15 years, organic sensitizers gained importance due to high yield, easy storage and reuse sensitizers.

II. Inorganic Sensitizers: In DSSCs, metal complexes, particularly transition metal complexes, show better photovoltaic performance and higher stability than organic and natural dyes due to their unique optical and electrical properties (108). Once photons are absorbed, they effectively transfer electrons into the semiconductor material, which is usually titanium dioxide, to initiate the production of an electric current. The long-term performance of DSSCs depends on the greater stability and lifespan provided by certain metal-based dyes. In DSSC, ruthenium-based complexes are most extensively used; for over 30 years, they exhibited high efficiency of up to 80% due to their versatility, high absorption, and ability to form stronger bonds with donor nitrogen of ligands (52) but are costly, toxic, and decompose with the passage of time (109).

Copper complexes not only act as sensitizers but also work as redox mediators (110). Except these, nickel (111), iron (112), zinc (113), osmium and many other transition metal complexes are also used as sensitizers. Some metal-based sensitizers are summarized in Supplementary Table S3.

It is expected that the DSSC innovation will be used to fulfill many prospective power requirements like economic growth, energy sustainability, and the conservation of the environment. Furthermore, DSSC is one of the most prominent renewable technologies that help reduce environmental problems. Globally, researchers are focusing on improving dye-sensitized solar cells' efficiency. To improve DSSC performance, a variety of strategies are being explored, and dye material is one of them. As DSSC's performance is directly affected by sensitizers as they are the most prevalent component. Sensitizers mentioned above are some of the reported metal-free, natural, and metal-based sensitizers. Scientists are constantly working to synthesize/modify the reported sensitizers to enhance their efficiency, flexibility, and environmental compatibility.

4. DETAILED COMPARISON (DISCUSSION) OF PHOTOSENSITIZERS USED IN DSSC

To gain a deeper insight into DSSCs, it is essential to explore the various types of photosensitizers, the heart of DSSC. These sensitizers are key to the efficiency, stability, and overall performance of DSSCs, as they facilitate light absorption and electron transfer to the semiconductor. In this section, we will present a comprehensive comparison of the main categories of photosensitizers—natural dyes, organic (metal-free) dyes, and metal-based dyes—based on literature. By exploring their mechanisms, efficiencies, absorption spectra, as well as their advantages and challenges, we aim to provide a detailed understanding of each type. This comparison will not only shed light on the potential of these photosensitizers but also highlight how ongoing innovations could shape the future of DSSCs, positioning them as a leading technology in the pursuit of sustainable energy solutions.

I.   Natural photosensitizers
As these are plant-based dyes extracted from plants like chlorophyll, anthocyaninand, carotenoid, as well as natural materials like animal-based ones like blood, meat or coal.

Mechanism of Natural Sensitizers: Natural dyes, like anthocyanins and chlorophyll, are effective due to their broad absorption range, capturing sunlight by their chromophoric structures, which absorb visible light through conjugated systems. When these dyes absorb photons, their electrons get excited and move to the conduction band of a semiconductor. The dyes are anchored to the semiconductor, allowing electron transfer and oxidation. The dye is then regenerated by accepting electrons from a redox mediator in the electrolyte, restoring it for more light absorption. Meanwhile, the electrons travel through the semiconductor to an electrode, generating electric current, while the mediator recharges the dye.

Efficiency of Natural Photosensitizers: The efficiency of natural photosensitizers varies but has significant promise for efficient light absorption and energy conversion, particularly chlorophyll, a widely studied natural pigment that has PCE up to 2%. Similarly, anthocyanins, derived from fruits like blueberries, exhibit PCE of about 5%, carotenoids from pumpkin and carrots have an efficiency of 1%, while curcumins from turmeric have an efficiency of up to 2%. Besides these, sensitizers derived from animal sources like fish scales and hair have high efficiency, up to 8%, while coal is also a natural material that exhibits PCE of about 5%.

Stability of Natural Sensitizers: Natural dyes are less stable, as these are easily affected by sun exposure or environmental conditions, pH, humidity, and temperature as well. However, extra care, modifications or addition of stabilizers, preservatives can increase their life spam.

Absorption Spectrum of Natural Photosensitizers: Natural sensitizers generally have a broad absorption spectral range from UV to visible, like anthocyanin (400-800nm), chlorophyll (400-450nm & 650-700nm), betalains and carotenoids (400-550nm), curcumins (400-500) and flavonoids (250-500nm).

Advantages of Natural Photosensitizers: Natural dye sensitizers offer a range of compelling advantages that significantly enhance both their environmental and economic benefits.

a. *Renewability & Sustainability:* Derived from renewable materials, these dyes are more eco-friendly compared to synthetic alternatives. For example, anthocyanins from blueberries and red cabbage are not only abundant but also biodegradable, reducing environmental impact and supporting sustainability in solar technology.
b. *Simple Extraction & Cost-effective:* The extraction process for natural dyes is often simpler and more cost-effective, like betalains from beets exemplify this with their affordable extraction methods. *Broad Absorption Spectra:* Natural dyes have broad absorption spectra, such as chlorophyll from green plants, which efficiently captures light across both blue and red wavelengths.
c. Biocompatible & Non-toxic: Natural dyes, like carotenoids from carrots and pumpkins, are biocompatible and non-toxic.
d. *Diverse Color Change:* The diverse color properties of natural dyes, like curcumin from turmeric, which change color depending on pH (yellow in acidic and red in basic conditions), can be optimized for light absorption and efficiency.
e. *Low Carbon Footprints:* Natural dyes generally have a lower carbon footprint, as their extraction and processing consume less energy compared to the production of complex synthetic dyes.

Disadvantages of Natural Photosensitizers: Despite their ecological benefits, natural dye sensitizers have several disadvantages.

a. *Lower Stability:* One of the primary challenges is their limited stability; natural dyes like anthocyanins from blueberries and betalains from beets are prone to degradation under continuous light exposure and oxidative conditions, which can diminish their performance over time. For example, chlorophyll, although efficient in light absorption, often suffers from degradation and reduced efficacy in DSSCs due to its sensitivity to environmental factors.

b. *Low Efficiency & Performance:* Additionally, natural dyes generally exhibit lower quantum efficiency compared to synthetic dyes such as ruthenium complexes, which can achieve efficiencies above 10%. This lower efficiency, coupled with issues related to dye solubility and charge transfer, can limit the overall performance of DSSCs utilizing natural dyes.

c. Change Transfer Issues: The production and processing of natural dyes can sometimes be inconsistent, not always facilitating electron transfer, leading to variability in their quality and effectiveness.

Future prospects of Natural Photosensitizers:
As the world is facing an energy crisis, it is today's requirement to develop or use such material that is more environmentally friendly. Researchers are continuously trying to increase the life span, stability and efficiency of natural sensitizers through chemical modifications.

II.　　Organic (Metal-Free) Dyes
The unique nature (donor-π-acceptor) of organic sensitizers makes them more feasible and attractive as photosensitizers for DSSC with high efficiency and non-toxic nature.

Mechanism of Organic Photosensitizers: In organic compounds, conjugate systems facilitate light absorption. Generally, these compounds have donor groups (D-π-A system), like thiophene and carbazole, and acceptor groups, like cyanoacrylic acid. Sometimes, these have extended conjugated systems like vinyl groups, conjugated chains, rings, and anchoring groups that strongly bind with titanium oxide. After absorption, electrons are promoted from ground state to excited state. This excitation usually occurs as the electron moves from π (lower energy orbit) to π* (high energy orbit).

Efficiency of Organic Photosensitizers: The efficiency of organic sensitizers is much higher than the natural dyes. Their efficiency increased with an increase of conjugate systems (ring/chain), donor groups. Thiophene-based derivatives have high efficiency up to 9% while cyanoacrylic acid derivatives have PCE more than 12%.

Stability of Organic Sensitizers: Organic sensitizers are durable, stable and resistant in normal conditions. However, these sometimes show *photo-degradation* (loss of activity or color via light exposure), *thermal degradation* (damage due to heat), and *oxidative degradation* (damage due to oxidative environment). But modifications can enhance their lifespan and longevity.

Absorption Spectrum of Organic Sensitizers: Organic sensitizers show variable absorption spectral ranges like coumarins 450-470 nm, anthraquinones 400-500 nm, thiazines 300-400nm, conjugate polymers 450-550 nm, aniline derivatives 200-300 nm, and azo dyes 400-500 nm.

Advantages of Organic Photosensitizers: There are several advantages to using them as sensitizers.

a. *Flexibility:* The main advantage of organic sensitizers is their flexibility; can undergo structural modifications to enhance their performance, like D-π-A system.

b. *Cost-Effective:* Thiophene derivatives are normally low-cost as compared to metal complexes and easy to store natural ones.

c. *Low Toxicity:* Another main advantage is low toxicity; these do not contain any toxic metals and are therefore supposed to be environmentally safe.

d. *Easy Modifications:* As these contain different functional groups that are easily modified to increase efficiency, like cyano- or carboxylic derivatives.

e. *Broad Absorption Spectrum:* These also have broad absorption spectra and the ability to absorb light of a long range of wavelengths, like squaraine dyes. 600-850 nm.

Disadvantages of Organic Sensitizers: With several advantages, organic sensitizers also have some disadvantages.

a. *Photostability:* The main disadvantage is their photostability like cyanine dyes that decompose when in contact with UV light.

b. *Electrolyte interaction:* Sometimes, these dyes react with electrolytes, especially when iodine-based electrolytes are used.

c. *Purification challenges & Efficiency:* Another notable disadvantage is their purification after synthesis; efficiency of organic dyes normally decreases in such cases with impurity.

Future prospects for Organic Sensitizers: Organic photosensitizers offer promising potential for energy development in the modern era. However, to fully realize their capabilities, improvements are needed through green synthesis methods, the incorporation of functional groups to broaden the absorption range, and the development of hybrid systems to enhance both efficiency and stability.

III.　　Metal-Based Dyes
Due to high efficiency and excellent stability, metal-based photosensitizers play a pivotal role. These dyes are normally complexes of ruthenium, platinum, palladium, iron, zinc or cobalt that exhibit broad absorption spectra.

Mechanism of Metal-based Photosensitizers: Transition metals like ruthenium or osmium, which are essential for effective light absorption and electron transfer, are used for metal-based dye

sensitizers in DSSC. In these dyes, the transition metal center serves as the primary photoactive site, responsible for absorbing light and exciting electrons. Meanwhile, the surrounding ligands play a dual role: they enhance light absorption by extending the dye's absorption spectrum and anchor the dye to the semiconductor surface, ensuring stable and efficient charge transfer.

Efficiency of Metal-based Sensitizers: The efficiency of metal-based dyes is highest among all the sensitizers used in DSSC, like zinc complexes (13%), ruthenium complexes (13%), iron complexes (7%), and cobalt (10%).

Stability of Metal-based Photosensitizers: Among all the photosensitizers, ruthenium metal-based photosensitizers are good photostable, chemically stable and have the highest lifespan, while iron exhibits lower. Sometimes, these metal-based sensitizers exhibit ligand loss, react with electrolyte or oxidize.

Absorption Spectrum of Metal-based Photosensitizers: Normally, ruthenium-based complexes exhibit a 400-700 nm spectral range, while iron and cobalt are 400-600 nm.

Advantages of Metal-based Sensitizers: Metal-based complexes exhibit impressive advantages.
a. *High Efficiency:* Ruthenium- and osmium-based photosensitizers exhibit high efficiency up to 13%.
b. *Broad Absorption Range:* Ruthenium complexes with their broad absorption range of 400-700 nm.
c. *Excellent stability:* Metal-based dyes show excellent photostability and chemical stability as compared to organic dyes.
d. *Low toxicity:* Certain metals like copper, cobalt and zinc complexes are less toxic and eco-friendly with high efficiency.

e. *Flexible nature:* Metal complexes have a flexible nature due to their bonding atoms, ligand modifications, metal combination and ligand variation.

Disadvantages of Metal-Based Photosensitizers: Despite their high efficiency, metal-based dyes have some disadvantages.
a. *Toxic nature:* Ruthenium-based sensitizers are toxic and raise environmental issues.
b. High Cost: Some metals like osmium, ruthenium, and palladium are expensive and need high costs for commercialization.
c. Decomposition: Some metal-based sensitizers decompose and undergo ligand-dissociate or ligand-exchange reactions in the presence of electrolytes, like cobalt complexes, that can easily react with electrolytes.

Future prospects for Metal-Based Photosensitizers: The future of metal-based sensitizers for dye-sensitized solar cells (DSSCs) looks very promising. Advancements are being made in developing new metal complexes that enhance efficiency by extending light absorption into the infrared spectrum. Efforts to reduce costs include using more abundant and affordable metals like iron and copper, along with optimizing production methods. Key improvements are also focused on enhancing the stability of these sensitizers, increasing their photostability, and ensuring compatibility with various electrolytes. With a growing emphasis on sustainability through eco-friendly and recyclable materials and the integration of DSSCs with technologies such as hybrid systems and flexible substrates, these advancements are set to make metal-based DSSCs more efficient, cost-effective, and commercially viable, leading to broader adoption in the renewable energy sector.

Based on the above data, a brief comparison between these sensitizers is presented below for better understanding.

Property	Natural	Metal-free	Metal-based
Source	Extracted from plant or any living material	Synthesized	Synthesized, often used transition metal complexes
Light absorption range	Limited	Broad	Broad
Toxicity	Non-toxic	Vary, low as compared to metal-based	High due to presence of heavy metals
Cost	Low	Low but vary	High/expensive
Bio-degradability	High	Vary	Low/none
Eco-friendly nature	High	Differ	Very low/none
Stability	Low, normally decompose on exposure to light	Moderate, sometimes decompose on exposure to light	High
Sensitivity	Low	High as compared to natural	High
Flexibility & modification	None	High due to tailored structure	High
Efficiency	~10	~11	~14
Example	Chlorophyll, anthocyanin etc.	Indole, imidazole, hydrazone, aromatics, pyridines etc.	Ruthenium, osmium, cobalt etc., metal complexes

Jabeen M et al. JOTCSA. 2025; 12(1): 35-46

REVIEW ARTICLE

5. CONCLUSION

Currently, the world is facing a serious energy crisis. Increasing consumption has led to the depletion of non-renewable energy resources. Solar energy is considered to be the most efficient renewable resource due to its abundant supply. One of the most promising energy sources for the future of our planet is solar energy, which plays a crucial role in meeting the global energy challenge. Compared to other forms of energy, solar energy is inexpensive and continuous. In recent years, solar and photovoltaic cells have become a hot topic. These cells convert sunlight directly into electricity via photovoltaic effect. Among all the solar cells, dye-sensitized solar cells are the thin-filmed, 3rd-generation solar cells and are widely used due to easy fabrication, a large number of sensitizers, inexpensiveness, and broad EM spectra. Photosensitive dyes absorb sunlight, generating electron-hole pairs. A photosensitive dye can be extracted from living organisms or synthetics, e.g., metal-based or metal-free compounds. Researchers are exploring novel sensitizers to improve DSSC performance, but the efficiency of these devices is less than 20%. During the past few years, the energy crisis has become the most potent problem. The current review summarized all possible dye sensitizers (natural and synthetic) used/synthesized during the last 15 years with 310 references, 145 natural sensitizers, 275 organic-based (metal-free) and 115 metal-based photosensitizers, and hope that it will be a potential increment in future research.

6. REFERENCES

1. Joy C. A review-The potential of natural dyes for dye sensitized solar cells. Int J Innov Sci Res Technol [Internet]. 2017;2(10):579–84. Available from: <URL>.

2. Dhilipan J, Vijayalakshmi N, Shanmugam DB, Jai Ganesh R, Kodeeswaran S, Muralidharan S. Performance and efficiency of different types of solar cell material – A review. Mater Today Proc [Internet]. 2022 Jan 1;66:1295–302. Available from: <URL>.

3. Ameri T, Li N, Brabec CJ. Highly efficient organic tandem solar cells: A follow up review. Energy Environ Sci [Internet]. 2013 Jul 17;6(8):2390–413. Available from: <URL>.

4. Shahzad U, Asgarpoor S. A comprehensive review of protection schemes for distributed generation. Energy Power Eng [Internet]. 2017 Aug 7;9(8):430–63. Available from: <URL>.

5. Shahzad U. The importance of renewable energy sources in Pakistan. Durreesamin J [Internet]. 2015;1(3):1–5. Available from: <URL>.

6. Pablo CCV, Enrique RR, José ARG, Enrique MP, Juan LH, Eddie NAM. Construction of dye-sensitized solar cells (DSSC) with natural pigments. Mater Today Proc [Internet]. 2016 Jan 1;3(2):194–200. Available from: <URL>.

7. Jabeen M, Tarıq K, Hussain SU. Bioplastic an alternative to plastic in modern world: A systemized review. Environ Res Technol [Internet]. 2024 Dec 31;7(4):614–25. Available from: <URL>.

8. Tripathi L, Mishra AK, Dubey AK, Tripathi CB, Baredar P. Renewable energy: An overview on its contribution in current energy scenario of India. Renew Sustain Energy Rev [Internet]. 2016 Jul 1;60:226–33. Available from: <URL>.

9. Hanif I, Aziz B, Chaudhry IS. Carbon emissions across the spectrum of renewable and nonrenewable energy use in developing economies of Asia. Renew Energy [Internet]. 2019 Dec 1;143:586–95. Available from: <URL>.

10. Shahzad U. The need for renewable energy sources. Int J Inf Technol Electr Eng [Internet]. 2015;4(4):16–8. Available from: <URL>.

11. Salim RA, Shafiei S. Urbanization and renewable and non-renewable energy consumption in OECD countries: An empirical analysis. Econ Model [Internet]. 2014 Feb 1;38:581–91. Available from: <URL>.

12. Kannan N, Vakeesan D. Solar energy for future world: - A review. Renew Sustain Energy Rev [Internet]. 2016 Sep 1;62:1092–105. Available from: <URL>.

13. Dinçer F. The analysis on photovoltaic electricity generation status, potential and policies of the leading countries in solar energy. Renew Sustain Energy Rev [Internet]. 2011 Jan 1;15(1):713–20. Available from: <URL>.

14. Schmidt T, Mangold D, Müller-Steinhagen H. Central solar heating plants with seasonal storage in Germany. Sol Energy [Internet]. 2004 Jan 1;76(1–3):165–74. Available from: <URL>.

15. Soile I. The economic and environmental challenges of energy supply disruptions in China. Eur J Econ Financ Adm Sci [Internet]. 2011;34:87–98. Available from: <URL>.

16. Deandra PP, Santoso H, Witono JRB. Carbon based sulfonated catalyst as an environment friendly material: A review. In: AIP Conference Proceedings [Internet]. American Institute of Physics Inc.; 2022. p. 040006. Available from: <URL>.

17. Jacobson MZ, Delucchi MA. A path to sustainable energy by 2030. Sci Am [Internet]. 2009;301(5):58–65. Available from: <URL>.

18. Sharma S, Jain KK, Sharma A. Solar Cells: In research and applications—A review. Mater Sci Appl [Internet]. 2015 Dec 1;06(12):1145–55. Available from: <URL>.

19. Al-Ezzi AS, Ansari MNM. Photovoltaic solar cells: A review. Appl Syst Innov [Internet]. 2022 Jul 8;5(4):67. Available from: <URL>.

20. Snaith HJ. The perils of solar cell efficiency measurements. Nat Photonics [Internet]. 2012 Jun 29;6(6):337–40. Available from: <URL>.

Jabeen M et al. JOTCSA. 2025; 12(1): 35-46

REVIEW ARTICLE

21. Sharma M, Gupta S, Prasad S, Bharatiya PK, Mishra D. First principles study of the influence of metallic-doping on crystalline ZnS: From efficiency aspects for use in a ZnS based dye sensitized solar cell (DSSC). Integr Ferroelectr [Internet]. 2018 Nov 22;194(1):96–103. Available from: <URL>.

22. El Chaar L, lamont LA, El Zein N. Review of photovoltaic technologies. Renew Sustain Energy Rev [Internet]. 2011 Jun 1;15(5):2165–75. Available from: <URL>.

23. Kenu E. Sarah. A review of solar photovoltaic technologies. Int J Eng Res [Internet]. 2020 Jul 18;9(7):741–9. Available from: <URL>.

24. Ouedraogo S, Sam R, Ouedraogo F, Kebre MB, Zougmore F, Ndjaka JM, et al. Optimization of copper indium gallium di-selenide (CIGS) based solar cells by back grading. In: 2013 Africon [Internet]. IEEE; 2013. p. 1–6. Available from: <URL>.

25. Fairbrother A, Saucedo E, Fontane X, Izquierdo-Roca V, Sylla D, Espindola-Rodriguez M, et al. Preparation of 4.8% efficiency $Cu_2ZnSnSe_4$ based solar cell by a two step process. In: 2012 38th IEEE Photovoltaic Specialists Conference [Internet]. IEEE; 2012. p. 002679–84. Available from: <URL>.

26. Fairbrother A, Fontané X, Izquierdo-Roca V, Espíndola-Rodríguez M, López-Marino S, Placidi M, et al. On the formation mechanisms of Zn-rich Cu_2ZnSnS_4 films prepared by sulfurization of metallic stacks. Sol Energy Mater Sol Cells [Internet]. 2013 May 1;112:97–105. Available from: <URL>.

27. Imamzai M, Aghaei M, Thayoob YHM, Forouzanfar M. A review on comparison between traditional silicon solar cells and thin- film CdTe solar cells. In: Proceedings National Graduate Conference [Internet]. 2012. Available from: <URL>.

28. Green MA, Dunlop ED, Yoshita M, Kopidakis N, Bothe K, Siefer G, et al. Solar cell efficiency tables (Version 64). Prog Photovoltaics Res Appl [Internet]. 2024 Jul 2;32(7):425–41. Available from: <URL>.

29. Masafumi Y. High-efficiency GaAs-based solar cells. In: Muzibur Rahman M, Mohammed Asiri A, Khan A, Inamuddin, Tabbakh T, editors. Post-Transition Metals [Internet]. IntechOpen; 2021. Available from: <URL>.

30. Vigil-Galán O, Courel M, Andrade-Arvizu JA, Sánchez Y, Espíndola-Rodríguez M, Saucedo E, et al. Route towards low cost-high efficiency second generation solar cells: Current status and perspectives. J Mater Sci Mater Electron [Internet]. 2015 Aug 30;26(8):5562–73. Available from: <URL>.

31. Kim HS, Lee CR, Im JH, Lee KB, Moehl T, Marchioro A, et al. Lead Iodide perovskite sensitized all-solid-state submicron thin film mesoscopic solar cell with efficiency exceeding 9%. Sci Rep [Internet]. 2012 Aug 21;2(1):591. Available from: <URL>.

32. Bermel P, Ghebrebrhan M, Chan W, Yeng YX, Araghchini M, Hamam R, et al. Design and global optimization of high-efficiency thermophotovoltaic systems. Opt Express [Internet]. 2010 Sep 13;18(S3):A314. Available from: <URL>.

33. O'Regan B, Grätzel M. A low-cost, high-efficiency solar cell based on dye-sensitized colloidal TiO_2 films. Nature [Internet]. 1991 Oct 24;353(6346):737–40. Available from: <URL>.

34. Yin Z, Zhu J, He Q, Cao X, Tan C, Chen H, et al. Graphene-based materials for solar cell applications. Adv Energy Mater [Internet]. 2014 Jan 23;4(1):1300574. Available from: <URL>.

35. Ning Z, Gong X, Comin R, Walters G, Fan F, Voznyy O, et al. Quantum-dot-in-perovskite solids. Nature [Internet]. 2015 Jul 16;523(7560):324–8. Available from: <URL>.

36. Yan J, Saunders BR. Third-generation solar cells: a review and comparison of polymer:fullerene, hybrid polymer and perovskite solar cells. RSC Adv [Internet]. 2014 Sep 12;4(82):43286–314. Available from: <URL>.

37. Piliego C, Protesescu L, Bisri SZ, Kovalenko M V., Loi MA. 5.2% efficient PbS nanocrystal schottky solar cells. Energy Environ Sci [Internet]. 2013 Sep 20;6(10):3054–9. Available from: <URL>.

38. Ge Z, Qiao J, Li Y, Song J, Zhang C, Fu Z, et al. Over 18% efficiency of all-polymer solar cells with long-term stability enabled by Y6 as a solid additive. Adv Mater [Internet]. 2023 Jul 24;35(28):2301906. Available from: <URL>.

39. LaPotin A, Schulte KL, Steiner MA, Buznitsky K, Kelsall CC, Friedman DJ, et al. Thermophotovoltaic efficiency of 40%. Nature [Internet]. 2022 Apr 14;604(7905):287–91. Available from: <URL>.

40. Shah N, Shah AA, Leung PK, Khan S, Sun K, Zhu X, et al. A review of third generation solar cells. Processes [Internet]. 2023 Jun 20;11(6):1852. Available from: <URL>.

41. Suhail A, Pan G, Jenkins D, Islam K. Improved efficiency of graphene/Si Schottky junction solar cell based on back contact structure and DUV treatment. Carbon N Y [Internet]. 2018 Apr 1;129:520–6. Available from: <URL>.

42. Kim T, Jin X, Song JH, Jeong S, Park T. Efficiency limit of colloidal quantum dot solar cells: Effect of optical interference on active layer absorption. ACS Energy Lett [Internet]. 2020 Jan 10;5(1):248–51. Available from: <URL>.

43. Zhou Y, Chen Y, Zhang Q, Zhou Y, Tai M, Koumoto K, et al. A highly-efficient concentrated perovskite solar cell-thermoelectric generator tandem system. J Energy Chem [Internet]. 2021 Aug 1;59:730–5. Available from: <URL>.

44. Mayer AC, Scully SR, Hardin BE, Rowell MW, McGehee MD. Polymer-based solar cells. Mater Today [Internet]. 2007 Nov 1;10(11):28–33. Available from: <URL>.

Jabeen M et al. JOTCSA. 2025; 12(1): 35-46

REVIEW ARTICLE

45. Sharma K, Sharma V, Sharma SS. Dye-sensitized solar cells: Fundamentals and current status. Nanoscale Res Lett [Internet]. 2018 Dec 28;13(1):381. Available from: <URL>.

46. Wei D. Dye sensitized solar cells. Int J Mol Sci [Internet]. 2010 Mar 16;11(3):1103–13. Available from: <URL>.

47. Baby R, Nixon PD, Kumar NM, Subathra MSP, Ananthi N. A comprehensive review of dye-sensitized solar cell optimal fabrication conditions, natural dye selection, and application-based future perspectives. Environ Sci Pollut Res [Internet]. 2022 Jan 21;29(1):371–404. Available from: <URL>.

48. Fitra M, Daut I, Gomesh N, Irwanto M, Irwan YM. Dye solar cell using syzigium oleina organic dye. Energy Procedia [Internet]. 2013 Jan 1;36:341–8. Available from: <URL>.

49. Srinivasu P, Singh SP, Islam A, Han L. Solar energy conversion by dye-sensitized photovoltaic cells using high surface area mesoporous carbon counter electrode. Adv Optoelectron [Internet]. 2011 Oct 10;2011(1):1–4. Available from: <URL>.

50. Ito S, Ha NLC, Rothenberger G, Liska P, Comte P, Zakeeruddin SM, et al. High-efficiency (7.2%) flexible dye-sensitized solar cells with Ti-metal substrate for nanocrystalline-TiO_2 photoanode. Chem Commun [Internet]. 2006 Sep 26;2006(38):4004–6. Available from: <URL>.

51. Hagfeldt A, Boschloo G, Sun L, Kloo L, Pettersson H. Dye-sensitized solar cells. Chem Rev [Internet]. 2010 Nov 10;110(11):6595–663. Available from: <URL>.

52. Kharul A, Yusuf NM, Mustafar S, Borines ML, Kusumawati EN, Hashim N. Versatility of photosensitizers in dye-sensitized solar cells (DSSCs). Biointerface Res Appl Chem [Internet]. 2021 Dec 13;12(6):8543–60. Available from: <URL>.

53. Michaels H, Rinderle M, Freitag R, Benesperi I, Edvinsson T, Socher R, et al. Dye-sensitized solar cells under ambient light powering machine learning: Towards autonomous smart sensors for the internet of things. Chem Sci [Internet]. 2020 Mar 18;11(11):2895–906. Available from: <URL>.

54. Sekaran PD, Marimuthu R. An extensive analysis of dye-sensitized solar cell (DSSC). Brazilian J Phys [Internet]. 2024 Feb 8;54(1):28. Available from: <URL>.

55. Mohiuddin O, Obaidullah M, Sabah C. Improvement in dye sensitized solar cells from past to present. Opt Quantum Electron [Internet]. 2018 Oct 5;50(10):377. Available from: <URL>.

56. Freitag M, Teuscher J, Saygili Y, Zhang X, Giordano F, Liska P, et al. Dye-sensitized solar cells for efficient power generation under ambient lighting. Nat Photonics [Internet]. 2017 Jun 1;11(6):372–8. Available from: <URL>.

57. Sheehan S, Surolia PK, Byrne O, Garner S, Cimo P, Li X, et al. Flexible glass substrate based dye sensitized solar cells. Sol Energy Mater Sol Cells [Internet]. 2015 Jan 1;132:237–44. Available from: <URL>.

58. Patni N, Sharma P, Parikh M, Joshi P, Pillai SG. Cost effective approach of using substrates for electrodes of enhanced efficient dye sensitized solar cell. Mater Res Express [Internet]. 2018 Aug 17;5(9):095509. Available from: <URL>.

59. Marques A dos S, da Silva VAS, Ribeiro ES, Malta LFB. Dye-sensitized solar cells: components screening for glass substrate, counter-electrode, photoanode and electrolyte. Mater Res [Internet]. 2020 Nov 23;23(5):e20200168. Available from: <URL>.

60. Yeoh ME, Chan KY. Recent advances in photo-anode for dye-sensitized solar cells: A review. Int J Energy Res [Internet]. 2017 Dec 1;41(15):2446–67. Available from: <URL>.

61. Ye M, Wen X, Wang M, Iocozzia J, Zhang N, Lin C, et al. Recent advances in dye-sensitized solar cells: from photoanodes, sensitizers and electrolytes to counter electrodes. Mater Today [Internet]. 2015 Apr 1;18(3):155–62. Available from: <URL>.

62. Bagheri O, Dehghani H, Afrooz M. Pyridine derivatives; new efficient additives in bromide/tribromide electrolyte for dye sensitized solar cells. RSC Adv [Internet]. 2015 Oct 12;5(105):86191–8. Available from: <URL>.

63. Zhao M, Zhang L, Liu M, Dong Y, Zou C, Hu Y, et al. Growth of atomically thin MoS_2 flakes on high-κ substrates by chemical vapor deposition. J Mater Sci [Internet]. 2018 Mar 20;53(6):4262–73. Available from: <URL>.

64. Chen W, Qiu Y, Zhong Y, Wong KS, Yang S. High-efficiency dye-sensitized solar cells based on the composite photoanodes of SnO_2 nanoparticles/ZnO nanotetrapods. J Phys Chem A [Internet]. 2010 Mar 11;114(9):3127–38. Available from: <URL>.

65. Chiang TL, Chou CS, Wu DH, Hsiung CM. Applications of P-type NiO in dye-sensitized solar cells. Adv Mater Res [Internet]. 2011 May 12;239–242:1747–50. Available from: <URL>.

66. Alami AH, Rajab B, Abed J, Faraj M, Hawili AA, Alawadhi H. Investigating various copper oxides-based counter electrodes for dye sensitized solar cell applications. Energy [Internet]. 2019 May 1;174:526–33. Available from: <URL>.

67. Hosseinnezhad M, Gharanjig K, Yazdi MK, Zarrintaj P, Moradian S, Saeb MR, et al. Dye-sensitized solar cells based on natural photosensitizers: A green view from Iran. J Alloys Compd [Internet]. 2020 Jul 5;828:154329. Available from: <URL>.

68. Arof AK, Ping TL. Chlorophyll as photosensitizer in dye-sensitized solar cells. In: Jacob-Lopes E, Zepka LQ, Queiroz MI, editors. Chlorophyll

Jabeen M et al. JOTCSA. 2025; 12(1): 35-46

REVIEW ARTICLE

[Internet]. Rijeka, Croatia: InTech; 2017. Available from: <URL>.

69. Bartkowiak A, Korolevych O, Chiarello GL, Makowska-Janusik M, Zalas M. Experimental and theoretical insight into DSSCs mechanism influenced by different doping metal ions. Appl Surf Sci [Internet]. 2022 Sep 30;597:153607. Available from: <URL>.

70. Lee CP, Li CT, Ho KC. Use of organic materials in dye-sensitized solar cells. Mater Today [Internet]. 2017 Jun 1;20(5):267–83. Available from: <URL>.

71. Grätzel M. Solar energy conversion by dye-sensitized photovoltaic cells. Inorg Chem [Internet]. 2005 Oct 1;44(20):6841–51. Available from: <URL>.

72. Jilakian M, Ghaddar TH. Eco-friendly aqueous dye-sensitized solar cell with a copper(I/II) electrolyte system: Efficient performance under ambient light conditions. ACS Appl Energy Mater [Internet]. 2022 Jan 24;5(1):257–65. Available from: <URL>.

73. Yella A, Lee HW, Tsao HN, Yi C, Chandiran AK, Nazeeruddin MK, et al. Porphyrin-sensitized solar cells with cobalt (II/III)–based redox electrolyte exceed 12 percent efficiency. Science [Internet]. 2011 Nov 4;334(6056):629–34. Available from: <URL>.

74. Feldt SM, Gibson EA, Gabrielsson E, Sun L, Boschloo G, Hagfeldt A. Design of organic dyes and cobalt polypyridine redox mediators for high-efficiency dye-sensitized solar cells. J Am Chem Soc [Internet]. 2010 Nov 24;132(46):16714–24. Available from: <URL>.

75. Lee CP, Chu TC, Chang LY, Lin JJ, Ho KC. Solid-state Ionic liquid based electrolytes for dye-sensitized solar cells. In: Jacob-Lopes E, Zepka LQ, Queiroz MI, editors. Chlorophyll [Internet]. Rijeka, Croatia: InTech; 2017. Available from: <URL>.

76. Gnanasekar S, Kollu P, Jeong SK, Grace AN. Pt-free, low-cost and efficient counter electrode with carbon wrapped VO_2(M) nanofiber for dye-sensitized solar cells. Sci Rep [Internet]. 2019 Mar 26;9(1):5177. Available from: <URL>.

77. Wu J, Lan Z, Lin J, Huang M, Huang Y, Fan L, et al. Counter electrodes in dye-sensitized solar cells. Chem Soc Rev [Internet]. 2017 Oct 2;46(19):5975–6023. Available from: <URL>.

78. Ahmed U, Alizadeh M, Rahim NA, Shahabuddin S, Ahmed MS, Pandey AK. A comprehensive review on counter electrodes for dye sensitized solar cells: A special focus on Pt-TCO free counter electrodes. Sol Energy [Internet]. 2018 Nov 1;174:1097–125. Available from: <URL>.

79. Thomas S, Deepak TG, Anjusree GS, Arun TA, Nair S V., Nair AS. A review on counter electrode materials in dye-sensitized solar cells. J Mater Chem A [Internet]. 2014 Mar 4;2(13):4474–90. Available from: <URL>.

80. Wu CS, Chang TW, Teng H, Lee YL. High performance carbon black counter electrodes for dye-sensitized solar cells. Energy [Internet]. 2016 Nov 15;115:513–8. Available from: <URL>.

81. Wang H, Hu YH. Graphene as a counter electrode material for dye-sensitized solar cells. Energy Environ Sci [Internet]. 2012 Jul 18;5(8):8182–8. Available from: <URL>.

82. Chou CS, Hsiung CM, Wang CP, Yang RY, Guo MG. Preparation of a counter electrode with *P*-type NiO and its applications in dye-sensitized solar cell. Int J Photoenergy [Internet]. 2010 Jan 1;2010(1):902385. Available from: <URL>.

83. Richhariya G, Kumar A, Shukla AK, Shukla KN, Meikap BC. Effect of different counter electrodes on power conversion efficiency of DSSCs. J Electron Mater [Internet]. 2023 Jan 20;52(1):60–71. Available from: <URL>.

84. Jamalullail N, Mohamad IS, Norizan MN, Baharum NA, Mahmed N. Short review: Natural pigments photosensitizer for dye-sensitized solar cell (DSSC). In: 2017 IEEE 15th Student Conference on Research and Development (SCOReD) [Internet]. IEEE; 2017. p. 344–9. Available from: <URL>.

85. Ghernaout D, Boudjemline A, Elboughdiri N. Electrochemical engineering in the core of the dye-sensitized solar cells (DSSCs). OALib [Internet]. 2020 Mar 5;07(03):1–12. Available from: <URL>.

86. Francis OI, Ikenna A. Review of dye-sensitized solar cell (DSSCs) development. Nat Sci [Internet]. 2021 Dec 7;13(12):496–509. Available from: <URL>.

87. Bera S, Sengupta D, Roy S, Mukherjee K. Research into dye-sensitized solar cells: A review highlighting progress in India. J Phys Energy [Internet]. 2021 Jul 1;3(3):032013. Available from: <URL>.

88. Bej S, Ghosh P, Majumdar G, Murmu NC, Banerjee P. Design and synthesis of new ruthenium coordination complex as efficient dye in DSSC Like alternative energy resources with a bird's eye view on strategies towards GHGs mitigation. In: Encyclopedia of Renewable and Sustainable Materials [Internet]. Elsevier; 2020. p. 395–410. Available from: <URL>.

89. Zhang L, Cole JM. Anchoring groups for dye-sensitized solar cells. ACS Appl Mater Interfaces [Internet]. 2015 Feb 18;7(6):3427–55. Available from: <URL>.

90. Ladomenou K, Kitsopoulos TN, Sharma GD, Coutsolelos AG. The importance of various anchoring groups attached on porphyrins as potential dyes for DSSC applications. RSC Adv [Internet]. 2014 May 14;4(41):21379–404. Available from: <URL>.

91. Rafique S, Rashid I, Sharif R. Cost effective dye sensitized solar cell based on novel Cu polypyrrole multiwall carbon nanotubes nanocomposites counter electrode. Sci Rep [Internet]. 2021 Jul

Jabeen M et al. JOTCSA. 2025; 12(1): 35-46

REVIEW ARTICLE

21;11(1):14830. Available from: <URL>.

92. Younas M, Gondal MA, Dastageer MA, Harrabi K. Efficient and cost-effective dye-sensitized solar cells using MWCNT-TiO$_2$ nanocomposite as photoanode and MWCNT as Pt-free counter electrode. Sol Energy [Internet]. 2019 Aug 1;188:1178–88. Available from: <URL>.

93. Sen A, Putra MH, Biswas AK, Behera AK, Groβ A. Insight on the choice of sensitizers/dyes for dye sensitized solar cells: A review. Dye Pigment [Internet]. 2023 May 1;213:111087. Available from: <URL>.

94. Agarwal R, Vyas Y, Chundawat P, Dharmendra, Ameta C. Outdoor performance and stability assessment of dye-sensitized solar cells (DSSCs). In: Aghaei M, editor. Solar Radiation - Measurement, Modeling and Forecasting Techniques for Photovoltaic Solar Energy Applications [Internet]. IntechOpen; 2021. Available from: <URL>.

95. Shukor NIA, Chan KY, Thien GSH, Yeoh ME, Low PL, Devaraj NK, et al. A green approach to natural dyes in dye-sensitized solar cells. Sensors [Internet]. 2023 Oct 12;23(20):8412. Available from: <URL>.

96. Parasuraman D, Ramakrishnan M. A review on dye-sensitized solar cells (DSSCs), materials and applications. Iran J Mater Sci Eng [Internet]. 2023 Mar;20(1):1–23. Available from: <URL>.

97. Calogero G, Bartolotta A, Di Marco G, Di Carlo A, Bonaccorso F. Vegetable-based dye-sensitized solar cells. Chem Soc Rev [Internet]. 2015 May 12;44(10):3244–94. Available from: <URL>.

98. Mekapogu M, Vasamsetti BMK, Kwon OK, Ahn MS, Lim SH, Jung JA. Anthocyanins in floral colors: biosynthesis and regulation in chrysanthemum flowers. Int J Mol Sci [Internet]. 2020 Sep 7;21(18):6537. Available from: <URL>.

99. Derince B, Gorgun K, Caglar Y, Caglar M. Architectural design of new conjugated systems carrying donor-π-acceptor groups (carbazole-CF3): Characterizations, optical, photophysical properties and DSSC's applications. J Mol Struct [Internet]. 2022 Feb 15;1250:131689. Available from: <URL>.

100. Saad Ebied M, Dongol M, Ibrahim M, Nassary M, Elnobi S, Abuelwafa AA. Effect of carboxylic acid and cyanoacrylic acid as anchoring groups on Coumarin 6 dye for dye-sensitized solar cells: DFT and TD-DFT study. Struct Chem [Internet]. 2022 Dec 16;33(6):1921–33. Available from: <URL>.

101. Nitha PR, Soman S, John J. Indole fused heterocycles as sensitizers in dye-sensitized solar cells: An overview. Mater Adv [Internet]. 2021 Oct 4;2(19):6136–68. Available from: <URL>.

102. Jabeen M. A comprehensive review on analytical applications of hydrazone derivatives. J Turkish Chem Soc Sect A Chem [Internet]. 2022 Aug 31;9(3):663–98. Available from: <URL>.

103. Zou J, Yan Q, Li C, Lu Y, Tong Z, Xie Y. Light-absorbing pyridine derivative as a new electrolyte additive for developing efficient porphyrin dye-sensitized solar cells. ACS Appl Mater Interfaces [Internet]. 2020 Dec 23;12(51):57017–24. Available from: <URL>.

104. Higashino T, Imahori H. Porphyrins as excellent dyes for dye-sensitized solar cells: Recent developments and insights. Dalt Trans [Internet]. 2015 Dec 9;44(2):448–63. Available from: <URL>.

105. Mahadevi P, Sumathi S. Mini review on the performance of schiff base and their metal complexes as photosensitizers in dye-sensitized solar cells. Synth Commun [Internet]. 2020 Aug 2;50(15):2237–49. Available from: <URL>.

106. Meyer TJ, Meyer GJ, Pfennig BW, Schoonover JR, Timpson CJ, Wall JF, et al. Molecular-level electron transfer and excited state assemblies on surfaces of metal oxides and glass. Inorg Chem [Internet]. 1994 Aug 1;33(18):3952–64. Available from: <URL>.

107. El-Agez TM, Taya SA, Elrefi KS, Abdel-Latif MS. Dye-sensitized solar cells using some organic dyes as photosensitizers. Opt Appl [Internet]. 2014;44(2):345–51. Available from: <URL>.

108. Arjmand F, Rashidi Ranjbar Z, Fatemi E. G H. Effect of dye complex structure on performance in DSSCs; An experimental and theoretical study. Heliyon [Internet]. 2022 Nov 1;8(11):e11692. Available from: <URL>.

109. Bashir R, Makhdoom AR, Bilal MK, Ahmad Badar M. Comparative study of the photovoltaic behavior of ruthenium and the other organic and inorganic dye-sensitized solar cells (DSSC). Optik (Stuttg) [Internet]. 2018 Mar 1;157:11–5. Available from: <URL>.

110. Pawlus K, Jarosz T. Transition metal coordination compounds as novel materials for dye-sensitized solar cells. Appl Sci [Internet]. 2022 Mar 28;12(7):3442. Available from: <URL>.

111. Linfoot CL, Richardson P, McCall KL, Durrant JR, Morandeira A, Robertson N. A nickel-complex sensitiser for dye-sensitised solar cells. Sol Energy [Internet]. 2011 Jun 1;85(6):1195–203. Available from: <URL>.

112. Mauri L, Colombo A, Dragonetti C, Fagnani F. A fascinating trip into iron and copper dyes for DSSCs. Inorganics [Internet]. 2022 Sep 10;10(9):137. Available from: <URL>.

113. Muddassir M, Alarifi A, Abduh NAY, Afzal M. New isomeric pyridyl imine zinc(II) complexes as potential co-sensitizers for state of the Art N719 dye in DSSC. J Mol Struct [Internet]. 2021 Dec 15;1246:131191. Available from: <URL>.

Investigation of Novel Hybrid Europium/TEMPTMA-based Neutral pH Aqueous Redox Flow Batteries

Ali Tuna[1,2]* iD , Pekka Peljo[1] iD

[1]University of Turku, Division of Materials Engineering, Vesilinnantie 5, Turku FI-20014, Finland.
[2]University of Turku, Department of Chemistry, Henrikinkatu 2, Turku FI-20014, Finland.

Abstract: In this study, Eu^{3+}/TEMPTMA-based hybrid aqueous redox flow battery system at 1.35 V in neutral pH containing 1 M KCl media was introduced and this battery system was monitored for a long-term cycling performance. During battery and electrochemical studies, capacity change, self-discharge rate and coulombic efficiencies are examined and diffusion constant (D_0) values are calculated for Eu^{3+} and TEMPTMA respectively. As a result, the adopted Eu^{3+}/TEMPTMA-based aqueous redox flow battery system exhibits good performance, reversibility and stability such as >99.97% per cycle (>99.88% per day) discharge capacity within containing 0.25 M Eu^{3+} in 1 M KCl as negolyte at 120 cycles and 29 days battery testing against little excess of 0.5 M TEMPTMA in 1 M KCl as posolyte.

1. INTRODUCTION

Energy arrangements are essential for governments to make strides the environment and decrease their reliance on remote vitality sources (1). In this manner, renewable vitality frameworks are accepting more consideration than ever. On the other hand, vitality capacity gadgets can guarantee the long-term maintainability of renewable energies (2).

Redox flow batteries (RFBs) are a striking innovation course among existing vitality capacity frameworks (3). These batteries have a structure where electrolyte arrangements are put away in two partitioned tanks and vitality is delivered through chemical responses in one cell when it is compared to traditional batteries (4). One of the greatest preferences of RFBs is that their vitality and control capacities can be scaled autonomously which is of course related to the utilized chemicals in such battery frameworks (5). Integration with renewable energy sources such as solar power and/or wind power, RFBs may give long term applications with higher/longer vitality capacities as extraordinary advantage (6). There is also a calculate that creates it troublesome for such vitality capacity framework to be commercially far reaching due to utilized chemicals' costs and components in case of large-scale application (7).
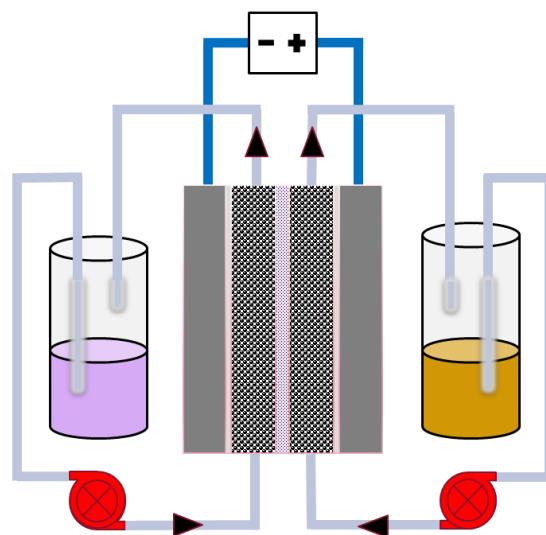
Scheme 1: The schematic illustration of redox-flow battery system including power source, redox cell (electrodes, ion exchange membrane, current collectors), reservoirs, tubing and pumps.

Aqueous redox flow batteries (ARFBs) are defined as water-based electrolytes to store and release energy (8). Non-aqueous redox flow batteries (NARFBs) are defined as organo-solvent based electrolytes (9). Water-based electrolytes provides superior energy and higher ionic conductivity in redox forms. In addition, the low cost and easy accessibility of water and salts make these batteries economical and non-flammability also increases safety in utilize (10). All properties can be numbered as their points of interest in comparison to non-aqueous RFBs, aqueous RFBs are more naturally promising (11).

A greater variety of chemicals are available through hybrid redox flow batteries (HRFBs), which integrate both organic and inorganic components (12). This gives you additional choices for enhancing battery performance. Generally speaking, hybrid systems provide a better energy density than pure systems. In particular, hybrid systems have great promise for integrating renewable energy sources. More energy storage capacity results from this (13). However,

depending on the chemical combinations used, hybrid batteries may also be more affordable. In general, organic components are less expensive than inorganic ones, and overall expenses can be decreased by combining them (14). Longer life and improved chemical stability can be obtained by combining the benefits of both organic and inorganic components in these hybrid systems. All things considered, hybrid redox flow batteries are versatile and may be tailored to meet a range of energy storage requirements (15).

Europium is one of the rare lanthanide group metals (16). It has been suggested to be used in aqueous redox flow batteries in the literature due to its relative electrochemical stability, reversibility and its reasonable production amount and cost when compared to traditional vanadium-based redox flow batteries (16,17). Eu^{3+}/Eu^{2+} reduction can be comparable with other redox-active species (Table 1).

Table 1: Potential and role comparisons of redox-active species in aqueous media.

Redox-active species	Potential (V vs SHE)	Posolyte/Negolyte
$dMe\text{-}Vg^{2+}$	-0.45	Negolyte
Eu^{3+}	-0.36	Negolyte
$bPpN(Me)_3\text{-}Vg^{2+}$	-0.33	Negolyte
V^{3+}	-0.25	Negolyte
$[Fc\text{-}CH_2N(Me)_3]^+$	+0.61	Posolyte
Fe^{2+}	+0.77	Posolyte
$TEMPTMA^+$	+0.98	Posolyte
VO^{2+}	+1.00	Posolyte

In this study, a Eu^{3+}/TEMPTMA-based which adopts one-electron battery system at 1.35 V in neutral pH containing 1 M KCl media is tested (Scheme 2). During battery and electrochemical studies, capacity

change, charge-discharge and coulombic efficiencies are examined, and diffusion constant (D_0) values are calculated for Eu^{3+} and TEMPTMA respectively.
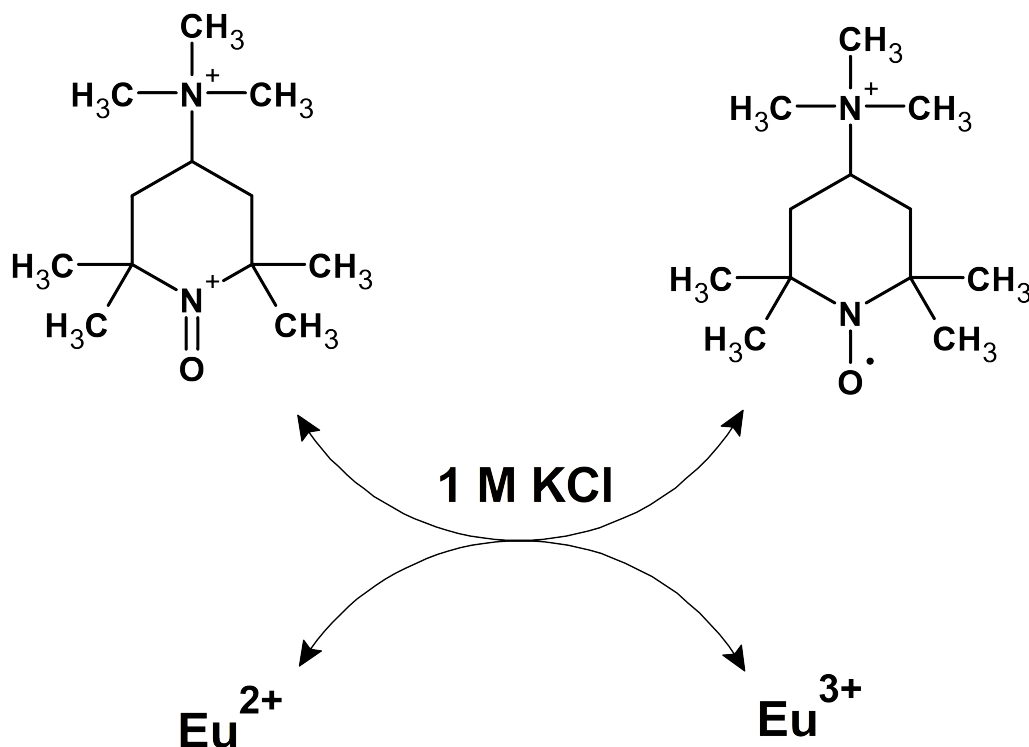
Scheme 2: The schematic illustration of redox reactions between TEMPTMA radical as posolyte and Eu^{3+} as negolyte in 1 M KCl as common electrolyte.

2. MATERIALS AND METHODS

Europium oxide (99.9%) was purchased from Alfa Aesar, Germany (Thermo Fisher Scientific), and TEMPOL (99%) was purchased from Jinan Refined Chemicals, China. Dimethylamine (DMA) and $AgNO_3$ was purchased from Sigma-Aldrich (Merck), Germany. Iodomethane (99.5%) was purchased from Acros Organics, Spain (Thermo Fisher Scientific). Other chemicals and supplements were obtained from VWR, Finland. AgCl was prepared by addition excess KCl to $AgNO_3$ solution in water. AgCl was suspended in isopropanol and covered with aluminum foil. TEMPTMA and $EuCl_3$ were prepared in accordance to designed synthetic methodologies (see supporting information).

All cyclic voltammetry analyses were performed using a PalmSens 4 potentiostat with PSTrace software from PalmSens BV (the Netherlands) using 2 mm glassy carbon disk electrode as working electrode (WE), 0.5 mm Pt wire as counter electrode (CE), and Ag/AgCl in 3.5 M KCl as reference electrode (RE). The experiments were carried out applying 95% of automatic IR drop compensation (Ru values ranging from 15 ohm to 30 ohm) evaluated with the ZIR tool. The glassy carbon disk working electrode was polished with 0.25 µm diamond powder (Büehler) and rinsed with distilled water during each measurement.

The EPR measurements were performed using Bruker Magnettech MS5000X on X-band (9.4 GHz) at room temperature with a typical organic radical adjustment setup for microwave power (10-20 mW) and magnetic field (200 – 650 mT) in quartz capillary which were sealed then with special plastic rubbers up and down. The resulting spectrum was processed using ESRStudio software and Origin.

3. RESULTS AND DISCUSSIONS

Before performing battery experiments, regular cyclic voltammetry analyses were run for Eu^{3+}, TEMPTMA, and a mixture of Eu^{3+}/TEMPTMA solutions to check reversibility and electrochemical compabilities. The cyclic voltammogram of mixture of Eu^{3+}/TEMPTMA also gave us understanding on detection of the battery voltage which is found to be 1.35 V (Figure 1).
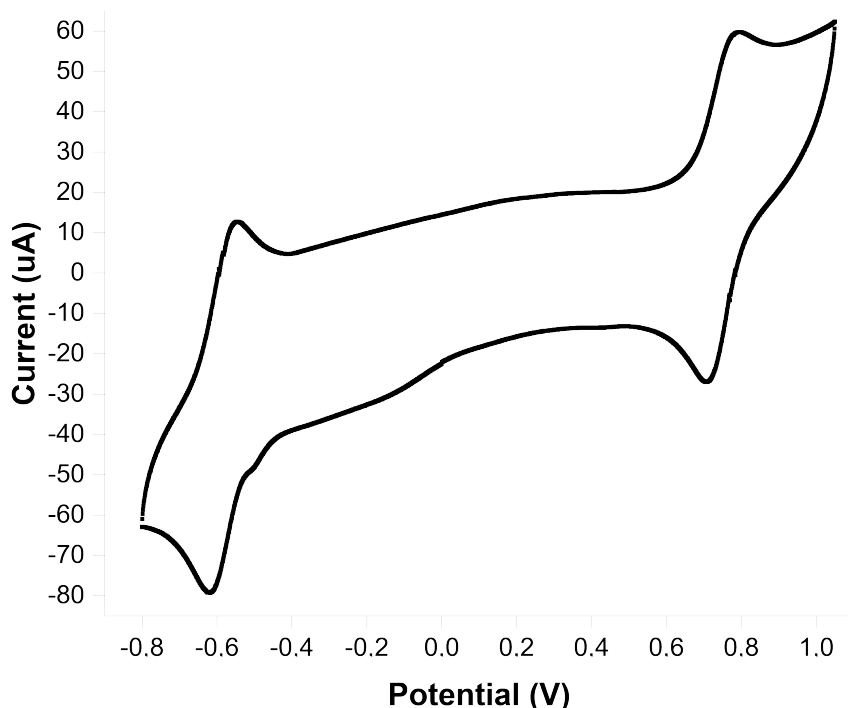
Figure 1: The cyclic voltammogram of mixture of Eu^{3+}/TEMPTMA in 1 M KCl using glassy carbon as working electrode (WE), Pt wire as counter electrode (CE) and Ag/AgCl in 3.5 M KCl as reference electrode (RE), scan rate: 100 mV/s.

A slightly capacity decay occurred at the early stages of the battery testing and after a while, the battery was stabilized and discharge capacity was slowly recovered to reach the certain amount to be restored (Figure 2). This could be explained that Eu(III) and Eu(II) ions can be found in various structures such as altered aqua and chloro complexes and those molecular rearrangements are more certain without decomposition. After 120 cycles within applying 100 mA current, charging at 1.35 V and applying 50 mA current, discharging at 0 V currents around 29 days, the battery system and the capacity are preserved successfully.
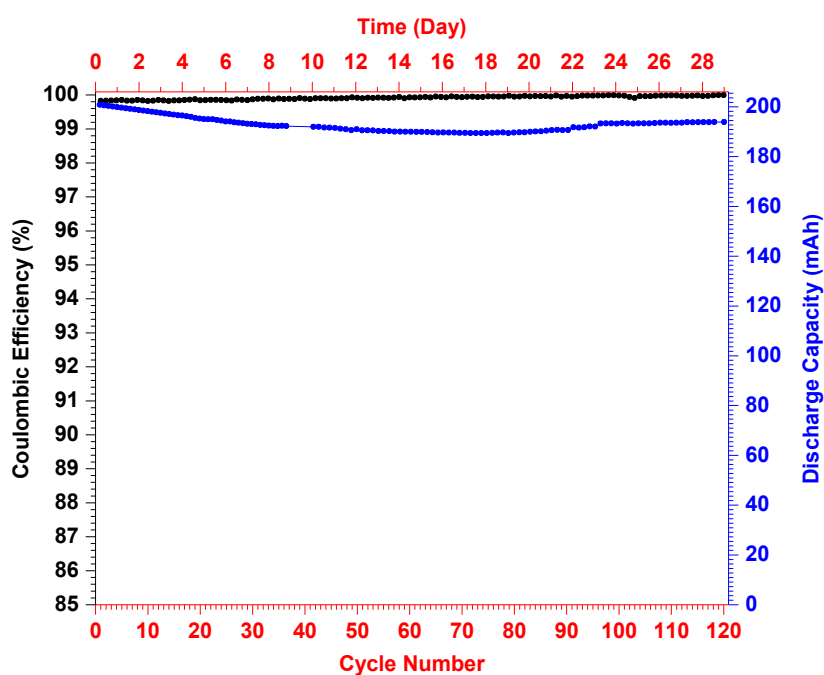
Figure 2. The experimental Coulombic efficiency and discharge capacity profile by day-based time and cycle numbers.

Additionally, we also tested self-discharge which was not considered in previous studies (17,18). In order to test self-discharge phenomenon, we tested our battery system for 5 hours period after being charged to Eu(II) to be found self-discharge 0.25 M Eu^{3+} in 1 M KCl is 0.0023% per hour, 0.0552% per day (Figure 3).
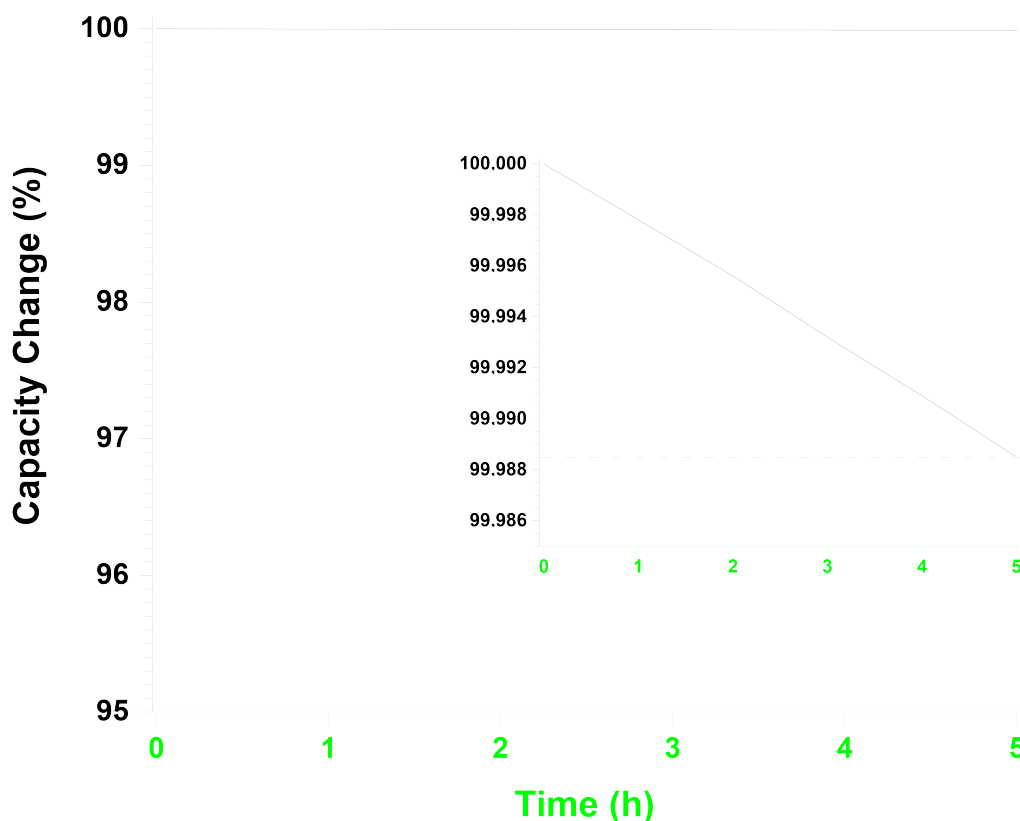
Figure 3: The self-discharge observation profile after charging at a certain time and rest mode for 5 hours.

It is concluded that Eu^{3+}/TEMPTMA-based one-electron battery system at 1.35 V in neutral pH containing 1 M KCl media showed good cycling performance. Our results were further compared with other Eu^{3+} batteries (16,17).

4. CONCLUSIONS

In conclusion, a hybrid aqueous redox flow battery of Eu^{3+} was tested as a negolyte material against $TEMPTA^+$ as a posolyte material in neutral pH 1M KCl supporting electrolyte. Eu^{3+}-based this 1.35 V redox flow battery system showed a good stability and reversibility under these circumstances. Self-discharge phenomenon was also considered and it found to be negligible as the charged-state battery is stable. The preliminary cost analyses also made to be compared regarding vanadium and Li-based batteries. As a results, Eu(III) ions are promising for long-term redox flow battery applications as compared to other heavy metals, europium is relatively non-toxic substance which carries no important biological role in living organisms.

5. ACKNOWLEDGMENTS

6. CONFLICT OF INTEREST

All authors declare that they have no conflicts of interest.

7. AUTHOR CONTRIBUTIONS

A. T.: conceptualization, data curation, formal analysis, investigation, methodology, validation, visualization, writing—original draft preparation, writing—review and editing.
P. P.: conceptualization, supervision, validation, writing—review and editing.

8. REFERENCES

1. Weber AZ, Mench MM, Meyers JP, Ross PN, Gostick JT, Liu Q. Redox flow batteries: A review. J Appl Electrochem [Internet]. 2011 Oct 2;41(10):1137–64. Available from: <URL>.

2. Ye R, Henkensmeier D, Yoon SJ, Huang Z, Kim DK, Chang Z, et al. Redox flow batteries for energy storage: A technology review. J Electrochem Energy Convers Storage [Internet]. 2018 Feb 1;15(1):010801. Available from: <URL>.

3. Bartolozzi M. Development of redox flow batteries. A historical bibliography. J Power Sources [Internet]. 1989 Sep 1;27(3):219–34. Available from: <URL>.

4. Arenas LF, Ponce de León C, Walsh FC. Redox flow batteries for energy storage: Their promise, achievements and challenges. Curr Opin Electrochem [Internet]. 2019 Aug 1;16:117–26. Available from: <URL>.

5. Li Z, Lu Y. Material design of aqueous redox flow batteries: Fundamental challenges and mitigation strategies. Adv Mater [Internet]. 2020 Nov 22;32(47):2002132. Available from: <URL>.

6. Alotto P, Guarnieri M, Moro F. Redox flow batteries for the storage of renewable energy: A review. Renew Sustain Energy Rev [Internet]. 2014 Jan 1;29:325–35. Available from: <URL>.

7. Sánchez-Díez E, Ventosa E, Guarnieri M, Trovò A, Flox C, Marcilla R, et al. Redox flow batteries: Status and perspective towards sustainable stationary energy storage. J Power Sources [Internet]. 2021 Jan 1;481:228804. Available from: <URL>.

8. Zhang J, Jiang G, Xu P, Ghorbani Kashkooli A, Mousavi M, Yu A, et al. An all-aqueous redox flow battery with unprecedented energy density. Energy Environ Sci [Internet]. 2018 Aug 8;11(8):2010–5. Available from: <URL>.

9. Rhodes Z, Cabrera-Pardo JR, Li M, Minteer SD. Electrochemical advances in non-aqueous redox flow batteries. Isr J Chem [Internet]. 2021 Jan 28;61(1–2):101–12. Available from: <URL>.

10. Janoschka T, Martin N, Hager MD, Schubert US. An aqueous redox-flow battery with high capacity and power: The TEMPTMA/MV system. Angew Chemie Int Ed [Internet]. 2016 Nov 7;55(46):14427–30. Available from: <URL>.

11. Zhu F, Guo W, Fu Y. Functional materials for aqueous redox flow batteries: Merits and applications. Chem Soc Rev [Internet]. 2023 Nov 27;52(23):8410–46. Available from: <URL>.

12. Yang G, Zhu Y, Hao Z, Lu Y, Zhao Q, Zhang K, et al. Organic electroactive materials for aqueous redox flow batteries. Adv Mater [Internet]. 2023 Aug 30;35(33):2301898. Available from: <URL>.

13. Cannon CG, Klusener PAA, Brandon NP, Kucernak ARJ. Aqueous redox flow batteries: Small organic molecules for the positive electrolyte species. ChemSusChem [Internet]. 2023 Sep 22;16(18):e202300303. Available from: <URL>.

14. Chen R, Zhang P, Chang Z, Yan J, Kraus T. Grafting and solubilization of redox-active organic materials for aqueous redox flow batteries. ChemSusChem [Internet]. 2023 Apr 21;16(8):e202201993. Available from: <URL>.

15. Zhang Y, Cao J, Chen Z, Xu J, Yu C. An organic-based aqueous hybrid flow battery with high power and long cycle life: A tetrapyridophenazine/ferrocyanide system. J Mater Chem A [Internet]. 2020 Apr 7;8(14):6874–81. Available from: <URL>.

16. Sun P, Liu Y, Zuo P, Li Y, Chen Q, Yang Z, et al. Eu-based anolytes for high-voltage and long-lifetime aqueous flow batteries. J Energy Chem [Internet]. 2021 Sep 1;60:368–75. Available from: <URL>.

17. Zeng D, Mao T, Zhang Z, Dai J, Ouyang J, Xie Z. A high-performance aqueous Eu/Ce redox flow battery for large-scale energy storage application. Int J Heat Mass Transf [Internet]. 2024 Nov 15;233:125978. Available from: <URL>.